Office of Graduate Studies
Dissertation / Thesis Approval Form

This form is for use by all doctoral and master's students with a dissertation/thesis requirement. Please print clearly as the library will bind a copy of this form with each copy of the dissertation/thesis. All doctoral dissertations must conform to university format requirements, which is the responsibility of the student and supervising professor. Students should obtain a copy of the Thesis Manual located on the library website.

Dissertation/Thesis Title: Compact Reconfigurable Antennas for Wireless Systems and Wearable Applications

Author: Damiano Patron

This dissertation/thesis is hereby accepted and approved.

Signatures:

Examining Committee

Chair _____

Members _____

_____

_____

_____

_____

Academic Advisor _____

Department Head _____

Office of Graduate Studies • 3141 Chestnut St. • Randell Hall 240 • Philadelphia, PA 19104
Tel.: 215-895-0366 • **Fax**: 215-895-0495 • **Email**: graduate@drexel.edu • **Web**: www.drexel.edu/provost/graduatestudies

Compact Reconfigurable Antennas for Wireless Systems and Wearable Applications

A Thesis

Submitted to the Faculty

of

Drexel University

by

Damiano Patron

in partial fulfillment of the

requirements for the degree

of

Doctor of Philosophy

May 2015

© Copyright 2015
Damiano Patron. All Rights Reserved.

Dedication

To my parents Moreno Patron and Teresa Vergari

for being symbols of strength and hard work for me, and for supporting and encouraging my passions and my growth.

To my family and my friends

whose love and support made this work possible.

Acknowledgments

I would like to express my sincere gratitude to my advisor Dr. Kapil R. Dandekar for his invaluable guidance and support during my studies and research activities. I was very fortunate to have his support and the freedom to explore new research fields. Thanks to Dr. Dandekar I broadened my skills in engineering, teaching, entrepreneurship, presenting at international conferences and scientific writing.

I would also like to thank my dissertation committee Dr. Kurzweg, Dr. Fontecchio, Ms. Dion and Dr. Taskin for their support and insights. In addition, I would like to thank Dr. Afshin S. Dayoush for his invaluable teaching of passive and active RF circuits and antennas. The outcome from his class projects inspired and enhanced my research. I also thank all my friends and colleagues at the Drexel Wireless System Laboratory, and in general my friends and stuff at Drexel University.

Finally, I would like to thank and dedicate this thesis to my parents and family. My father Moreno Patron who always supported and encouraged my passion for electronics and radio-frequency since I was very young. My mother, Teresa Vergari for giving me the strength, support and encouragement to set my goals high and to excel in them. Thank you to my aunts Maria Pia and Lavinia Vergari, and to my grandmother Angela Bovo, for their love, care and support during these years.

Table of Contents

LIST OF TABLES viii

LIST OF FIGURES ix

ABSTRACT xvi

1. INTRODUCTION 1

1.1 General Classification of Antenna Types 2

1.2 Innovative Contributions of this Thesis 5

1.3 Thesis Outline 13

2. BACKGROUND 15

2.1 Benefits of Reconfigurable Antennas in MIMO Systems 15

2.2 Pattern Reconfigurable Antennas 19

2.2.1 Antennas with Embedded Switches 20

2.2.2 Antennas with Variable Capacitors 24

2.2.3 Electronically Controlled Leaky-wave Antennas 26

3. RECONFIGURABLE ALFORD LOOP ANTENNA 31

3.1 Native Design 32

3.2 Reconfigurable Alford Loop Antenna Design 34

3.2.1 Radiation Characteristics 36

3.2.2 Comparison Between Numerical and Experimental Results 37

3.2.3 Integration of Switching Control Circuitry 39

3.2.4 Numerical Simulations for WiFi and WiMAX Bands 43
3.2.5 Experimental Analysis of Pattern Diversity for MIMO Applications 46
3.2.6 PIN Diode Non-linear Effects in MIMO Array 48
3.3 Optically-controlled Reconfigurable Alford Loop Antenna 55
3.3.1 Phototransistor as Optical Control of RF PIN Diodes 57
3.3.2 Experimental Results 58
3.3.3 Antenna Design With Integrated Optical Circuitry 61
3.4 Multi-band Reconfigurable Alford Loop Antenna 69
3.4.1 Multi-band Elements Approach 70
3.4.2 Input Impedance Experimental Results 71
3.4.3 Radiation Patterns 72
3.4.4 Single-band Elements Approach 73
3.4.5 Input Impedance Experimental Results 75
3.4.6 Radiation Patterns 76
3.5 Summary 76
4. MINIATURIZATION OF RECONFIGURABLE CRLH LEAKY-WAVE ANTENNAS . 80
4.1 Overview 80
4.2 Related Work 81
4.3 Improved LWA Design 85
4.3.1 Experimental Results 86
4.4 Application for Direction Of Arrival Estimation 88
4.5 Design of the Miniaturized CRLH LWA Unit Cell 91
4.5.1 Experimental Results 94

4.6 Miniaturized CRLH LWA Antenna 97
4.6.1 Input Impedance Experimental Results 98
4.6.2 Radiation Patterns Experimental Results 99
4.6.3 Comparison with Conventional LWA Model 101
4.7 Summary 103
5. WEARABLE STRAIN SENSOR THROUGH FREQUENCY-RECONFIGURABLE ANTENNAS AND RFID TECHNOLOGY 105
5.1 Related Work 106
5.2 Inductively Coupled RFID Tag 108
5.3 Flexible RFID Strain Sensor Using Inductively Coupled RFID Tag 110
5.3.1 Experimental Dielectric Characterization 110
5.3.2 Folded Dipole Antenna Design 111
5.3.3 Impedance Measurements Setup and Experimental Results 115
5.3.4 Strain Sensitivity Experimental Analysis 117
5.4 Knitted RFID Strain Sensor 118
5.4.1 Experimental Material Characterization 118
5.4.2 Knitted Antenna Design 120
5.4.3 Input Impedance Experimental Results 123
5.4.4 Radiation Pattern Experimental Results 126
5.4.5 Effects of the Human Body Proximity 127
5.5 Application as a Biomedical Contractions Sensor 130
5.6 Application as a Baby Breathing Monitor 131
5.7 Summary 134

6. CONCLUSIONS 136

BIBLIOGRAPHY 142

APPENDIX A: COMMERCIALIZATION OF RECONFIGURABLE ANTENNAS 154

A.1 Modes of University Technology Commercialization 155

A.1.1 Survey Results and Considerations 163

VITA 167

List of Tables

3.1 Maximum Spatial Correlation and Mutual Coupling Between Patterns Using Two RALAs. 47

3.2 RALA Equivalent RLC model values 50

3.3 PIN Diode Intrinsic Values 53

3.4 Intermodulation Distortion Simulations 55

3.5 PT19-21B Phototransistor Characteristics 58

3.6 Optical Reconfigurable Alford Loop Antenna Dimensions 61

3.7 Bandwidth Comparison Between Optical Control, Electrical Control and Simulation 66

4.1 Summary of Four Different Configurations at the Frequency of 2.46 GHz . . . 87

4.2 Comparison Between Expected and Measured DoAs. 91

4.3 Summary of Four Different Configurations at the Frequency of 2.46 GHz . . . 96

4.4 Comparison Between Conventional and Miniaturized LWAs 103

5.1 Murata MAGICSTRAP IC Characteristics 110

5.2 RSSI Measurement Results 118

5.3 Supporting Material Characterization 119

5.4 Human Stomach Layer Properties 128

A.1 Current Firms Commercializing Reconfigurable Antenna Technologies 164

List of Figures

1.1 Antennas classification and types of reconfigurable antennas 2

2.1 Reconfigurable printed dipole antenna array [1]. 21

2.2 Reconfigurable circular patch antenna [2]. 21

2.3 Reconfigurable circular slot antenna [3]. 22

2.4 (a) Planar electronically beam steering antenna [4]. (b) Reconfigurable Zeroth-order loop antenna, top and bottom view [5]. 24

2.5 (a) Example of ESPAR antenna architecture [6]. (b) Schematic of basic configuration and controlling principle [7]. 25

2.6 (a) Circuit model of a hypotetical uniform LH transmission line. (b) Circuit model of a Composite Right/Left-Handed (CRLH) transmission line. (c) Planar LH transmission line in microstrip technology. [8] 27

2.7 Sketch of a two-port CRLH Reconfigurable Leaky-Wave antenna with details of the beamsteering capability. 29

2.8 (a) CRLH LWA controlled with a single voltage and (b) detail of metamaterial unit cell [9]. (c) CRLH LWA controlled with two voltages and (d) detail of the metamaterial unit cell [10]. 30

3.1 Sketch of the four radiating elements comprising the ultrahigh-frequency loop [11]. The current distribution in one of the elements is shown with red arrows. . 33

3.2 Layout of the first Reconfigurable Alford Loop Antenna, for the frequency of 3.8 GHz 35

3.3 Simulation of the Reconfigurable Alford Loop Antenna. (a) Four active pairs and radiation of omnidirectional beam. (b) Single active pair and radiation of a directional beam. 36

3.4 Simulated and measured return loss for both the omnidirectional (a) and the directional (b) modes. 38

3.5 Measured radiation patterns for both omnidirectional (a) and directional modes (b). In (c) is shown a summary of the directional beams. 39

3.6 Transmission line used for PIN diode measurements and control circuitry schematic. 40

3.7 S_{12} measurements under different control voltage levels, at V_{CC} = 3.3 V 41

3.8 3D view and dimensions of the 2.4 GHz RALA. 43

3.9 Schematic and arrangement of the switching circuitry components. 43

3.10 PIN diode equivalent model: (a) Forward bias, ON state. (b) Reverse bias, OFF state. 44

3.11 Return loss of the 2.4 GHz RALA for the three possible radiation modes. . . . 45

3.12 Simulated radiation patterns for (a) Omnidirectional mode, (b) Directional mode, (c) Bi-directional mode. 46

3.13 The best fitted equivalent model of return loss and comparison of RL with actual antennas measurements: (a) omnidirectional (b) directional. 51

3.14 Circuit schematic of two antenna models equipped with pin-diodes, emulating coupling in 2x2 MIMO antenna system 51

3.15 HB simulation, both antennas in omnidirectional mode: (a) low coupling, k = 0.1 (b) higher coupling k = 0.5 (c) very high coupling k = 0.9. 54

3.16 PIN diode mounted on microstrip lines for S-parameter measurements and detail of the optical control circuitry. 58

3.17 S_{21} measurements of the PIN diode under different levels of λ = 850 nm laser illumination on the phototransistor. Lumped equivalent models of ON and OFF states are also shown. 59

3.18 3D model of the proposed reconfigurable planar antenna. (a) Top layer view. (b) Horizontal profile with RF input port detail. (c) Bottom layer view. The small pads and lines visible on both layers constitute the arrangement for the SMD components population. 62

3.19 Manufactured prototype and details of the optical switching circuitry for a pair of symmetric elements. (a) Top layer biasing circuitry. (b) Bottom layer optical and biasing circuitry. The voltage and current activated by the phototransistor, are shared between the two layers through a via hole (red dashed line). 63

3.20 Simulated return loss for each antenna state and comparison of measurements between electrical and optical control. (a) Omnidirectional mode (b) Directional mode. While the simulated S_{11} is always identical for each directional state, some slight differences occur in real scenario when the four directional modes are measured under light illumination. 65

3.21 Measured radiation patterns, at 2.45 GHz. (a) Omnidirectional beam, azimuth and elevation view. All the microstrip elements are connected to the central port. (b) Single directional beam, azimuth and elevation view. In this example, only the pair of elements along negative x axis is activated. (c) Azimuth view summary of the four possible directional beams. Note that each beam is activated singularly. 68

3.22 Comparison of radiation patterns between optical and electrical control of the proposed reconfigurable antenna. (a) Omnidirectional state. (b) Directional state. Measurements conducted at 2.45 GHz. 69

3.23 (a) Top and bottom layer pictures of the fabricated multi-band RALA. The total dimensions are 9 x 9 cm. (b) Illustration of a single element, with lumped inductor L and capacitor C for separating the two current flows at 2.4 and 5 GHz. 71

3.24 Measured return loss when all the elements are connected (Omnidirectional) and when just two adjacent elements are connected (Directional). Good impedance matching is accomplished within the whole 2.4 GHz band and from channel 40 to 60 in the 5 GHz band. 72

3.25 Simulated radiation patterns. (a) Omnidirectional and directional beams at 2.45 GHz. Gain are 0.7 and 3.6 dBi, respectively. (b) Omnidirectional and directional beams at 5.3 GHz. Gain are 2.4 and 3.4 dBi, respectively. As expected, the beams generated by the internal 5 GHz elements couples with the larger elements, and yielding local magnitude reductions. 73

3.26 (a) Top and bottom layer pictures of the proposed antenna. The total dimensions are 6.5 x 6.5 cm. (b) Detail of a single pair of elements; a lumped diplexer is used to separate the two current flows. 74

3.27 Measured return loss for omnidirectional and directional patterns at 2.4 and 5 GHz. Similar to the first approach, good impedance matching is accomplished within the whole 2.4 GHz band and from channel 40 to 60 at 5 GHz. However, the higher selectivity of the diplexer allows for the blocking of larger resonances outside the two bands. 75

3.28 Simulated radiation patterns. (a) Omnidirectional and directional beams at 2.45 GHz. Gain are 1.7 and 3.8 dBi, respectively. (b) Omnidirectional and directional beams at 5.3 GHz. Gain are 3 and 3.2 dBi, respectively. As expected, the beams generated by the smaller 5 GHz elements undergo some coupling with the larger elements, resulting in slight local magnitude reductions and side lobes. 77

4.1 Sketch of a two-port CRLH Reconfigurable Leaky-Wave antenna with details of the beamsteering capability. 80

4.2 (a) Sketch of a CRLH leaky-wave antenna with beam steering from broadside $\theta = 0^\circ$ to backward θ_1 and forward θ_2 angles. (b) Schematic of a conventional CRLH unit cell (c) Dispersion diagram used to evaluate the propagation constant β and estimate the main beam angle θ. 82

4.3 CRLH LWA prototype and unit cell details. 85

4.4 Measured scattering parameters of the CRLH LWA: (a) V_S = 12 V - V_{SH} = 11 V, (b) V_S = 14 V - V_{SH} = 16.5 V, (c) V_S = 20 V - V_{SH} = 18 V. 87

4.5 Measured radiation patterns (*z-y* plane) of the CRLH LWA: (a) Positive angles, port 1 connected, (b) Negative angles, port 2 connected. 88

4.6 Anechoic chamber DoA measurement setup. 89

4.7 Measured DoA performance using the proposed CRLH LWA and modified MUSIC algorithm. 90

4.8 (a) 3D HFSS model of the LWA unit cell, with CSRR etched on the ground plane. (b) 2D top layer layout and dimensions. (c) Bottom layer with ground plane and CSRR design. r_1 = 5 mm and r_2 = 4 mm. The gap *g* and the distance between the two rings is 0.5 mm. 91

4.9 Junction capacitance C_J and series resistance R_S as function of the reverse voltage V_R. The values were extracted from the measured S-parameters. While R_S maintains a relatively constant value within the entire voltage sweep, the capacitance C_J exhibits a larger dynamic range when $V_R \leq 10$ V. 93

4.10 Top and bottom layer pictures of the miniaturized LWA unit cell. The design is etched between two $\lambda/8$ microstrip lines for S-parameter measurents. 95

4.11 Simulated and measured S-parameters for four different configurations. While V_S acts as major controller for the center frequency, V_{SH} allows for fine-tuning and improvement of the impedance. 96

4.12 Dispersion diagram of the proposed miniaturized CRLH unit cell. The four different states were taken for incremental values of bias voltages V_S V_{SH}. The desired frequency bandwidth, 2.41 - 2.48 GHz, falls within the RH radiated region. 97

4.13 Picture of the miniaturized CRLH LWA. (a) Top layer with cascade or N = 11 unit cells. (b) Bottom layer with CSRRs. The overall dimensions are: l = 11.5 cm, h = 2.3 cm. 98

4.14 Measured S-parameters of the miniaturized CRLH LWA. 99

4.15 Measured 3D radiation patterns at 2.46 GHz for four configurations. Port 2, oriented in +y direction was connected to a signal generator, while port 1 was terminated to a 50 Ω matched load. (a) V_S = 8.5 V, V_{SH} = 10 V (b) V_S = 7 V, V_{SH} = 9 V (c) V_S = 6 V, V_{SH} = 12 V (d) V_S = 5 V, V_{SH} = 4 V. 100

4.16 Azimuth (x-z) view of the total beam steering capabilities. The solid lines depict beams generated by exciting port 1 (and port 2 terminated to a 50 Ω load), whereas the dashed beams with port 2 (and port 1 terminated to a 50 Ω load). 101

4.17 Comparison between the conventional and the proposed miniaturized reconfigurable LWA. Both antennas were designed by cascading N = 11 unit cells. The former occupies an area of 56 cm^2 while the latter 26.5 cm^2. 102

5.1 Dielectric characterization of the polyethylene substrate, compared with the standard air characteristics. 111

5.2 3D HFSS model of the folded dipole antenna. The substrate characteristic was defined based on the dielectric measurements, while the metallization was assumed copper. The lumped port used as excitation was set accordingly to the microchip impedance Z_c = 25 - j 200 Ω. 113

5.3 Simulated folded dipole antenna input impedance Z_a. 114

5.4 Numerical estimation of the reflection coefficient S_{11} within the highlighted bandwidth above, from 800 to 960 MHz. 114

5.5 Radiation characteristic of the folded dipole antenna. The pattern resemble the typical dipole omnidirectional pattern, with uniform radiation around the plane normal to the feed port (x-z). 115

5.6 Measured input impedance through the test fixture. 116

5.7 Numerical estimation of the return loss, S_{11}. 117

5.8 RSSI measurement setup within the anechoic chamber. 118

5.9 3D Simulation model of the proposed wearable RFID sensor. The substrate characteristics were defined based on the dielectric measurements reported in Table 5.3. As an RF excitation, a lumped port was set according to the RFID tag impedance Z_c = 25 - *j* 200 Ω. 121

5.10 Simulated complex input impedance of the textile folded dipole antenna. 122

5.11 Numerical estimation of the return loss S_{11} using 5.1. The antenna layout has been optimized to yield good impedance matching within the whole frequency range of the RFID tag: 870 - 915 MHz. 122

5.12 Simulated current distribution and radiation characteristics. (a) The highest density of current distribution flows along the major axis, generating an omni-directional beam normal to the y axis. (b) 2D radiation pattern for both azimuth (x-y plane, dashed line) and elevation plane (x-z plane, solid line). 123

5.13 Experiment setup of S-parameter measurements. (a) Network analyzer connected to the two-port fixture. (b) Knitted dipole antenna prototype with location of the pocket for RFID tag housing and detail of the two-port fixture for balanced impedance measurements. 124

5.14 Measured complex input impedance of the knitted folded dipole ntenna, using the differential measurement approach. 125

5.15 Measured return loss S_{11}, extracted using 5.1. The 10 dB return loss bandwidth is 100 MHz. 126

5.16 Anechoic chamber setup for radiation pattern measurements. (a) Directional antenna connected to Impinj Speedway reader [12]. (b) Knitted folded dipole antenna with MAGICSTRAP tag inserted within the knitted pocket. 127

5.17 Sketch of the human body stomach model used for simulations. 128

5.18 Return loss S_{11} of the RFID tag antenna for different distances d from the human stomach model. 129

5.19 Radiation patterns as function of the heights d above the human stomach, at the frequency of 870 MHz. (a) d = 5 mm, (b) d = 10 mm, (c) d = 30 mm, (c) d = 45 mm. Under low distance the gains are negative, while when d is increased, the gains are about 60 % higher than without human stomach. 130

5.20 Performance comparison between the proposed wearable RFID sensor (red) and a commercial tocodynamometer (blue). 131

5.21 Plot of breathing and non-breathing patterns detected using the wearable strain sensor, along with the support vector machine algorithm. 133

A.1 Summary of the three academic modes of technology commercialization. The external approaches lead to higher separation from the academic institution, and it can be accomplished through technology licensing, spin-offs or joint ventures. 156

A.2 Benefits and costs summary of technology licensing for both the licensor and the licensee. 158

A.3 Benefits and costs of the spin-off mode of commercialization. 160

A.4 Benefits and costs of the joint venture as a third mode of external approach of technology commercialization. 161

Abstract

Compact Reconfigurable Antennas for Wireless Systems and Wearable Applications
Damiano Patron
Dr. Kapil R. Dandekar

The fast growth of wireless communications has driven the necessity of exploiting technological solutions for the needs of faster connectivity. While bandwidth allocation and effective radiated power (ERP) are subjected to regulatory constraints, alternative solutions have been developed to overcome the challenges that arise in terms of wireless coverage and number of users. Reconfigurable antennas (RAs) technology is one of the hardware solutions developed to enhance the connectivity between wireless devices. These new classes of radiating elements are able to adapt their physical characteristics in response to the environmental changes or user density and location. Reconfigurable antennas can be divided into two main categories: frequency reconfigurable antennas and pattern reconfigurable antennas. The former class of RAs are able to switch the operational frequency in order to move the communication within unoccupied channels. The latter category defines those antennas that are able to change their radiation characteristics (radiation pattern or polarization) in response to the dynamics of the surrounding environment. Unlike conventional static antennas where the energy is wasted around the surrounding space, the use of RAs allows for a smarter management of the radiated energy as the beam can be focused toward specific directions. As a result, not only data throughput between two devices can be improved but also the interference between adjacent networks can be reduced significantly.

In this Ph.D. thesis we focus on the design, prototyping and system application of compact RAs for wireless base stations and mobile devices. Specifically, the first part focuses on the design of a compact reconfigurable antenna capable of generating omnidirectional and directional beams in a single planar design. Next, we propose to apply a miniaturization technique in order to drastically reduce the size of Composite Right-Left Handed

Reconfigurable Leaky-Wave Antennas (CRLH RLWAs). The large beam steering capabilities along with the miniaturized dimension open new venues for the integration of this antenna technology into mobile devices such as laptops or tablets.

Similarly for electrically reconfigurable antennas, characteristics such as the input impedance and the radiation properties of a radiating element can vary by mechanically changing its physical dimension. In other words, instead of changing the metallic geometry through electrical components, the characteristics of an antenna can be changed through physical deformation of its geometry. This principle addresses the second main application of reconfigurable antennas in this Ph.D. thesis.

Wearable technologies are gaining a lot of attention due to their strong potential for sensing, communication and tactile interaction applications. Thanks to the progresses in knitting facilities and techniques, smart fabrics are generally implemented through sewn-in sensors, especially in the fields of medical and athletic applications. Such wearable sensors provide a means to monitor the wearers health through physiological measurements in a natural setting or can be used to detect or alert care providers to potential hazards around the wearer. The feasibility of building electrical devices have been demonstrated in recent literature using conductive fabrics has been analyzed through electrical characterization of textile transmission lines and antennas where conductive fabrics have been applied onto woven fabrics. Previous works show conductive copper foils or fabrics bonded to a flexible substrate. However, these techniques show limitations in terms of electrical losses caused by adhesives or glue chemicals. It is desirable to address these drawbacks by knitting conductive and non-conductive yarns in a single process resulting in smart textiles that are unobtrusively integrated into the host garment so as to eliminate the need for chemical adhesives that degrade the electrical performance. The characteristic variations of a fabric-based antenna under physical deformations can be exploited to provide a fully wireless sensing of certain body movements. The second part of this Ph.D. thesis focuses on the design and testing of these purely textile wireless sensors for biomedical applications. The Radio-Frequency Identification (RFID) technology will be applied for

designing fabric-based strain sensors through the use of novel inductively coupled RFID microchips (MAGICSTRAP). As opposed to conventional surface-mount microchips, the MAGICSTRAP does not require any physical soldering connection as the RF energy is inductively coupled from the microchip's pads to the antenna's arms. A separate interrogator unit can communicate with this knit passive RFID architecture by sending a probing signal; the backscattered component received from the knit tag will indicate the level of stretch, and this information will be translated in the physical phenomenon being monitored. The change in the electrical characteristics of the textile antenna, along with the decoupling of the MAGICSTRAP chip allow, for more reliable detection of contraction/elongation movements. This study will include comprehensive design and characterization of the textile tag sensor along with performance analysis using mechanical human mannequins.

Chapter 1: Introduction

Reconfigurable antennas have received significant attention in the literature with respect to static antennas (antennas with a fixed radiation pattern) thanks to their capability of dynamically changing their radiation properties. These antennas can adapt their characteristics in response to the behavior of the wireless channel and can be used for a variety of applications, including throughput maximization [13, 14], interference management [15], directional networking [16], spectrum sensing [17] and security [18, 19]. Reconfigurable antennas are typically developed by means of electrical components, such as switches or loading devices. These lumped components alter the metallic layout, changing the radiation properties of the antenna.

In addition to the pattern reconfigurability, the property of frequency reconfiguration of antennas can also be used for expanding the potential applications. Mechanical deformation of a flexible antenna can achieve similar reconfigurability, changing input impedance and radiation characteristics. Specifically, it has been demonstrated that a radiating element can be applied for strain and crack monitoring. In essence, the mechanical changes of an object can be monitored through elongation or relaxation of the antenna that is applied to it. This change in shape produces a down or up shift of the antenna's resonant frequency, as noted by [20]. By connecting a small Radio Frequency Identification (RFID) microchip at the antenna input port, the change in the resonant frequency can be detected by looking at the wireless backscattered power received by an interrogating unit. Specifically, a com-

mercially available RFID reader will keep interrogating the RFID tag, detecting the value of the backscattered power (RSSI) and providing indication of object's deformation.

1.1 General Classification of Antenna Types

In Fig. 1.1 we show the general classification of antenna types. The first subset of *Standard Antennas* comprises those antennas having fixed frequency and radiation properties. Examples of this type are standard dipole or monopole antennas, where a specific and fixed current distribution defines the radiation characteristic.

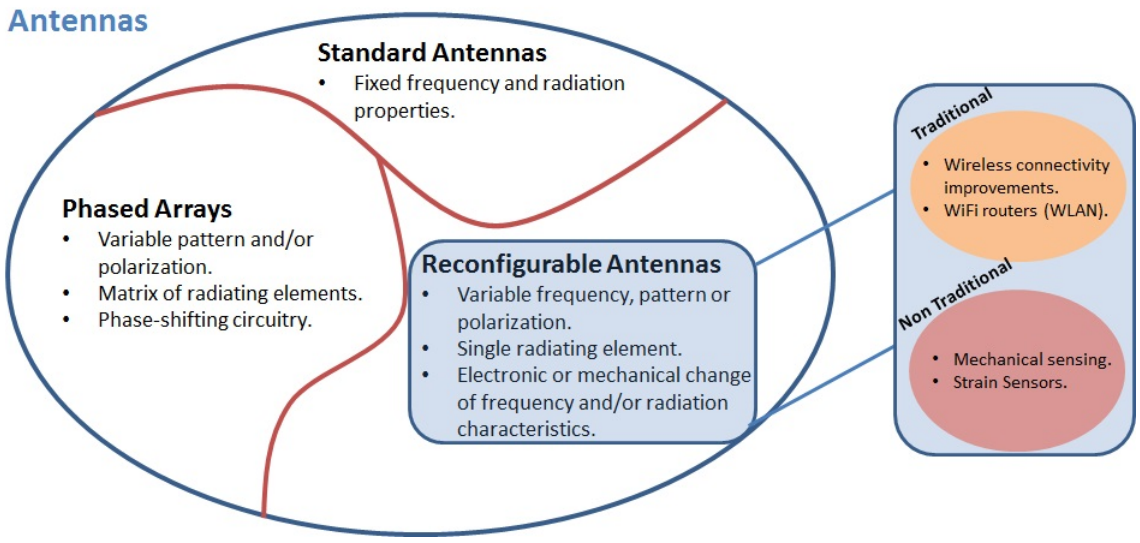

Figure 1.1 Antennas classification and types of reconfigurable antennas

Adaptive antennas can be divided into two subclasses: *phased arrays* and *reconfigurable antennas*. Phased arrays require a cascade of multiple elements and five types of controls can be used to change the radiation pattern [21]:

1. Geometrical configuration of the overall array (linear, circular, rectangular, spherical, etc.)

2. Distance between the elements

3. Amplitude excitation of each element

4. Phase excitation of each element

5. Relative pattern of each element

The method of controlling the phase between the elements is preferred for the purpose of tilting the radiation pattern and thus designing a beam-steering antenna. The total field of an antenna array can be seen as the field of a single element positioned at the origin, multiplied by a factor which is called the *array factor*. The array factor is a function of the geometry of the array and the excitation phase. The normalized array factor is given by:

$$AF = \cos\left[\frac{1}{2}(kd\cos\theta + \beta)\right] \tag{1.1}$$

where k is the wavenumber, d is the distance between each antenna element, θ is the steering angle, and β is the phase shift between the antenna elements. Mathematically, the total field of a uniform array of identical elements is equal to the product of the field of a single element and the array factor of that array:

$$\mathbf{E}(total) = [\mathbf{E}(\textit{single element})]\, x\, [\textit{array factor}] \tag{1.2}$$

This is referred to as *pattern multiplication* of arrays of identical elements.

Phased arrays are characterized by large form factors and requires phase shifting circuitry to provide the necessary phase to steer the directional beam. On the other hand, reconfigurable antennas consist of a single radiating element, capable of generating different patterns or polarizations. The reconfigurable antenna solution is thus preferable with

respect to a phased array antenna mainly because: *i)* it employs a single active element and therefore it occupies a smaller space and *ii)* it allows for high radiation efficiency since it does not employ phase shifters and power dividers.

Generally speaking, reconfigurable antennas can be divided into two main categories: frequency-reconfigurable antennas, which are able to adapt their resonant frequency based on the desired operational frequency [22], and pattern-reconfigurable antennas which can change their radiation pattern or polarization in order to enhance the capacity of the wireless channel [23]. Such reconfigurability is typically provided by changing the current distribution on the metallic elements through switches [24] or reactive components [25], such as PIN diodes or varactor diodes or by stretching a flexible design [26].

Different types of reconfigurable antennas capable of changing pattern and polarization have been proposed. These antennas may employ embedded switches or variable capacitors to change the current distribution on the metallization of the active element [27]; or may employ an active antenna element surrounded by passive elements (i.e., parasitic elements) loaded with variable capacitors or connected to switches [28, 29].

Furthermore, these classes of reconfigurable antennas have been used for different purposes. The traditional electrically reconfigurable antennas find applications for throughput maximization within WiFi routers and other WLAN devices, whereas stretchable antennas are used for their frequency-reconfigurability in the field of mechanical sensing, such as crack detection and other strain sensing. In this thesis, we discuss novel compact designs for both traditional and non-traditional applications such as WiFi routers and wearable applications.

1.2 Innovative Contributions of this Thesis

Reconfigurable Alford Loop Antenna: Different types of reconfigurable antennas, capable of changing pattern and polarization, have been proposed in the literature. These antennas may employ embedded switches or variable capacitors to change the current distribution on the metallization of the active element or may employ an active antenna element surrounded by passive elements (parasitic elements) loaded with variable capacitors or connected to switches. However, none of the prior art approaches allow radiating with omnidirectional and directional radiation patterns while preserving a planar and cost-effective design (e.g., two layer printed circuit board and limited number of lumped components). In some applications, such as WLAN, distributed (Multiple-Input Multiple-Output) MIMO [30], or complex multipath propagation environments, the employment of horizontally polarized antennas with omnidirectional patterns may result to be more convenient. To our knowledge, the only antenna technology capable of achieving both omnidirectional and directional radiation patterns is the Reconfigurable Zero-Order Loop Antenna, presented in [5]. However, the metamaterial active element of such a design, along with the surrounded reactive components, results in a narrow frequency bandwidth. In [4] the authors propose the design of a planar antenna made by surrounding a central radiating element with switchable parasitics. However, the design is characterized by a large number of RF switches. The first contribution of this Ph.D. thesis is in the design of a planar reconfigurable antenna which we will call Reconfigurable Alford Loop Antenna (RALA). This antenna is capable of generating omnidirectional and directional radiation patterns over a wide frequency band or over multiple bands, using a limited number of lumped compo-

nents. For the purpose of generating an omnidirectional and directional radiation pattern, we propose to apply the concept of the Alford Loop Antenna [11] with re-designed metallic elements, making it a compact pattern-reconfigurable antenna.

Furthermore, we show two design approaches for covering 2.4 and 5 GHz WiFi channels simultaneously. Building on the Reconfigurable Alford Loop antenna design, the first approach uses lumped inductors and capacitors for designing dual-band elements, while in the second approach two independent sets of elements are combined together using lumped diplexers.

The Reconfigurable Alford Loop Antenna requires switching components to connect or disconnect the microstrip elements to the central RF port. This can be accomplished by using PIN diodes, which are Single-Pole Single-Throw (SPST) switches that operate in the RF domain. As a commercial PIN diode, we have used the Skyworks™ SMP-1345, a PIN diode specifically designed to operate up to 6 GHz. In order to avoid external control boards for driving the PIN diodes, we wanted to equip the Reconfigurable Alford Loop Antenna with appropriate switching control circuitry. The aim of the circuitry design is to add to the antenna the controlling flexibility through common General Purpose Input/Output (GPIO) voltages found in SDR platforms, typically 3.3 V or 5 V. In this thesis, we will show the schematic of the circuit for the PIN diode control along with the scattering parameter (S-Parameter) measurements for evaluating the RF switching performance. In order to reduce complexity and power consumption, we have used an N-Channel MOSFET BSS-138 and a resistive network to provide the appropriate voltage and current to the PIN diode.

The drawback of using DC switching circuitry is that it requires external metallic cables to provide the DC control which may interfere with the antenna's radiation pattern. On the

other hand, the use of optical components as switching elements is preferable because optical control is accomplished using dielectric fiber waveguides which avoid any conductive metallic strips that cause electromagnetic field coupling with the antenna's desired radiation pattern. In this thesis, we also discuss the design of an optically controlled RALA antenna. We provide the optical switching using commercially available devices, where an RF PIN diode is switched ON and OFF though the light illumination of a phototransistor. The performance of this optical approach will be quantitatively analyzed, and the circuit will be implemented as part of the antenna design.

Outcomes

- Design of a compact and planar antenna capable of generating omnidirectional and directional radiation patterns
- First published optical switching circuitry for pattern reconfigurability
- Analyzed and published the intermodulation distrortion (IP3) and the pattern diversity advantage when two reconfigurable antennas are used in a MIMO system
- Extended the basic antenna architecture by designing two multiband solutions for 2.4 and 5 GHz WiFi bands.

Publications

- **D. Patron**, D. Piazza and K. R. Dandekar, **'A wideband planar antenna with reconfigurable omnidirectional and directional radiation patterns'**, *IET, Electronics Letters*, vol. 48, n. 9, 2013.

- **D. Patron**, A. S. Daryoush and K. R. Dandekar, **'Optical Control of Reconfigurable Antennas and Application to a Novel Pattern-Reconfigurable Planar Design'**, *IEEE Journal of Lightwave Technology, Special Issue on Microwave Photonics*, vol. 32, n. 20, Oct, 2014. **(invited paper)**

- **D. Patron**, K. R. Dandekar, and A. S. Daryoush **'Optical Control of Pattern-Reconfigurable Planar Antennas'**, *IEEE International Topical Meeting on Microwave Photonics*, Alexandria, VA 2013.

- **D. Patron**, D. Piazza and K. R. Dandekar, **'A reconfigurable antenna with Omnidirectional and Directional Patterns for MIMO Systems'**, *IEEE International Symposium on Antennas and Propagation APS/URSI*, Orlando, FL, 2013.

- **D. Patron**, and K. R. Dandekar, **'Planar Reconfigurable Antenna with Integrated Switching Control Circuitry'**, *IEEE European Conference on Antennas and Propagation, EuCAP*, The Hague, The Netherlands, 2014.

- M. Williams, **D. Patron**, and K. R. Dandekar, **'Investigation of Switching Techniques for Reconfigurable Multiband Planar Antennas'**, *IEEE International Symposium on Antennas and Propagation APS/URSI*, Orlando, FL, 2014.

- **D. Patron**, A. S. Daryoush, D. Piazza, and K. R. Dandekar, **'Design and Harmonic Balance Analysis of a Wideband Planar Antenna having Reconfigurable Omnidirectional and Directional Patterns'**, *IEEE Wireless and Microwave Technology Conference, WAMICON*, Orlando, FL, 2013.

- **D. Patron**, D. Piazza, and K. R. Dandekar, **'On The Use of Lumped Filters for**

Designing Dual-Band Planar Antennas with Omnidirectional and Directional Radiation Patterns', *IEEE Wireless and Microwave Technology Conference, WAMICON*, Orlando, FL, 2015.

Patents

- **D. Patron**, D. Piazza and K. R. Dandekar, **'Wideband reconfigurable planar antenna with omnidirectional and directional radiation patterns'**, PCT/US 2013/076816.

Miniaturization of Reconfigurable CRLH Leaky-Wave Antennas: The RALA antenna can have wide usage within commercial WiFi routers and access points. However, its form factor does not allow integration within mobile devices, such as laptops or tablets. Therefore, in order to also provide pattern reconfigurability within mobile terminals, in this thesis we discuss the design of a miniaturized Reconfigurable Leaky-Wave Antenna (LWA). As opposed to conventional resonating-wave behavior, Leaky-wave antennas are metamaterial antennas based on the concept of traveling-wave. When an RF signal is applied to the input port, the traveling wave progressively "leaks" power as it travels along the waveguide structure. This leakage phenomenon is directly related to the directivity of the radiated beam. Despite the planar and compact form factor of the LWAs, this antenna technology can fit into wireless base stations but cannot be exploited on mobile devices. In this thesis, we apply a defected ground technique to achieve miniaturization of this metamaterial reconfigurable antenna. In particular, we build upon an improved LWA design in which, as opposed to the conventional LWAs, we greatly reduce PCB manufacturing constraints by avoiding the use of thin interdigital capacitors. We designed the miniaturized LWA by applying a Complementary Split-Ring Resonator (CSRR) underneath each unit cell to achieve

miniaturization of the top layer radiating layout. The unit cell is designed and characterized to resonate at 2.4 GHz and to provide the largest possible beam-steering. Relative to a conventional 2.4 GHz LWA, the overall dimension can be halved while maintaining good impedance matching, a relatively high front-to-back ratio, and good beam steering performance. The miniaturized LWA is designed to exhibit good impedance matching within the 2.41 - 2.48 GHz band for WiFi operations on mobile devices, such as laptops or tablets.

Outcomes

- First published reconfigurable CRLH LWA with improved layout and port symmetry
- First published Direction Of Arrival Estimation using an improved LWA design and a modified MUSIC algorithm
- First reconfigurable CRLH LWA miniaturized using complementary split-ring resonators, suitable for mobile devices.

Publications

- **D. Patron**, and K. R. Dandekar, **'A miniaturized CRLH Leaky-Wave Antenna using Complementary Split-Ring Resonators'**, *IEEE Transactions on Antenna and Propagation*, Under Review.
- **D. Patron**, H. Paaso, A. Mammela, and K. R. Dandekar, **'Improved design of a CRLH Leaky-Wave Antenna and its Application for DoA Estimation'** *ICEAA IEEE-APS APWC Conference*, Turin, Italy, 2013. **(Recipients of the Young Scientist Best Paper Award)**

- H. Paaso, A. Mammela, **D. Patron**, and K. R. Dandekar, **'Modified MUSIC Algorithm for DoA Estimation using CRLH Leaky-Wave Antennas'** *8th International Conference on Cognitive Radio Oriented Wireless Networks (CROWNCOM), Washington, DC, 2013.*

- H. Paaso, A. Mammela, **D. Patron**, and K. R. Dandekar, **'DoA Estimation Through Modified Unitary MUSIC Algorithm for CRLH Leaky-Wave Antennas'** *IEEE 24th International Symposium on Personal Indoor and Mobile Radio Communication (PIMRC), London, UK, 2013*.

Patents

- **D. Patron**, and K. R. Dandekar, **'Miniaturization of Metamaterial Leaky-Wave Antennas'**, 2015 (to be filed).

Wearable Strain Sensor Through Frequency-Reconfigurable Antennas and RFID Technology: Finally, this thesis applies some of the concepts expressed above to design compact frequency-reconfigurable antennas for wearable applications. Specifically, we propose to overcome the current limitation of bulky wearable biomedical devices by applying one of the most innovative techniques for designing wireless strain sensors through the use of resonant antennas. In other words, the mechanical changes of an object can be monitored through elongation or relaxation of the antenna that is attached to it. This change in shape produces a down or up shift of the antenna's resonant frequency. By connecting a small Radio Frequency Identification (RFID) microchip at the antenna input port, the change in the resonant frequency can be detected by looking at the backscattered power (RSSI) received by an interrogating unit. Specifically, a commercially available

RFID reader will keep interrogating the wearable tag, detecting the value of the RSSI and providing indication of elongation or contraction. We will start by showing the design of a flexible tag antenna for the use with a novel inductively coupled RFID microchip, which doesn't require any soldering process since the pads are inductively coupled to the antenna's ports. This choice was motivated by the need for enhancing the tag's sensitivity to physical deformations, as well as avoiding conductive chemicals for the chip connection. Thus, by using the proposed RFID microchips, the physical deformation of the wearable sensor causes impedance variations and coupling reduction between the microchip and the antenna, yielding significant variations of the RSSI. The electrical performance of this antenna will be experimentally demonstrated in terms of input impedance and radiation pattern. Further experiment will validate the strain sensitivity under incremental elongation as well as using a biomedical mannequin simulators.

Outcomes

- First published wireless strain sensor using inductively coupled RFID tag and textile antenna
- First passive, wireless strain sensor for wearable applications that detects contraction and breathing patterns.

Publications

- **D. Patron**, W. Mongan, T. Kurzweg, A. Fontecchio, G. Dion, and K. R. Dandekar, **'On the use of Knitted Antennas and Inductively Coupled RFID Tags for Wearable Applications'**, *IEEE Transactions on Biomedical Circuits and Systems*, Under Review.

- **D. Patron**, T. Kurzweg, A. Fontecchio, G. Dion, and K. R. Dandekar, **'Wireless Strain Sensor through a Flexible Tag Antenna Employing Inductively-Coupled RFID Microchip'**, *IEEE Wireless and Microwave Technology Conference, WAMICON*, Orlando, FL, 2014.

- **D. Patron**, K. Gedin, T. Kurzweg, A. Fontecchio, G. Dion, and K. R. Dandekar, **'A wearable RFID Sensor and Effects of Human Body Proximity'**, *IEEE Benjamin Franklin Symposium on Microwave and Antenna Sub-systems, BenMAS*, Philadelphia, PA, 2014. **(Second Price Best Paper Award)**

- **D. Patron**, T. Kurzweg, A. Fontecchio, G. Dion, and K. R. Dandekar, **'Wearable Biomedical Strain Sensing via Knitted Antennas and Inductively-Coupled RFID Tags'**, *IEEE 9th Annual International Conference on RFID,* San Diego, CA, 2015.

Patents

- G. Dion, T. Kurzweg, A. Fontecchio, M. Owen, **D. Patron**, and K. R. Dandekar, **'Smart Knitted Fabrics, usage of the yarns and knots to create wireless devices (e.g. RFID devices) and other circuit components'**, PCT/US 2014/020681.

- G. Dion, T. Kurzweg, A. Fontecchio, M. Owen, **D. Patron**, and K. R. Dandekar, **'Smart Knitted Fabrics, active and passive technologies for the Bellyband'**, Provisional US 61/906,883.

1.3 Thesis Outline

This dissertation is organized as follows: in Chapter 3, we discuss the design of the Reconfigurable Alford Loop Antenna, comparing simulation and experimental results. In

this chapter, we extend the switching control concept by showing an optical switching circuit, which allows eliminating the DC wires for the states' control. Due to the form factor of the RALA antenna, in Chapter 4, we propose an even more compact design for mobile terminals. We apply a novel miniaturization technique to an improved design of Leaky-Wave Antenna, achieving 47 % of size reduction and maintaining large beam steering capabilities. In Chapter 5 we discuss the design and the application of a wearable frequency-reconfigurable antenna, which allows biomedical sensing through RFID technology. Chapter 6 concludes this dissertation, summarizing the main contributions and highlighting the future direction of this research field. In Appendix A, we provide a survey of the current commercialization status of reconfigurable antennas along with a useful analysis of the modes of university technology commercialization.

Chapter 2: Background

2.1 Benefits of Reconfigurable Antennas in MIMO Systems

In a wireless communication system, the transmission medium is the radio channel between a transmitter TX and a receiver RX. Channel models are used as representations of this medium. They are used to predict the communication performance and obtain a realistic performance evaluation of the system. When the communication system is equipped with an array of antennas at both the TX and RX, the system is called Multiple-Input Multiple-Output (MIMO). The multiple copies of the signal at the RX can be combined constructively through optimal signal processing algorithms, improving the link capacity, mitigating interference, and strengthening the link [31]. This technology is currently supported by modern communication standards such as IEEE 802.11, 3GPP LTE-A [32] and IEEE WiMax [33].

Wireless channels are challenged by signal attenuation, noise, and numerous potential sources of interference. In particular, a wireless communication link is susceptible to fading and interference. The most notable physical challenges to wireless communication systems are [34]:

- Multipath propagation, which is the path randomness associated with different possible reflections
- Spectrum limitations, which are defined by standard regulations

- Energy limitations, which are defined by standard regulations as well as safety concerns

- User mobility.

The source of these challenges is the fact that the signal from TX to RX can travel through a large number of different propagation paths. The ideal case is the Line of Sight (LOS), which is the straight line propagation between TX and RX. However, in real scenarios, the signal is usually reflected or diffracted by different interacting objects in the surrounding environment. Each multipath may have different delays, amplitude of the signal, angles of arrivals, or phase shifts. However, one of the most important phenomenon that affects wireless channels is the *fading*. This is a natural attenuation of the signal due to either the distance between TX and RX or to the different multipath components. Specifically, we can divide this phenomenon into two cases:

Small-scale fading, which describes the constructive or the destructive interference that may occur to multipath components that are combined at the receiver. Sometimes, even a small movement can result in a large change in signal amplitude. A common example is the loss of FM radio signal within a small distance such as a stop-and-go traffic.

Large-scale fading, which is associated with the amplitude variations of the different multipath components or the distance-dependent attenuation in LOS [35]. Shadowing is an example of such phenomenon and it is typically due to obstacles, such as surrounding buildings.

The Signal-to-Noise Ratio (SNR) is the most commonly used figure of merit to evaluate the quality of a received signal. The SNR is inversely proportional to the distance between

TX and RX, and it expresses the ratio between the desired signal at the receiver and the noise.

One of the best solutions to cope with the physical challenges described above, is by enabling the MIMO communication system to select the optimal wireless channel. Selecting the optimal channel allows to achieve the highest SNR or meet the required quality of service. In this regard, reconfigurable antennas offer several degrees of freedom to accomplish this task. As opposed to standard ”static” antennas, reconfigurable antennas possess frequency or radiation pattern agility to select the best wireless channel [36, 37, 13, 38]. This agility can be described as a function of the frequency or radiation diversity that an electrically reconfigurable antenna can offer. The principle of diversity is to ensure that the same information reaches the RX on statistically independent channels. There are five different types of diversity:

Spatial Diversity: Is the oldest and simplest form of diversity, however it is still widely used in communication systems. The signal from TX is received at an array of antenna elements at the RX side, and sophisticated signal processing techniques allows improvement to the link through constructive combination schemes. However, the performance of these signal processing algorithms is influenced by the correlation between the signal between the antenna array elements. The most important aspect in designing diversity antennas is to ensure high uncorrelated signals at their respective RF ports. The numerical evaluation of the correlation coefficient is a function of the spacing between the elements as well as the interaction between each radiation pattern.

Temporal Diversity: Since the wireless propagation channel is time-variant, signals that are received at different times are uncorrelated. In order to enhance the decorrela-

tion, the temporal distance must be at least $1/2v_{max}$, where v_{max} is the maximum Doppler frequency. Examples of techniques that used temporal diversity are: repetition coding, automatic repeat request, and a combination of interleaving and coding.

Frequency Diversity: it is the principle for which the resonant frequency of the antenna can be adapted to transmit at different frequencies. If these frequencies are spaced apart by more than a coherent bandwidth of the channel (i.e. frequency interval over which two frequencies of a signal are likely to experience comparable or correlated amplitude fading), then their fading is approximately independent. As a result, the probability that the signal is in deep fade at two of more frequencies is low. Some of the modern modulation techniques that take advantage of frequency diversity are: Time Division Multiple Access (TDMA), Code Division Multiple Access (CDMA), Carrier Division Multiple Access (CDMA), and frequency hoping (used in the Bluetooth standard). These methods allow improvement to the wireless link without wasting bandwidth. In Chapter 5 of this dissertation, the principle of frequency diversity is exploited for designing wearable sensors through textile antennas and RFID technology.

Angle Diversity: Deep fading may occur when multipath components come from different directions and interfere destructively. When two elements on an antenna array with different patterns receive different weighted multipath signals, they interfere differently for the two antennas. Often, angle diversity can be used in conjunction with spatial diversity in order to enhance the decorrelation of the signals received at closely spaced antennas. Even if the antennas individually have the same pattern, when they are close to each other in array form the interaction and coupling [21] between them change and re-shape the radiation pattern.

Polarization Diversity: Polarization of a radiated wave is defined as the property of an electromagnetic wave describing the time-varying direction and relative magnitude of the electric field vector. In order words, polarization is the curve traced by the end point of the vector representing the electric field observed along the direction of propagation [21]. In a wireless channel, horizontally and vertically polarized multipath components propagate differently, as the reflection and diffraction effects depend on polarization. Therefore, for a determined polarized array of antennas at the TX and RX, the potential change in polarization due to multipath effects may lead to depolarization. The fading of signals with different polarizations is statistically independent, and the use of a dual-polarized antenna with separate signal processing can offer a diversity advantage.

Several antennas can be designed to add pattern and polarization diversity to MIMO systems. In the next sections we provide an overview of the current most important trends and techniques in the field of pattern reconfigurable antennas.

2.2 Pattern Reconfigurable Antennas

The radiation pattern of an antenna is determined by the current distribution along the metallic design, accounting for its magnitude and phase. In order words, different current paths lead to different spatial distribution of the radiated field. After choosing the antenna design for the desired impedance and radiation characteristics, the current distribution can be altered to generate different radiation patterns. The most cost-effective and feasible method for changing the current path is to introduce lumped components that can electrically alter or load the metallic layout. These antennas employ embedded switches or variable capacitors to change the current distribution on the metallization of the active el-

ement [39, 40]; or may employ an active antenna element surrounded by passive elements (i.e., parasitic elements) loaded with variable capacitors or connected to switches [41, 42]. Another interesting approach is the design of Composite Right/Left-Handed (CRLH) Reconfigurable Leaky-Wave Antennas (LWAs), a two-port metamaterial design that is able to steer its directive beam from broadside to backward and forward angles [43].

2.2.1 Antennas with Embedded Switches

RF switches can be used to alter the current distribution of a microstrip antenna and change its radiation pattern. These switches can be solid state (PIN diodes, Single-Pole Double-Throw switches) [5, 44], electro-mechanical (RF MEMS), optical [45], or thermal [46]. Two common approaches for designing reconfigurable antennas using embedded switches are *i)* Alter a single radiating element through variations of the electrical length, *ii)* surround the main radiator with switchable parasitic elements.

Single element approach: One of the basic principles for designing a reconfigurable antenna is to change its electrical length. In [1] the authors present the design of a reconfigurable microstrip dipole antenna with PIN diodes used to extend or reduce the electrical length of the dipole, Fig. 2.1. By turning OFF the two switches the configuration is set to half-wavelength dipole, while by turning ON the switches it changes to a three-quarter wavelength dipole. When two of these antennas are coupled to form an array, there are a total of four pairs of short and long configurations, which yield four different radiation patterns.

In [2] the authors present the design of a reconfigurable circular patch antenna. The principle underlying this architecture is that the radiation pattern of a circular patch antenna

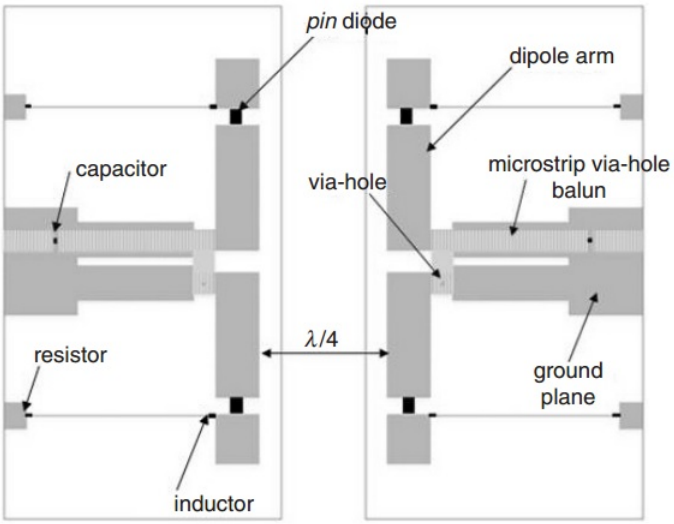

Figure 2.1 Reconfigurable printed dipole antenna array [1].

is directly related to its radius [21]. In fact, the authors design an inner circle surrounded by an external ring. Then, by populating the two sectors using PIN diodes, the antenna can be switched from a short radius patch (PIN diodes OFF), to a larger radius patch (PIN diodes ON), Fig. 2.2. Furthermore, the antenna has two RF ports, and two different radiation patterns can be excited at each port by varying the radius through the set of PIN diodes.

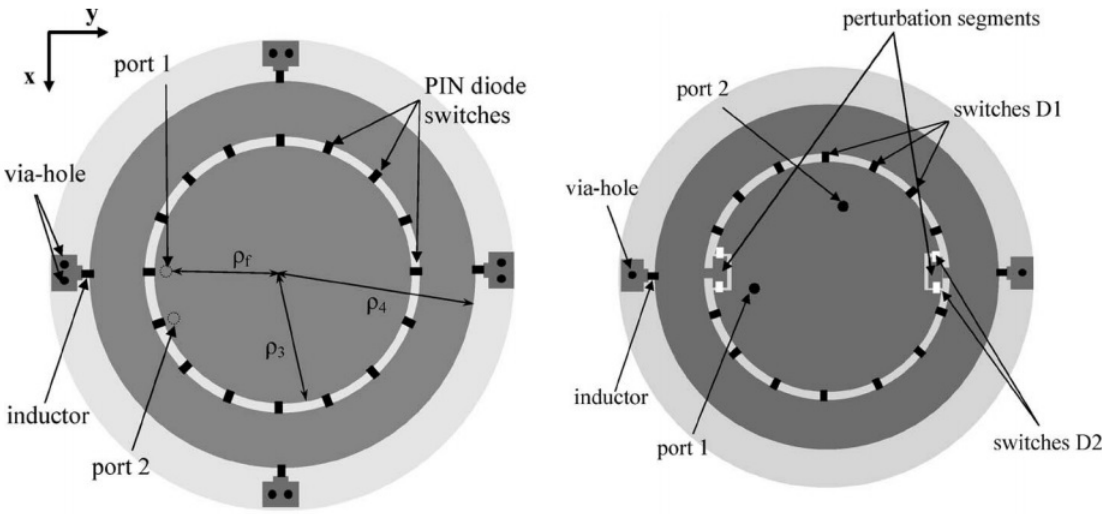

Figure 2.2 Reconfigurable circular patch antenna [2].

Other antenna architectures utilize switches on the ground plane instead of the main radiating element. In [3] the proposed pattern reconfigurable antenna is designed with a top layer circular radiating element, with circular slots etched on the ground plane and switched through PIN diodes. By turning ON and OFF the two PIN diodes, the antenna can operate in two different modes tilting the two main lobes about 35°.

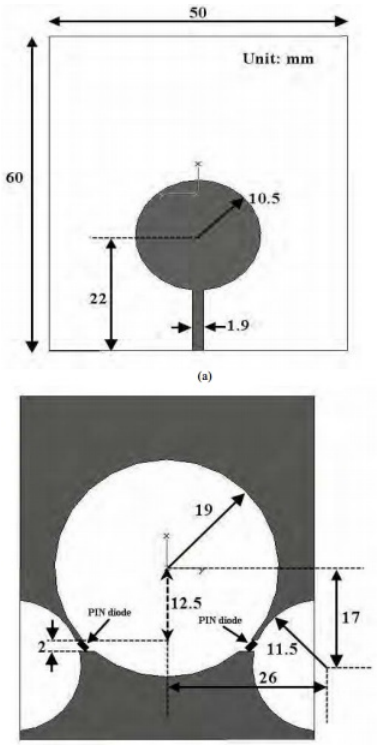

Figure 2.3 Reconfigurable circular slot antenna [3].

Switchable parasitic elements approach: So far we reported switchable reconfigurable antennas where the switching components are mounted on the main radiator. However, other architectures use a single radiating element surrounded by switchable parasitics [47]. This approach is usually preferable under applications that require to steer a directional beam around the entire azimuth plane (plane orthogonal to the main radiator). Typically, this type of reconfigurable antennas are accomplished by designing a central omnidirec-

tional antenna surrounded by switchable parasitic elements. For example, in [4] the authors designed a Z-shaped radiator, which is characterized by omnidirectional radiation in the plane of the antenna, surrounded by radial sectors (the parasitic elements). These parasitic elements are connected to each other by means of PIN diodes, Fig. 2.4(a). When all the PIN diodes are OFF the antenna radiates its original omnidirectional beam. On the other hand, when a set of PIN diodes that connect multiple parasitics are activated they act as reflectors, generating a directional beam in the opposite direction.

A more recent architecture utilize a similar principle, but has the advantage of reducing the overall dimensions [5]. The main radiator is a zeroth-order loop antenna, which is a composite right/left-handed structure that makes the antenna size independent from the frequency of operation. The main radiator is made by a cascade of 4 unit cells to form a loop, populated with lumped inductors and capacitors to generate a zero order mode and thus excite an omnidirectional pattern in the azimuth plane. Eight parasitic elements are placed around the central loop and connected to one another through PIN diodes to provide the pattern reconfigurability, Fig. 2.4(b). A total of eight directional beams with 45° resolution, and one omnidirectional beam can be generated by changing the PIN diodes configuration.

Despite the planar form factors, these antenna architectures tend to employ a large number of lumped components, which challenge their effective commercialization. Other reconfiguration techniques use photoconductive switches such as photodiodes or phototransistors [39, 48, 49], or thermal switches [50].

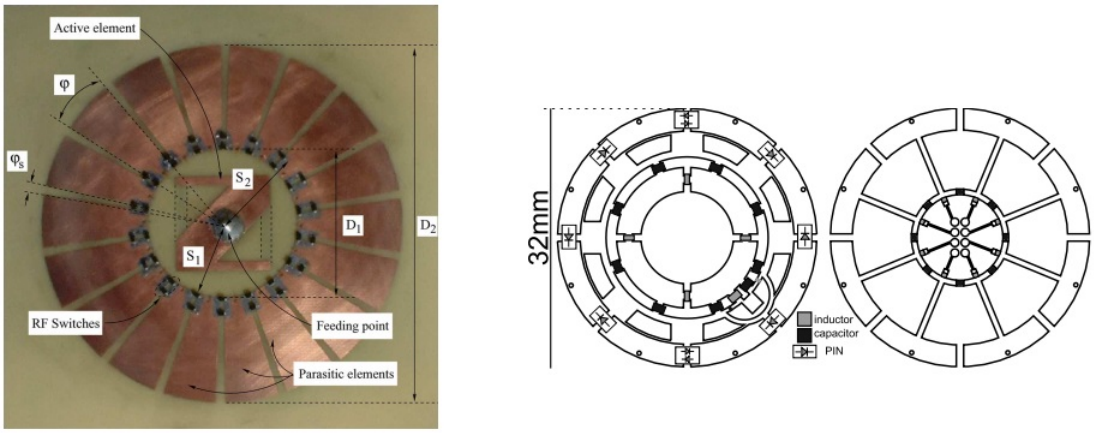

(a) (b)

Figure 2.4 (a) Planar electronically beam steering antenna [4]. (b) Reconfigurable Zeroth-order loop antenna, top and bottom view [5].

2.2.2 Antennas with Variable Capacitors

The use of switching components such as PIN diodes is a convenient solution that relies on a discrete set of states (switches can be ON or OFF) and fast switching time. However, other reconfigurable antennas resort to varactor diodes. This component is an electrically tunable capacitor, which can be varied through an external DC voltage. Such antennas are typically characterized by larger and continuous tunability (varactor diodes are varied through a continuous DC voltage range). For instance, Electronically Steerable Passive Array Radiatior (ESPAR) antennas is an attractive architecture that can be used as an adaptive beamformer thanks to its large beam and null steering capability [6, 51]. Thanks to the coupling between the central radiating element and the surrounding switchable reflectors/directors, the gain is typically higher than single element antennas. As an example, a 7 element ESPAR antenna [6] can achieve continuous beam steering with 8 dBi of gain around the entire azimuth plane. The major drawback of ESPAR antennas is the fact that the design requires

vertical elements mounted on top of a substrate, which makes the architecture large and unsuitable for small WLAN systems [6].

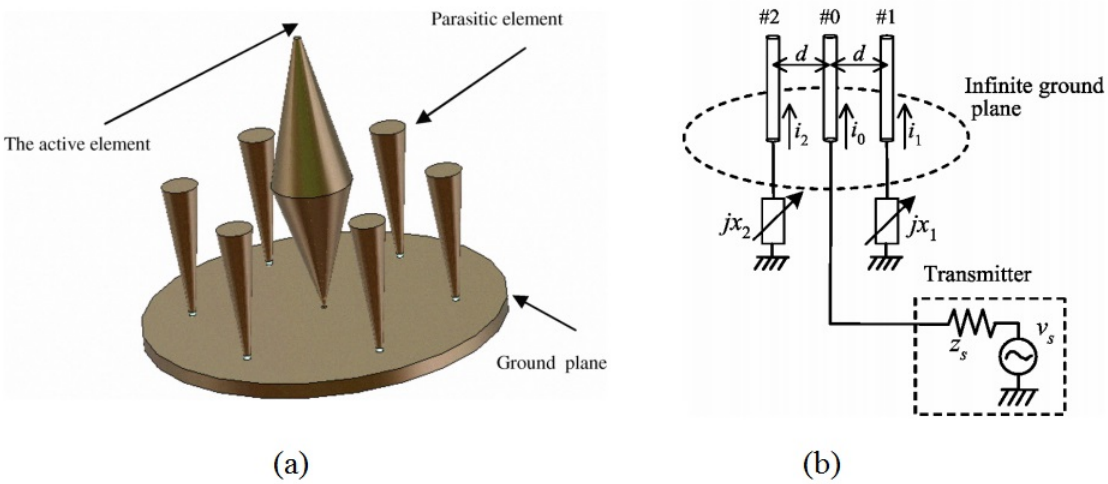

Figure 2.5 (a) Example of ESPAR antenna architecture [6]. (b) Schematic of basic configuration and controlling principle [7].

Other more compact architectures employ varactor diodes for changing the current characteristic on the main radiator and vary the radiation pattern. For example, a patch top-loaded monopole antenna loaded with varactor diodes was presented in [52]. By varying the capacitive loading of the varactors, the antenna can generate two directional patterns and a single omnidirectional pattern. Other architectures use a single microstrip element, such as patch antennas, coupled to multiple parasitic antennas via varactor diodes [53]. The tunable mutual coupling between the main and the parasitic elements replaces the traditional need of phase shifters. In other words, by changing the mutual coupling through the varactors, the beam can be electronically steered.

2.2.3 Electronically Controlled Leaky-wave Antennas

Of particular interest, as part of the subset of reconfigurable antennas, is the design of Composite Right/Left-Handed (CRLH) Reconfigurable Leaky-Wave Antennas (LWAs), a two-port metamaterial-based design that is able to steer its directive beam from broadside to backward and forward angles [9, 8]. Electromagnetic metamaterials are widely defined as *artificial effectively homogeneous electromagnetic structures with unusual properties not readily available in nature.* Where, an *effectively homogeneous structure* is a structure whose average cell size *p* is much smaller than the guided wavelength λ_g. In other words, the average cell size should be smaller than $p < \lambda_g/4$.

The concept of metamaterials was first introduced by Viktor Veselago in 1967, through a theory describing "substances" LH that allow the propagation of the electromagnetic waves with the electric field, the magnetic field, and the phase constant vectors building a *Left-Handed* (LH) triad, whereas in conventional materials this triad is know to be *Right-Handed* (RH). Despite that no LH materials were discovered, 30 years later an artificially effectively homogeneous structure was developed by Smith and colleagues [54]. Although very exciting from the physical view point, the initial metamaterial structures seemed not practical for engineering purposes. The main limitations were the high losses and narrow bandwidth. Eventually, in 2002 three groups introduced almost simultaneously the first approach to metamaterials using transmission lines [55, 56, 57]. While a conventional transmission line can be modeled as a series inductance and a shunt capacitor, the LH tranmission line is modeled with a series capacitance and a shunt inductance, Fig. 2.6(a)(c). Because of their non-resonant nature, metamaterial tranmission lines can be utilized to

exhibit low loss and broad bandwidth, opening new engineering opportunities.

The concept of composite right/left-handed (CRLH) metamaterials was introduced in [58]. The transmission line structure consists of a series capacitor C_L and a shunt inductor L_L to provide the left-handedness. Whereas, the series inductor L_R and shunt capacitor C_R provide the right-handedness. In addition to the design of guided-wave transmission lines, where the energy remains confined within the waveguide, CRLH metamaterials opens new venues for designing antennas as well. CRLH structures offer unique radiation properties, that can be used for beam forming in MIMO systems. In fact, if a metamaterial structure is open to free space and supports fast-wave mode, called leaky-wave, it radiates and can be used as an antenna. A leaky-wave is a traveling wave that progressively leaks out power while it propagates along the metamaterial waveguide.

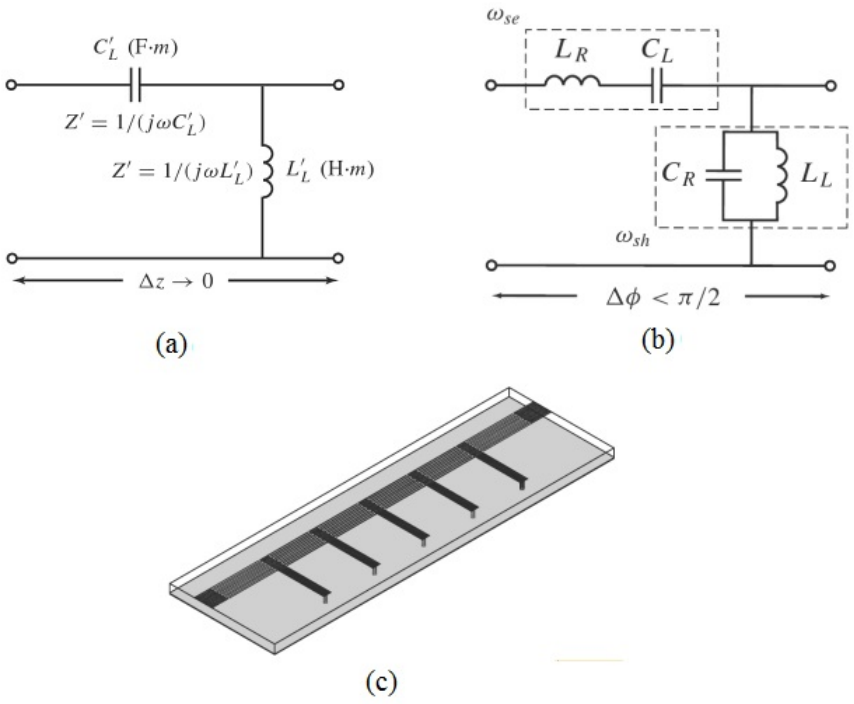

Figure 2.6 (a) Circuit model of a hypotetical uniform LH transmission line. (b) Circuit model of a Composite Right/Left-Handed (CRLH) transmission line. (c) Planar LH transmission line in microstrip technology. [8]

The reconfigurable CRLH LWA can be realized as a two-port radiating element with tunable radiation properties. The layout is made by a series of *N* metamaterial unit cells [8], cascaded in order to create a periodic structure from port 1 to port 2, as shown in Fig. 4.1. Unlike conventional resonating-wave antennas, the LWA is based on the concept of a traveling-wave. When a radio-frequency signal is applied to one of the input ports, the traveling wave "leaks" out energy as it progressively travels toward the second port. This energy leakage determines the directivity of the radiated beam and is a function of the propagation constant along the structure.

In LWAs, the radiation properties are determined by the complex propagation constant $\gamma = \alpha - j\beta$, where α is the attenuation constant and β is the phase constant. While the former corresponds to a loss due to the leakage of energy, the latter determines the radiation angle of the main beam. Additionally, the relationship between β and the wavenumber k_0 defines the regions of operation.

Several voltage-controlled LWAs have been developed in the literature [9, 59]. The structure is made by series of interdigital capacitors and shunt stubs, including voltage-controlled varactor diodes to change electronically the propagation constant β. The angle of the main beam can be determined by the following equation:

$$\theta = \sin^{-1}\left(\frac{\beta}{k_0}\right) \tag{2.1}$$

where, the propagation constant β can be varied through the varactor diodes that can

vary C_R and C_L:

$$\beta_{(\omega)} = \frac{1}{p}\left(\omega\sqrt{L_R C_R} - \frac{1}{\omega\sqrt{L_L C_L}}\right) \tag{2.2}$$

In this way, the antenna's directional beam can be steered from broadside to backward θ_1 and forward θ_2 end-fire directions at a given frequency, Fig. 4.1. In other words, the introduction of varactor diodes allows for a change in capacitance through the reverse bias voltage and the propagation constant β becomes a function of the diode's voltage.

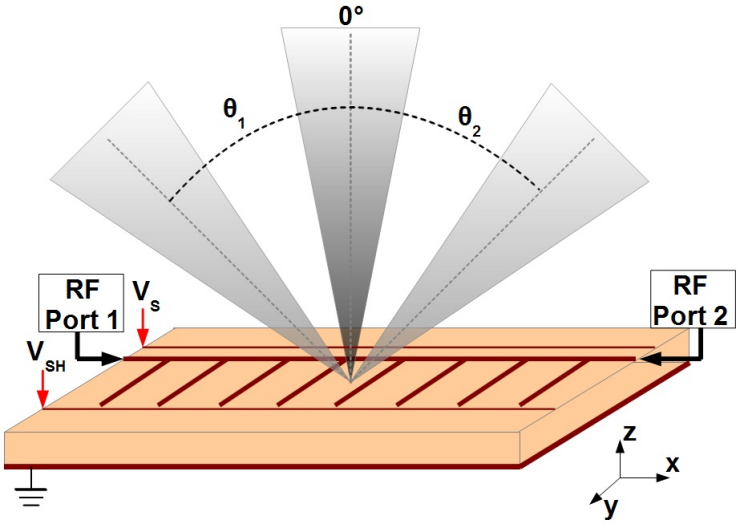

Figure 2.7 Sketch of a two-port CRLH Reconfigurable Leaky-Wave antenna with details of the beamsteering capability.

Preliminary CRLH reconfigurable antennas utilized the same voltage to control the series and the shunt varactors [9], V_b in Fig. 2.8(a) and (b). A more recent architecture, utilizes two different voltages to control the series and the shunt varactors separately. This approach allows for improved impedance and beam control [10]. The series portion is designed with two interdigital capacitors and two varactor diodes D_{S1} and D_{S2} connected in parallel. The shunt portion is composed of a stub and a varactor diode D_{SH} in series.

The capacitor C acts as DC-block for the two bias lines V_S and V_{SH}, Fig. 2.8(c) and (d). Three $\lambda/4$ microstrip transformers provide the DC bias to the diodes. The aforementioned characteristics make the reconfigurable LWA a very attractive solution for beamforming within commercial WiFi routers and access points.

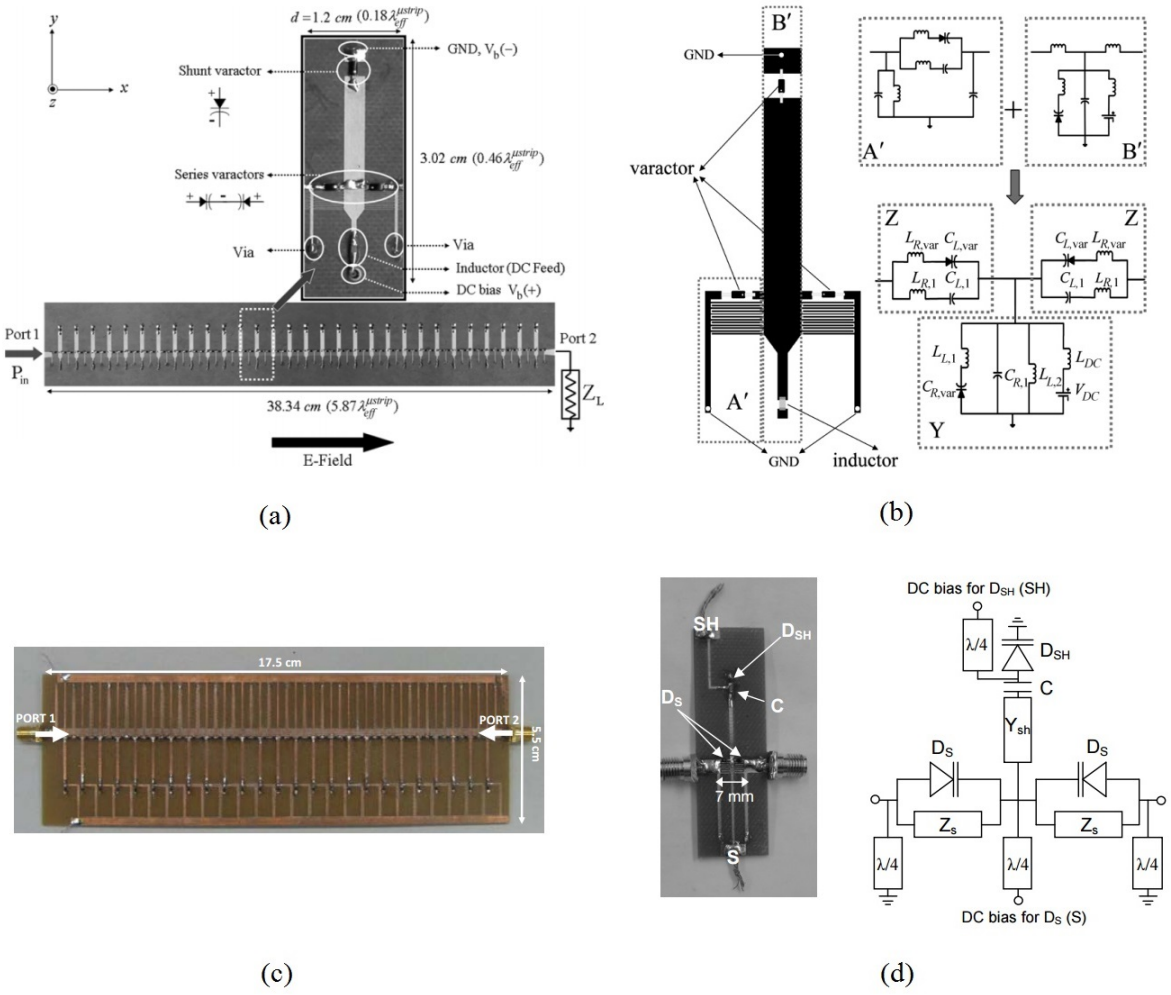

Figure 2.8 (a) CRLH LWA controlled with a single voltage and (b) detail of metamaterial unit cell [9]. (c) CRLH LWA controlled with two voltages and (d) detail of the metamaterial unit cell [10].

Chapter 3: Reconfigurable Alford Loop Antenna

Reconfigurable antennas have been proposed as a low-cost solution to leverage pattern diversity and to improve the spectral efficiency of wireless links [38]. However, in some applications such as WLAN, distributed MIMO [30], or complex multipath propagation environments, the employment of horizontally polarized antennas with omnidirectional patterns may result to be more convenient. In particular, experimental analysis have shown that the freedom of switching between an omnidirectional and directional radiation patterns can improve the data throughput under the following conditions: *i)* Crowded user scenarios, *ii)* Complex multipath and rich scattering environment, and *iii)* fast-changing wireless channels.

Recently, a compact planar design was developed for a reconfigurable antenna that combines omnidirectional and directional pattern realizations [5]. However, the reactive components around the active element increases the Quality factor Q [21], resulting in a narrow bandwidth. Conversely, a compact planar design based on an Alford loop has been shown to have a wider bandwidth [60, 61], but is only able to generate a single, static omnidirectional beam. In this section we describe the design and the experimental analysis of a reconfigurable, broadband, square-shaped Alford loop antenna that can generate both omnidirectional and directional radiation patterns by switching between the elements.

3.1 Native Design

One of the most simple and versatile antenna types is the loop antenna. The layout can be designed through a square, triangle, ellipse, circle, and other forms. However, because of its simplicity, the circular loop is the most popular form among antenna designers. The monopole antennas are one of the most widely used antennas for mobile devices, while the loop antennas found very few applications due to size and impedance characteristics. However, loop antennas posses three main advantages [21]:

- High noise immunity, which makes them very attractive for an interfering and fading environment like that of mobile communications
- Within handheld devices, both vertical and horizontal placement present attractive radiation characteristics
- The characteristic impedance makes loop antennas attractive for integration with balanced amplifiers.

In general, a small loop antenna is equivalent to an infinitesimal magnetic dipole whose axis is perpendicular to the plane of the loop. In other words, the fields of a small loop are the same as those radiated by an infinitesimal magnetic dipole. Usually, loop antennas can be classified into two categories:

- *Electrically Small loop antennas:* whose overall circumference is $\mathrm{C} < \lambda/10$.
- *Electrically Large loop antennas:* whose overall circumference is $\mathrm{C} \sim \lambda$.

Electrically small antennas tend to be poor radiators and they are seldom employed for radio communications. They find usage within receivers where the signal-to-noise ratio

is more important than efficiency. Furthermore, they are utilized as near-field probes at microwave frequencies. The field radiated by these loops is uniform around the plane of the loop with a null along the axis of the loop. This radiated field is called *omnidirectional*.

In the case of electrically large loop antennas, the radiation efficiency is higher and comparable to other standard radiatiors. These loops are used primarily in directional arrays, such as Yagi-Uda, helical, and other directional antennas. For these loops, the radiated field is directed toward the axis of the loop forming an end-fire antenna.

Stemming from above, it is very desirable to take advantage of the noise immunity of loop antennas by designing an antenna having dimensions comparable to electrically small loops but performance similar to electrically large loops.

In 1942, Andrew Alford ad A. G. Kandoian published a paper entitled *"Ultrahigh-frequency Loop Antennas"* [11]. The authors describe the design procedure of loop antennas that radiates horizontally polarized waves. This new approach for design loop antennas is significant because it maintains the typical uniform current distribution and omnidirectional radiation pattern of electrically small antennas, while ensuring performance comparable to electrically large loops with a smaller form factor.

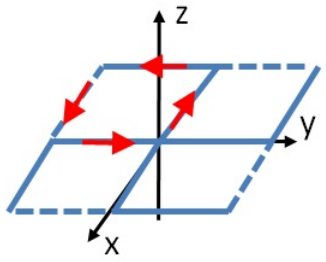

Figure 3.1 Sketch of the four radiating elements comprising the ultrahigh-frequency loop [11]. The current distribution in one of the elements is shown with red arrows.

The type of loop utilized in this dissertation is depicted in Fig. 3.1. The loop is made by four folded elements in which the current distribution is in phase, and having direction as shown by the red arrows in Fig. 3.1. The center of the geometry is the location of the RF input port. The length l of each radiator is assumed small in comparison with the frequency wavelength λ. The magnetic field produced by the four radiators of the loop antenna is the vector sum of the individual fields. At any given point in far-field, the magnetic and electric field can be summarized as $H_x = E_y$ and $H_y = E_x$. Since the efficiency of loop antennas depends on the radiation resistance and the loss resistance of the conductors, the computed radiation resistance for the ultrahigh-frequency loop antenna is [11]:

$$R = 320 \left(\sin \frac{\pi l}{\lambda} \right)^4 \tag{3.1}$$

which is a special case of a more general result which holds true for any electrically large loop antennas [21]. Generally speaking, the efficiency can be defined as:

$$\eta = \frac{\text{radiation resistance}}{\text{radiation resistance} + \text{loss resistance}} \tag{3.2}$$

which highlights the importance of having high radiation resistance for achieving an ideal unitary efficiency.

3.2 Reconfigurable Alford Loop Antenna Design

In this section, we describe in more details the design of the Reconfigurable Alford Loop Antenna (RALA) along with its major characteristics. The layout is made of four pairs of 90° microstrip elements arranged symmetrically between the top and bottom layer of a

standard FR-4 substrate having a thickness of t = 1.6 mm and a dielectric constant ϵ_r = 4.4, as shown in Fig. 3.2. The eight gaps, four on the top and four on the bottom layers, have the proper length (1.1 mm) to include single-pole single-throw RF switches (Pin Diode SKYWORKS model SMP1345-079LF [62]) in order to selectively connect the branches to the center feed port. The antenna is fed by a coaxial SMA, having the ground connected to the bottom layer and inner conductor soldered to the top layer through a via hole.

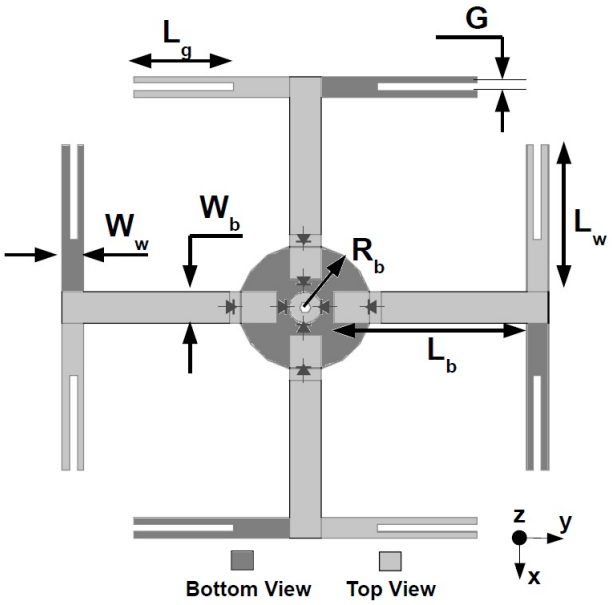

Figure 3.2 Layout of the first Reconfigurable Alford Loop Antenna, for the frequency of 3.8 GHz

Using a commercial full wave electromagnetic field simulator (HFSS^{TM})[63], the design has been optimized to operate at a center frequency of 3.8 GHz for potential use in ultrawideband systems [64]. The layout of the proposed antenna is shown in Fig. 3.2. The complete design fits within a 40 x 40 mm area and the dimensions are: R_b = 5.8 mm, W_b = 3 mm, W_w = 2 mm, L_b = 19.4 mm, L_w = 17 mm, L_g = 9 mm, G = 1 mm. The wings' slot length has been tuned for wider bandwidth, while the radii of the top and bottom circles were designed to improve the impedance matching in both modes of operation, resulting in

a simple feeding network.

3.2.1 Radiation Characteristics

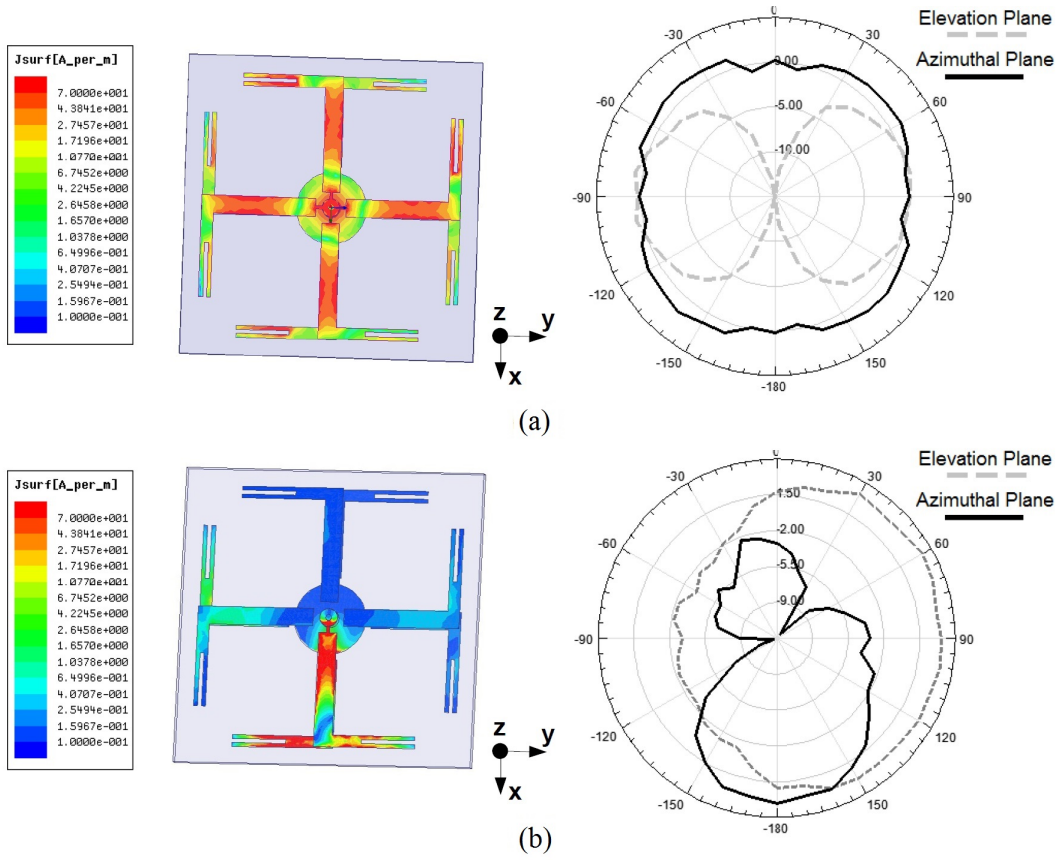

Figure 3.3 Simulation of the Reconfigurable Alford Loop Antenna. (a) Four active pairs and radiation of omnidirectional beam. (b) Single active pair and radiation of a directional beam.

If the four pairs of branches are connected to the center feed port (all pin diodes in forward bias), the current distributions will be uniform along the microstrip elements, as shown Fig. 3.3a. In this way, the radiating structure resembles the ultrahigh-frequency loop antenna proposed by A. Alford in [11], which radiates an omnidirectional radiation pattern with horizontal polarization.

Directional modes are achieved by connecting just one pair of the branches to the center

feed port (two pin diodes in forwad bias), while the other three disconnected branches act as reflector elements. The amount of energy coming from the radiating element directed toward the disabled pairs undergoes a reflection, pointing the beam in the direction of the excited pair as shown in Fig. 3.3b. To enhance the front-to-back ratio in directional mode, the reflectors' effect has been maximized by designing the Alford loop antenna with 90° squared branches.

Simulations have shown that the contribution of the disconnected pairs is twofold. To give an example, assume the scenario where the active pair is the one in positive *x* direction, as depicted in Fig. 3.3(b). Among the disconnected elements, the contribution of the only parallel pair (located in -*x* direction) is to compress the beam along the x axis, generating two peaks toward the end-fire directions ($\pm$ *z*). On the other hand, a major contribution to a clear directionality is given by the two parallel pairs (located in +*y* and -*y* directions). The effect they provide on the directivity is for a broadside radiation directed normal to the excited pair. The four pairs of identical elements allow for the generation of a total of four distinct directional patterns spaced 90° between each other.

3.2.2 Comparison Between Numerical and Experimental Results

The proposed antenna was etched on a conventional 1.6 mm thick FR-4 substrate using a milling machine. The board was populated using PIN diode RF switches and the DC bias voltages were provided through 220 nH inductors. The pin diode SMP1345 requires a forward voltage of 0.89 V (I = 10 mA), where insertion loss and isolation are respectively 0.23 dB and 12.6 dB. Using an Agilent N5230A network analyzer, we measured the return loss or, S_{11}, which describes the impedance integrity between the antenna's port and the

feed line. Fig. 5.1 shows the comparison between simulation and measurement for both modes of operation centered at 3.8 GHz: in omnidirectional mode the measured antenna covers a 10 dB return loss (RL) bandwidth of 400 MHz and a 6 dB RL bandwidth of about 650 MHz, while each directional mode covers a 10 dB RL bandwidth of 400 MHz and a 6 dB RL bandwidth of 1 GHz . The small discrepancy between simulation and measurement may be due to the manufacturing process.

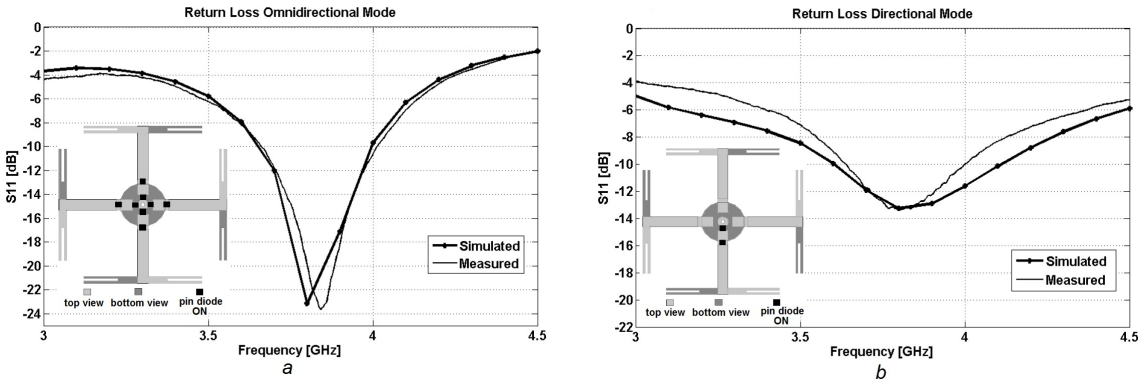

Figure 3.4 Simulated and measured return loss for both the omnidirectional (a) and the directional (b) modes.

The radiation patterns characterize the variation of the far-field radiation magnitude as a function of angular steps at a specific frequency. In Fig. 3.5, the measurements performed in the anechoic chamber for both modes of operation at 3.8 GHz are shown: the omnidirectional mode has 1.8 dBi of gain while each directional mode has 4 dBi gain and Half-Power Beamwidth (HPBW) of about 55°. By switching between each pair of branches, the antenna can generate four identical directional modes with 90° between each mode as shown in Fig.3.5(c).

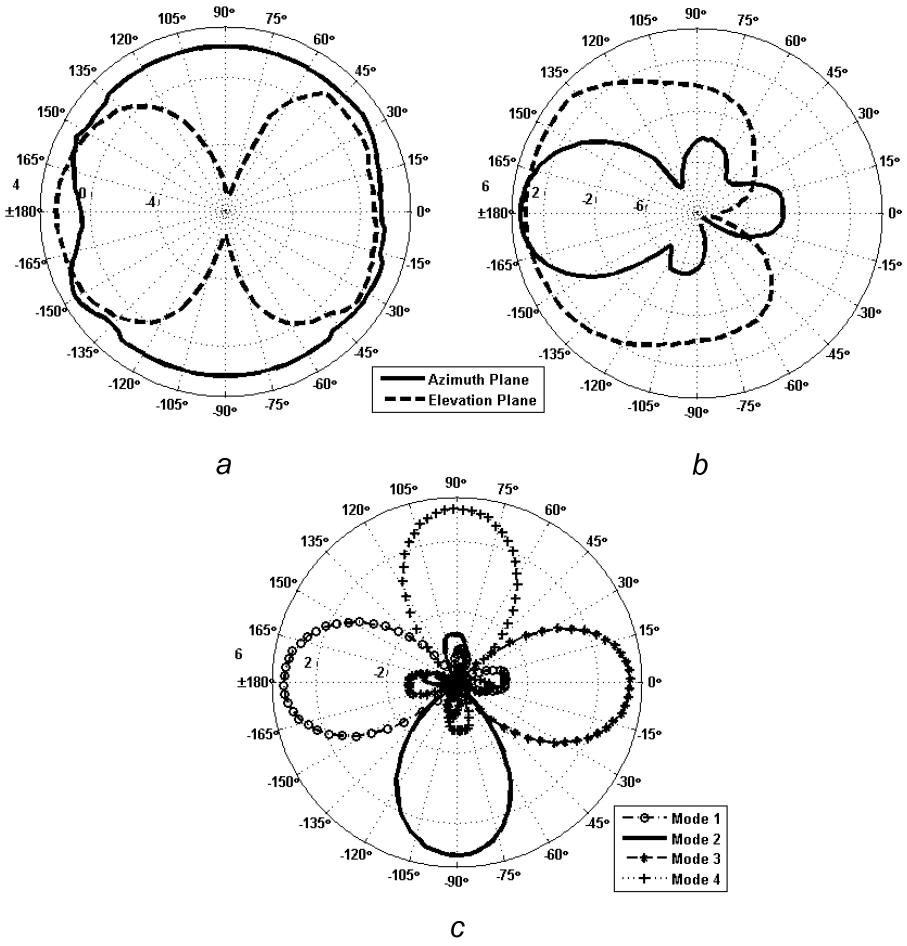

Figure 3.5 Measured radiation patterns for both omnidirectional (a) and directional modes (b). In (c) is shown a summary of the directional beams.

3.2.3 Integration of Switching Control Circuitry

In order to electronically switch between the elements, the RALA requires proper RF switching devices and DC control circuitry. This can be accomplished by using PIN diodes which are single-pole-single-throw (SPST) switches that operate in the RF domain. For our purpose we have used a Skyworks™ SMP1345 [62], a PIN diode specifically designed to operate up to 6 GHz.

In order to avoid external control boards for driving the PIN diodes, we wanted to equip

the antenna with appropriate switching control circuitry [65]. The aim of the circuitry design was to add to the antenna the flexibility for use with common GPIO voltages found in SDR platforms, typically 3.3 V or 5 V. In Fig. 3.6, we show the schematic of the circuit for the PIN diode control along with a picture of the transmission line built for scattering parameter measurements. In order to reduce complexity and power consumption, we have used an N-Channel MOSFET BSS-138 and a resistive network to provide the appropriate voltage and current to the PIN diode (V = 1 V, I = 10 mA). In essence, when the control voltage V_G is at logic level 0, V_{PIN} is equal to zero, turning the PIN diode to the OFF state (high RF isolation). On the other hand, when V_G rises to higher voltage levels (greater than the MOSFET's threshold voltage), it enables the current to flow through the circuit, thus turning ON the PIN diode (low RF insertion loss). The inductor L = 220nH acts as a RF-choke preventing the RF leakage along the DC circuit.

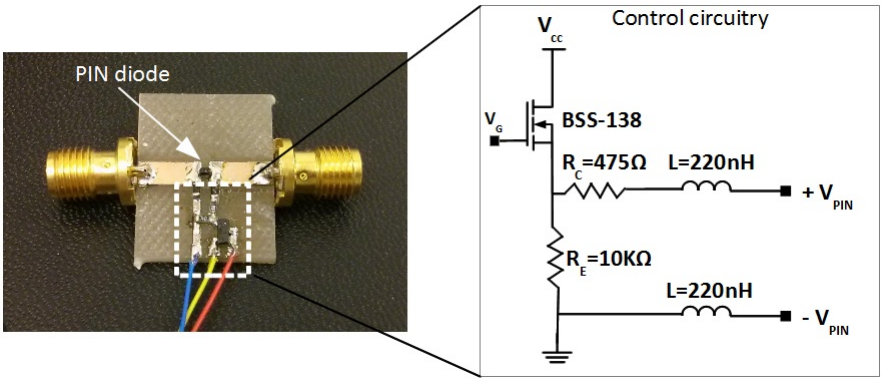

Figure 3.6 Transmission line used for PIN diode measurements and control circuitry schematic.

Scattering parameters of the circuitry described in Fig. 3.6 were measured within the bandwidth of interest, from 2 GHz to 3 GHz. By considering the two cases V_{CC} = 3.3V and V_{CC} = 5V, we have measured the scattering parameter S_{12} under different levels of

the control voltage V_G. The network analyzer has been calibrated with the port extension function for de-embedding the $\lambda/4$ microstrip line used to solder the PIN diode.

In Fig. 3.7, we depict the S_{12} curves for five levels of control voltage V_G, the bias voltage V_{CC} was set to 3.3 V. When the circuit is turned off, V_G = 0, the PIN exhibits a relatively high isolation of about 10 dB. On the other hand, when V_G is increased to values greater than the threshold voltage (V_{th} = 1.5 V), the MOSFET's operation point moves to the saturation region, allowing the current to flow through the resistive network. For V_G greater than 3 V, the MOSFET is in the saturation region and the PIN diode is in fully forward bias, achieving an insertion loss of about 0.3 dB. The same experiment run at V_{CC} = 5 V yields very similar isolation and insertion loss under the same control voltages V_G.

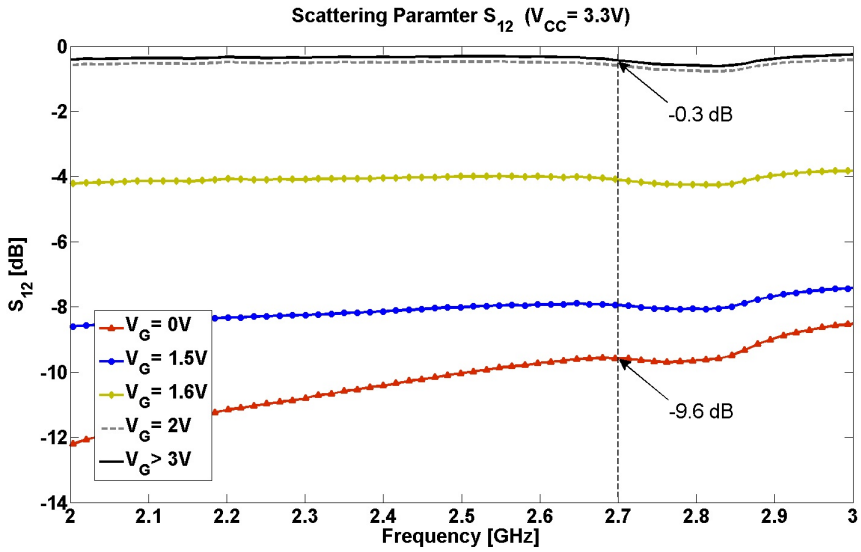

Figure 3.7 S_{12} measurements under different control voltage levels, at V_{CC} = 3.3 V

Once the PIN diode along with the switching circuitry were validated, we integrated the circuit design on a RALA tuned for WiFi and WiMAX channels, Fig. 3.8. Similarly for the previous version, the antenna design consists of four 90° microstrip elements arranged symmetrically between the top and bottom layer of a 1.6 mm thick FR-4 substrate. The

antenna is fed by a coaxial SMA connector, having the ground soldered to the larger bottom layer circle and the inner conductor soldered on the top smaller circle.

When all the microstrip elements are connected to the central port, a uniform surface current generates an omnidirectional radiation pattern around the azimuth plane. Alternatively, when two adjacent elements are connected to the central port, the beam is reflected toward the disconnected pairs, generating a directional pattern. Considering the four 90° spaced microstrip elements, the antenna can generate a total of four directional beams with 90° of spacing between each other. Lastly, a bi-directional beam can also be generated by activating a couple of opposite elements, keeping the other two disconnected. Thus, two additional bi-directional beams can also be generated. Each element has been designed with a square shape to maintain uniform current distribution when omnidirectional mode is activated, but also to enhance the front-to-back ratio when the element acts as a reflector for directional operations. In front of each pair of elements, we added a microstrip reflector on the top layer in order to enhance the directivity, and thus the gain, in directional mode.

Fig. 3.9 shows the circuit and the component arrangement to switch one pair of microstrip elements (the same circuitry is replicated next to each couple of elements). In order to reduce the number of wires, the DC voltage V_{CC} is provided through the RF cable by means of a bias-tee. Such voltage is then extracted from the input port by using 220 nH RF chokes (RFC) and a 15 pF decoupling capacitor (DC-block). The MOSFET, as well as the resistive network, were placed on the bottom layer and the resulting voltage V_{PIN} is shared between the two layers through a via hole. Resistor R_1 = 10 KΩ and R_2 = 230 Ω are set in order to provide a current of 20 mA for the two PIN diodes.

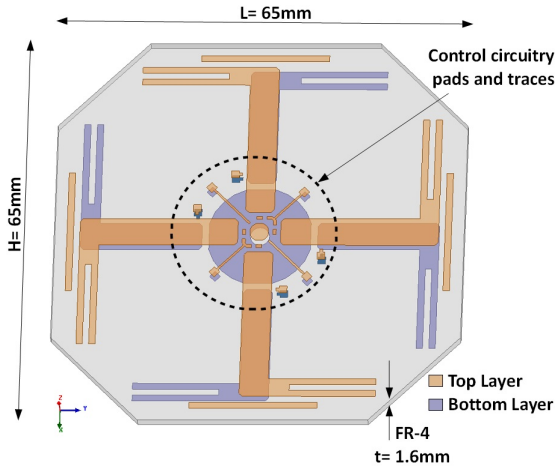

Figure 3.8 3D view and dimensions of the 2.4 GHz RALA.

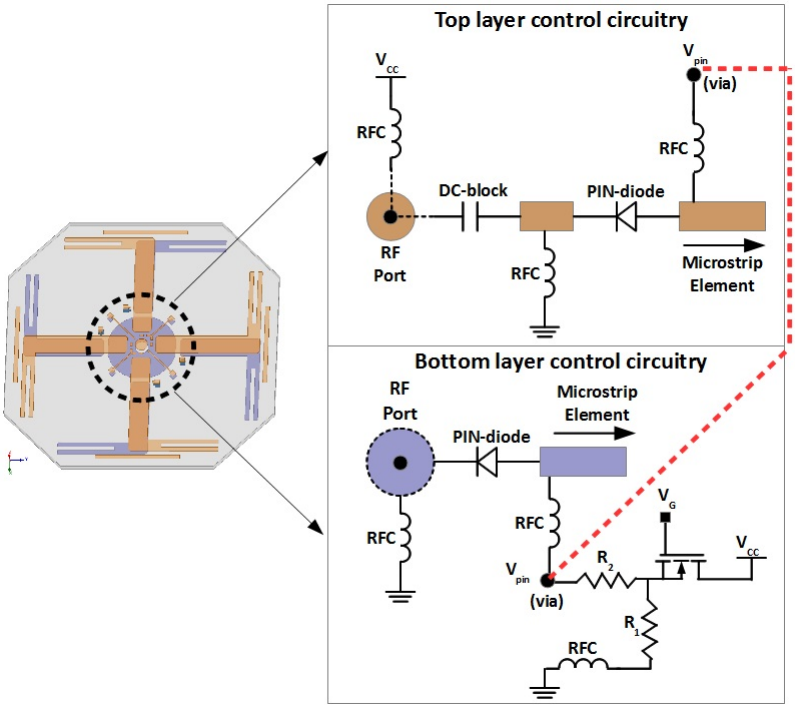

Figure 3.9 Schematic and arrangement of the switching circuitry components.

3.2.4 Numerical Simulations for WiFi and WiMAX Bands

The RALA with integrated switching circuitry has been designed and simulated using the High Frequency Structural Simulator HFSS™. A lumped element equivalent model of the

PIN diode has been extracted for the best fit with the S-Parameter measurements described in the previous section. The equivalent model and relative lumped element values under forward (ON state) and reverse bias (OFF state) conditions are depicted in Fig. 3.10. The elements L_S and R_S account for packaging and wire-bonding parasitic effects, while C_J and R_J are respectively, junction capacitance and junction resistance under 0 V DC bias.

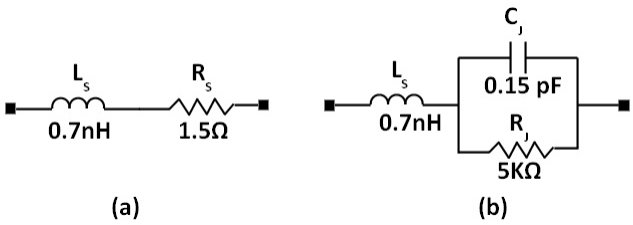

Figure 3.10 PIN diode equivalent model: (a) Forward bias, ON state. (b) Reverse bias, OFF state.

The PIN diode equivalent models were loaded into the HFSS antenna model by means of lumped RLC ports, connected between gaps having the same length of the actual SMD component. Accounting for such losses allows for more realistic simulations in terms of isolation and insertion loss of the PIN diode in ON and OFF states.

The input impedance characteristics of the proposed antenna were simulated from 1 GHz to 4 GHz assuming a matched 50 Ω feed port. The return loss, or S_{11}, is shown in Fig. 3.11 for each mode of operation: omnidirectional, directional and bi-directional beams. By looking at the 10 dB return loss bandwidth, the antenna covers a minimum bandwidth of 400 MHz in omnidirectional mode, covering WiFi and WiMAX channels from 2.4 to 2.8 GHz. When directional modes are activated, a larger bandwidth is achieved, extending the coverage up to 3 GHz.

Simulation analysis of radiation patterns were carried out for each antenna state. When

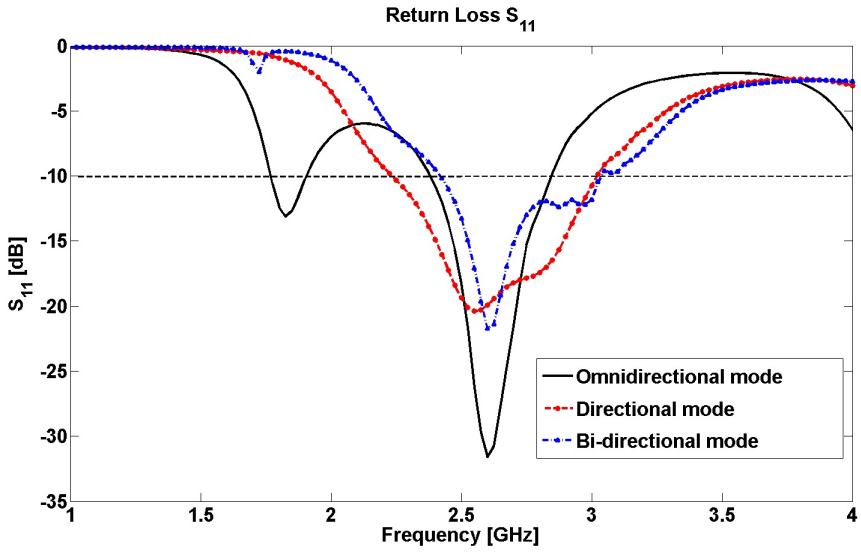

Figure 3.11 Return loss of the 2.4 GHz RALA for the three possible radiation modes.

all the microstrip elements are connected to the central RF port, the current distribution is uniform through the metallic elements, radiating an omnidirectional beam having 1.8 dBi of gain. The simulated radiation pattern is depicted in Fig. 3.12(a), showing the azimuth plane $\theta = 90°$ (solid line) and the elevation plane $\phi = 0°$ (dashed line).

Four distinct directional modes can be generated when two adjacent couples of elements are connected to the central port while the other three are disconnected, acting as reflectors. In Fig. 3.12(b) we show one such directional mode, having a gain of 3.6 dBi and a HPBW of 60°.

Two bi-directional beams can be radiated when two opposite elements are connected to the central port. The beam is reflected toward the disconnected pairs, radiating two main lobes in the direction of the excited pairs. Fig. 3.12(c) shows one of the two bi-directional modes with a gain of 4 dBi and HPBW of 50°.

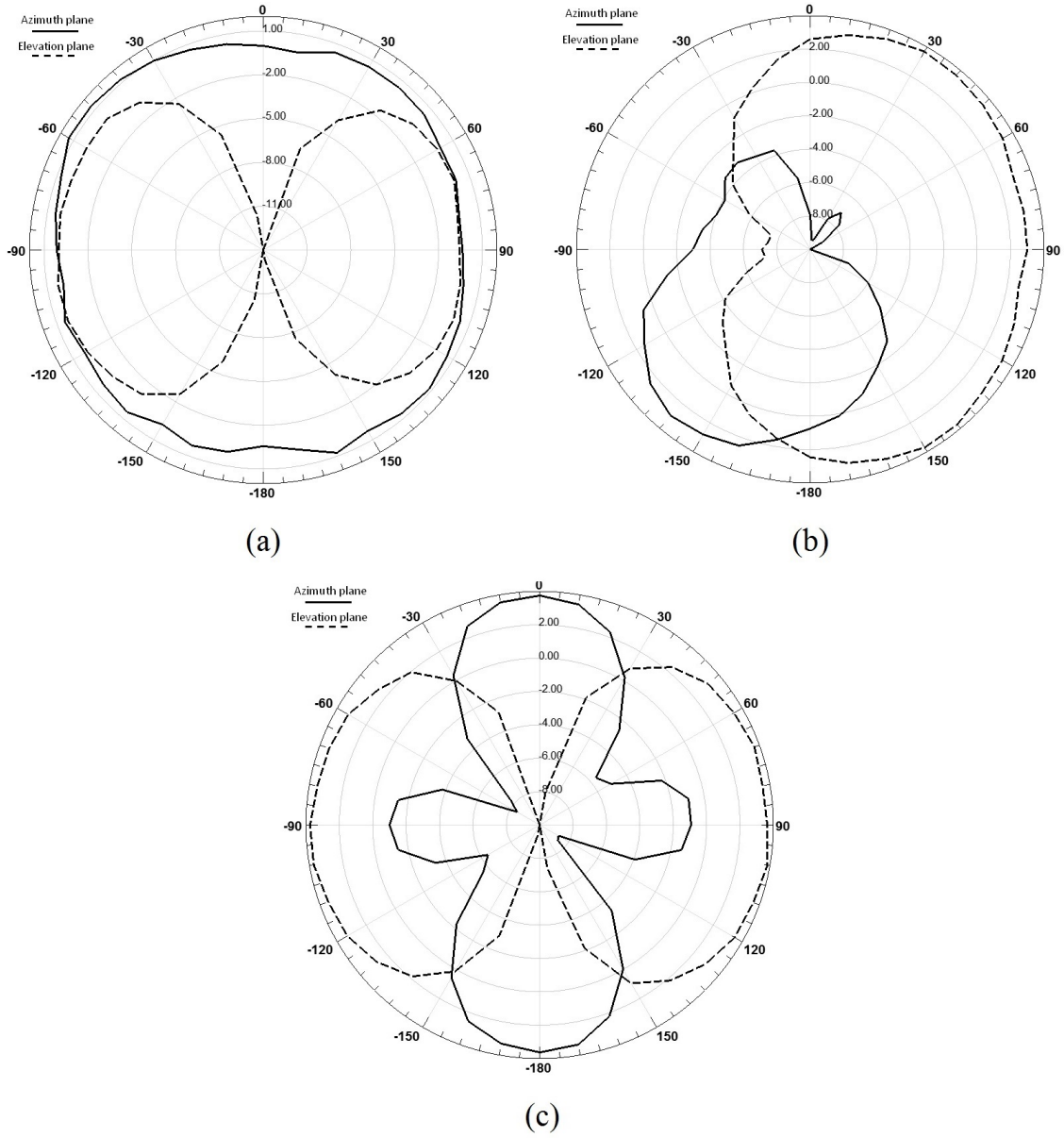

Figure 3.12 Simulated radiation patterns for (a) Omnidirectional mode, (b) Directional mode, (c) Bi-directional mode.

3.2.5 Experimental Analysis of Pattern Diversity for MIMO Applications

Radiation pattern diversity in wireless communications is recognized as a key parameter to improve spectrum efficiency and capacity [38]. Since the RALA has been designed for

application in multiple-input-multiple-output (MIMO) WLAN systems, in this section we assess the performance in terms of pattern diversity. We assume a realistic scenario where two of these antennas are employed as part of a 2x2 MIMO access point. Two antennas were aligned at a distance of $\lambda/4$ = 31 mm and connected to a vector network analyzer. The antenna diversity was computed from the following equation for the spatial correlation coefficient [66], expressed in terms of the S-parameters measured at 2.45 GHz:

$$\rho = \frac{\left|S_{11}^{*}S_{12} + S_{21}^{*}S_{22}\right|^{2}}{\left(1 - \left(\left|S_{11}\right|^{2} + \left|S_{21}\right|^{2}\right)\right)\left(1 - \left(\left|S_{22}\right|^{2} + \left|S_{12}\right|^{2}\right)\right)} \tag{3.3}$$

Since each antenna can generate 5 different radiation patterns, the total number of radiation pairs in a 2x2 array is 25, where half of the amount contains symmetrical permutations. For brevity, Table 3.1 shows the maximum spatial correlation for the three significant subsets of states, along with the respective maximum coupling between the two radiators.

Table 3.1 Maximum Spatial Correlation and Mutual Coupling Between Patterns Using Two RALAs.

Antennas state	ρ	Coupling
Omni-Omni	0.003	-22 dB
Max{Dir-Omni}	0.005	-18 dB
Max{Dir-Dir}	0.003	-16 dB

Overall, the measurements show low levels of patterns correlation, denoting a high spatial diversity. The 4G standard set ρ = 0.3 as the maximum correlation coefficient, while the maximum measured correlation is ρ = 0.005. In terms of mutual coupling between the two radiators, the maximum coupling is S_{21} = S_{12} = -16 dB when both antennas are in directional state. However, the majority of the remaining states exhibit couplings below

-30 dB. These coupling regimes indicate sufficient isolation between two antennas to be used as a two-element array in a MIMO system. Since the antenna has high potential to be used as part of a MIMO system [67, 68], concerns may arise in terms of the PIN diode's non-linearity. In order to address this consideration, in the next section we demonstrate that when two antennas of a similar type are employed in a 2x2 MIMO system, the influence of intermodulation distortions (IMD) are relatively low. The third-order IMDs are on the order of -100 dBm, approaching the typical OFDM noise floor of -110 dBm.

3.2.6 PIN Diode Non-linear Effects in MIMO Array

The presence of the PIN-diodes and the wide frequency bandwidth of the RALA motivated the need to analyze the intermodulation distortion that may appear in-band [69]. Devices such as diodes, transistors, and switches are nonlinear components and this nonlinearity characteristic is highly desirable for functions such as amplification and detection. However, the nonlinear effect of active devices can lead to undesired gain compression as well as generation of spurious frequency responses. At the transceiver side, these effects may lead to losses, signal distortion, and interference.

When using two reconfigurable antennas as part of a 2x2 MIMO system, it is desirable to evaluate the nonlinear effects that the switching components may generate. Let us consider a two-tone input voltage, consisting of two closely spaced tones, ω_1 and ω_2:

$$v_i = V_0 \left(\cos \omega_1 t + \cos \omega_2 t\right) \tag{3.4}$$

The total output output response of a nonlinear circuit can be modeled as a Taylor series in

terms of the two input voltages:

$$v_0 = a_0 + a_1 V_0 \left(\cos\omega_1 t + \cos\omega_2 t\right) + a_2 V_0^2 \left(\cos\omega_1 t + \cos\omega_2 t\right)^2 + \\ + a_3 V_0^3 \left(\cos\omega_1 t + \cos\omega_2 t\right)^3 + \ldots \tag{3.5}$$

In other words, the output spectrum consists of harmonics of the form $m\omega_1 + n\omega_2$, with $m, n = 0, \pm 1, \pm 2, \pm 3, \ldots$. These combinations of the two input frequencies are called *intermodulation products*. Specifically, the two third-order difference terms $2\omega_1 + \omega_2$ and $2\omega_2 - \omega_1$ produce frequency components located near the original input signals ω_1 and ω_2, and they cannot be easily filtered from bandpass filters. These components are the potential cause of distortion of the output signal, and this effect is called *third-order intermodulation distortion*.

For the 3.8 GHz UWB RALA described in Section 3.2.3, we calculated the antennas equivalent circuit model, and a simulation of a 2x2 MIMO system was performed in a circuit harmonic balance (HB) simulator (e.g., Agilent ADS). After considering different levels of mutual coupling between the two antennas, we simulated the intermodulation products as a function of the input power and operating frequencies.

A lumped circuit model of the radiating impedance of antenna has been considered to integrate with the PIN diode nonlinear circuit to perform the HB analysis. The antenna's equivalent model, in both omnidirectional and directional modes, was fitted to a resonant RLC circuit. Considering the center frequency of 3.8 GHz, the resistive component is provided by looking at the real part of the input impedance (Z_{in}), while the reactive L and C components were calculated using 3.6, where *X* is the imaginary part of Z_{in}. The values

of the lumped elements were tuned for the best fit with the measured S-Parameters. In Table 3.2, we summarize the RLC values relative to both antennas' modes. The Smith Charts in Fig. 3.13 show the models' response in terms of magnitude and phase, and their comparison with the measured antenna's S_{11}. The frequency sweep goes from 3 GHz to 4.5 GHz. The equivalent RLC models are in good agreement with the actual return loss of the antenna. Despite a slight discrepancy between the two representations, in both cases the operational bandwidth is centered at 3.8 GHz and the RL bandwidth coverage is guaranteed as well. The RLC model experiences a wider 10 dB RL bandwidth due to the intrinsic frequency dependence of the lumped elements.

$$\begin{cases} \sqrt{LC} = \frac{1}{\omega_0} \\ \frac{\delta X}{\delta \omega_0} \approx L \end{cases} \tag{3.6}$$

Table 3.2 RALA Equivalent RLC model values

Component	Omnidirectional Mode	Directional Mode
R	63 Ω	59 Ω
L	0.55 nH	0.7 nH
C	3.4 pF	2.5 pF

Next, we considered the employment of two of the designed reconfigurable antennas as part of a 2x2 MIMO system. The wide bandwidth of operation motivated the need to investigate the intermodulation distortions (IMD) that may appear when the two antennas operate at different center frequencies [70]. The non-linearity of the PIN diode components, used to switch between the elements, is responsible for generating third order intermodulation distortions within the bandwidth of operation. The PIN diode (Skyworks

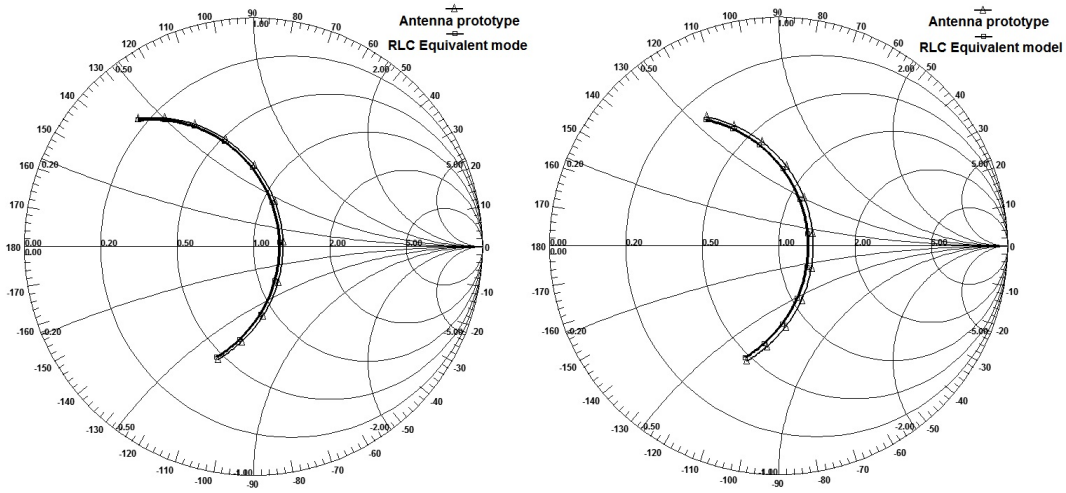

Figure 3.13 The best fitted equivalent model of return loss and comparison of RL with actual antennas measurements: (a) omnidirectional (b) directional.

SMP1345-079LF [62]) provides low series resistance (1.5 Ω) and low parasitic inductance (0.7 nH) up to 6 GHz. The required forward voltage is 0.89 V (I = 10 mA), while insertion loss and isolation simulated through the equivalent model [71] are 0.23 dB and 12.6 dB, respectively. On the antenna, the DC bias voltages were provided through 220 nH lumped inductors. Table 3.3 summarizes the equivalent model values which were used as intrinsic parameters for the two PIN diodes as part of the schematic depicted in Fig. 3.14.

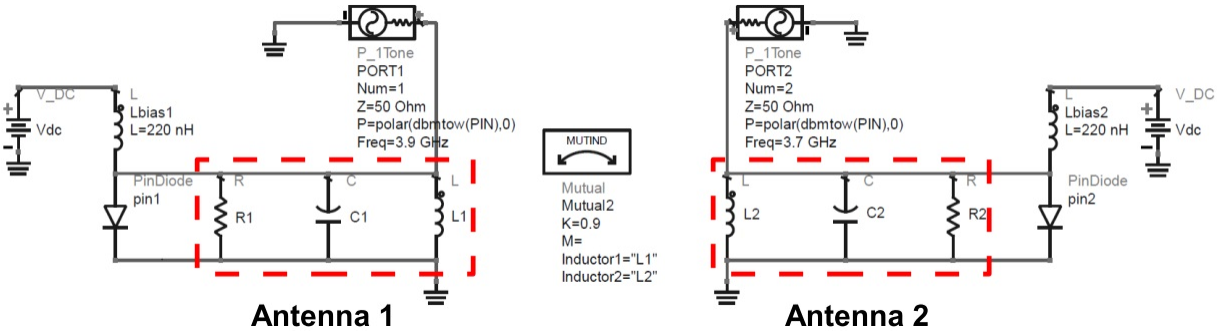

Figure 3.14 Circuit schematic of two antenna models equipped with pin-diodes, emulating coupling in 2x2 MIMO antenna system

Fig. 3.14 renders the schematic diagram used for HB simulation in Agilent ADS. It contains two antenna equivalent RLC models, each of them equipped with SMP1345 PIN diodes (having loaded intrinsic values) with the appropriate bias circuitry (L = 220 nH and DC power). Both antennas are fed by a generator that provides both 3.9 GHz and 3.7 GHz carrier frequencies, respectively. When multiple antennas are being used as part of a wireless MIMO system, it is important to be aware of the mutual coupling that may occur between them. Considering this MIMO situation, the coupling S_{21} has been simulated using the software HFSS for two different configurations: first, two antennas were broadside coupled by placing one on top of the other, then, they were horizontally coupled on the same plane. When the antennas are spaced 0.5λ, the simulation in omnidirectional mode yields a coupling of around -15 dB. Similarly, when directional beams are used, the worst case for which two beams are pointing toward each other shows about -11 dB of coupling. To resemble this scenario as close as possible, the 2x2 equivalent circuit for harmonic balance simulations takes into account antenna coupling by varying the mutual induction between L1 and L2. Despite the coupling cannot be considered as exact as in a real scenario, this method gives us the chance to evaluate the harmonic distortions starting from worst case values of insertion loss (IL). This IMD analysis would otherwise not have been possible using the method of moment software (HFSS).

Harmonic balance simulations have been carried out for an input power sweep from -20 dBm to +20 dBm in steps of 0.5 dBm. We considered the PIN diode in forward bias condition, as it can connect the elements to the center feed for omnidirectional or directional pattern generation. Therefore, each antenna in Fig. 3.14 is equipped with a PIN diode containing the intrinsic parameters summarized in Table 3.3. The results of the simulations

will show the intermodulation products that are being generated across Antenna 2 up to 10 GHz. The broadband frequency sweep helps evaluate higher intermodulation products even outside the bandwidth of operation. A level of -110 dBm was considered as OFDM noise floor. We considered operation of the antenna at the largest 6 dB RL bandwidth (600 MHz in omnidirectional mode and 900 MHz in directional mode). Thus, besides the fundamental signals at OFDM frequencies of f_1 = 3.7 GHz and f_2 = 3.9 GHz, we are interested in investigating the third order components $2f_1$-f_2 = 3.5 GHz and $2f_2$-f_1 = 4.1 GHz as in-band distortion signals.

Table 3.3 PIN Diode Intrinsic Values

Parasitic inductance	L_S = 0.7 nH
Series resistance	R_S = 1.5 Ω
Capacitance	C_T = 0.15 pF

By considering that in a wireless MIMO system each antenna configuration is independently selected for the best link performance, in the harmonic balance simulations we accounted for all the three possible cases: both antennas transmitting in omnidirectional mode, both antennas transmitting in directional mode, and, one antenna in omnidirectional mode while the other generates a directional beam. For each case, we considered two worst cases with high mutual coupling, k = 0.9 and k = 0.5, then a better situation where the coupling is improved to k = 0.1. In this way, we can summarize the HB analysis within three coupling ranges, accounting for all the possible beam configurations that two antennas may assume when used in a MIMO system. For the first case, where both antennas transmit omnidirectional beams, Fig. 3.15 shows sample results of the intermodulation products that are being generated. In the low mutual coupling case, the antenna's bandwidth is free from

distortions since the in-band 3rd order components approach the noise floor. On the other hand, when higher mutual coupling occurs, the in-band distortions start to appear for input power levels above 15 dBm. However, their values are still very low, about -97 dBm for very high mutual coupling. In all cases, other higher order components are being generated within the simulated frequency sweep, but they do not reside into the antenna's bandwidth. The other two cases, where omnidirectional plus directional and directional plus directional modes are used, the results are in the same order of magnitude as in Fig. 3.15. To summarize all the IMD products more clearly, Table 3.4 lists the values for all the three configuration cases.

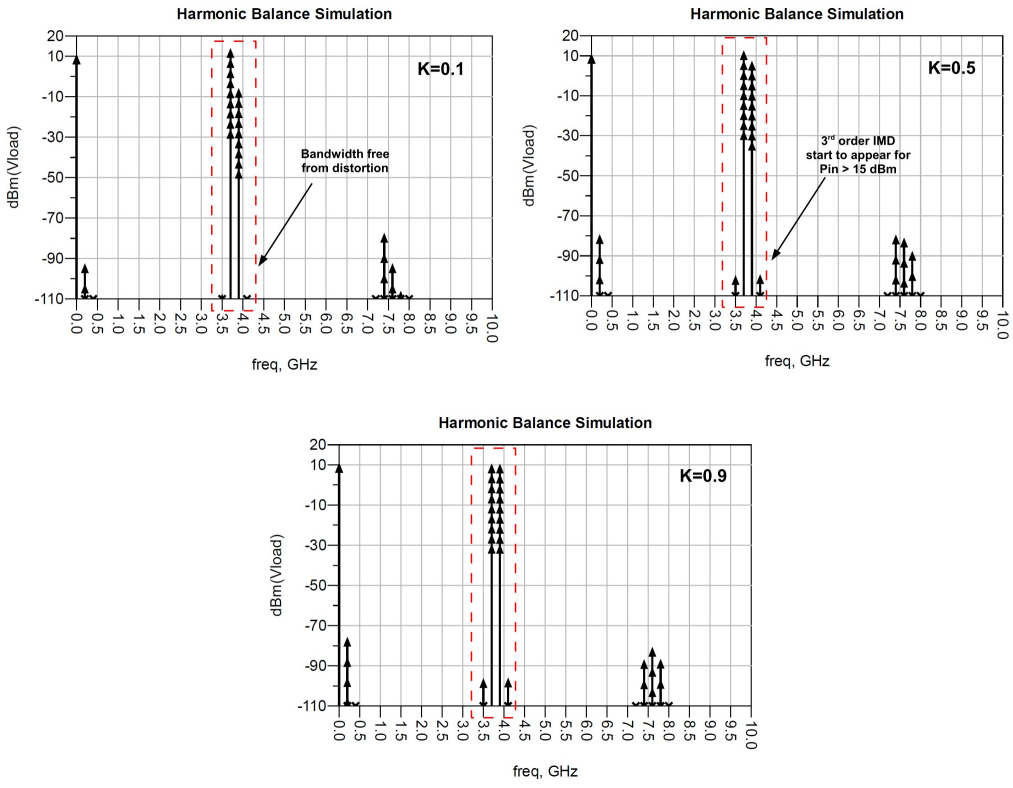

Figure 3.15 HB simulation, both antennas in omnidirectional mode: (a) low coupling, k = 0.1 (b) higher coupling k = 0.5 (c) very high coupling k = 0.9.

In summary, we have observed that by increasing the mutual coupling between the

Table 3.4 Intermodulation Distortion Simulations

	Coupling	3.5 GHz		4.1 GHz	
		dBm	dBc	dBm	dBc
	k = 0.1	-108.4	-128.4	-124.6	-144.6
	k = 0.5	-100.6	-120.6	-100.1	-120.1
	k = 0.9	-97.1	-117.1	-96.8	-116.8
[a]	k = 0.1	-110.0	-130.0	-126.9	-146.9
	k = 0.5	-100.6	-120.6	-101.7	-121.7
	k = 0.9	-96.9	-116.9	-97.5	-117.5
	k = 0.1	-111.3	-131.3	-130.0	-150.0
	k = 0.5	-101.6	-121.6	-103.6	-123.6
	k = 0.9	-98.9	-118.9	-98.2	-118.2

[a] Each subset of rows is relative to the three respective 2x2 array case: omnidirectional-omnidirectional, omnidirectional-directional, directional-directional.

antennas, the intermodulation distortion becomes more pronounced. For a low value of mutual coupling k = 0.1 (IL of 20 dB), the in-band third order harmonics start to appear for input power levels above 15 dBm. On the other hand, for a higher value of mutual coupling, k = 0.5 and k = 0.9, the third order products rise at lower input power levels of 10 to 15 dBm. However, in all cases the power difference between IMD levels and input power (dBc column in Table 3.4) is quite high, thus the quality of signal in a real scenario would not be affected. In fact, by considering the theoretical expression *kTB* for a bandwidth of 600 MHz, the noise floor would be about -86 dBm, which is always above the simulated in-band intermodulation products for coupling insertion loss values of 6 dB to 20 dB.

3.3 Optically-controlled Reconfigurable Alford Loop Antenna

Optically controlled reconfigurable antennas are a class of radiating elements that are able to change their radiation properties through optical activation of silicon switches or reactive

elements. With respect to the conventional DC control of lumped components, the use of optically controlled devices is preferable because they eliminate the need for metallic wires that may interfere with the antenna's radiation characteristics [49]. Additionally, while the switching speed of DC-controlled lumped elements is typically limited by external control circuitry, the use of photonic components is significantly faster. Other important aspects, such as the thermal and electrical isolation from the control circuitry, make the photonic switching technique a very attractive solution relative to conventional DC control of lumped elements.

In general, the DC control of reconfigurable antennas often requires additional metallic microstrip or wired biasing lines, which add more complexity and may interfere with the desired radiation pattern. In order to overcome this issue, several optically controlled reconfigurable antennas have been reported in the literature. In [72, 73], the authors propose a frequency-reconfigurable antenna designed using photoconductive switches. The laser light is coupled through an optical fiber that passes through the substrate by means of a proper fixture to illuminate the switches connected to the top layer metallic elements. A reconfigurable monopole antenna, presented in [74], employs photoconductive switches illuminated in free space to switch between metallic branches and thus change resonant frequency. In [75] the authors propose an optically reconfigurable dipole antenna which can vary frequency and radiation pattern by switching between short and long configurations of the conductive arms. However, in all of these designs, the authors use customized photoconductive switches that are not commercially available.

In the next section, we experimentally apply an optical switching control technique to the RALA for the 2.4 GHz WiFi band [39, 48]. Switching control of RF PIN diodes is

accomplished through the optical illumination of a phototransistor, equipped with a proper biasing network. The application of an optical switching technique is advantageous for those base-station applications (WLAN) where the need of eliminating cumbersome and interfering cables is more important than a slight increase in power consumption for driving the low cost VCSEL laser. In this section, we show a new optical switching strategy applied to the RALA that can effectively reduce the far-field interference occurring under conventional wired DC control, which may cause distortion of the desired radiation patterns.

3.3.1 Phototransistor as Optical Control of RF PIN Diodes

This optical technique for reconfigurable antennas combines the benefit of using an electrical PIN diode, specifically designed for RF switching, and a phototransistor for the optical control. For a PIN diode we selected the Skyworks SMP1345 [62]. This 1.2 x 0.8 mm SMD package device has very low capacitance and is designed for high isolation and low insertion loss in wireless applications. As optical control, a silicon-based Everlight PT19-21B phototransistor was employed with a 20 mA collector current, which is sufficient for driving up to two PIN diodes in two forward biases. In this two-terminal phototransistor, the maximum collector-emitter voltage V_{CE} is 30V and saturation voltage $V_{CE(sat)}$ is 0.4 V. This model has been preferred thanks to its small 1.2 x 0.8 mm SMD package as well as fast response time and high photosensitivity. Generally speaking, the phototransistor is in essence a bipolar transistor having a transparent package so that light can reach the base-collector junction. The electrons generated by the incoming light are amplified by the transistor's current gain β, allowing for current to flow from the two poles of the de-

vice. The main characteristics of the selected phototransistor, reported in the component's datasheet [76], are summarized in Table 3.5.

Table 3.5 PT19-21B Phototransistor Characteristics

Collector current	I_C = 20 mA
Wavelength of peak sensitivity	940 nm
Responsivity	0.9 A/W
Collector dark current	100 nA

3.3.2 Experimental Results

A picture of the PIN diode mounted on microstrip lines for S-parameter measurements is shown in Fig. 3.16, along with the depiction of the schematic of the control circuitry. When the phototransistor is not illuminated, the voltage across the PIN diode (V_{PIN}) is equal to zero and thus the PIN diode is in a high isolation state (OFF). On the other hand, under optical illumination, a photocurrent flows between the collector and emitter poles of the phototransistor. A resistive network (R_E = 10 kΩ, R_P = 470 Ω) provides a proper voltage drop that is required for changing the bias condition of the RF PIN diode, hence enabling a required insertion reduction for switching from OFF to ON states of the RF PIN diode (V_{PIN} = 1 V, I = 10 mA).

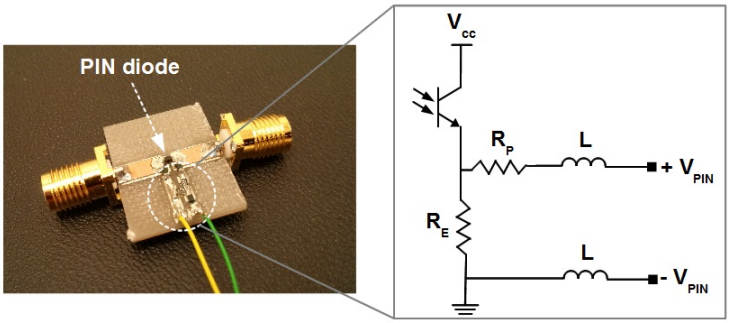

Figure 3.16 PIN diode mounted on microstrip lines for S-parameter measurements and detail of the optical control circuitry.

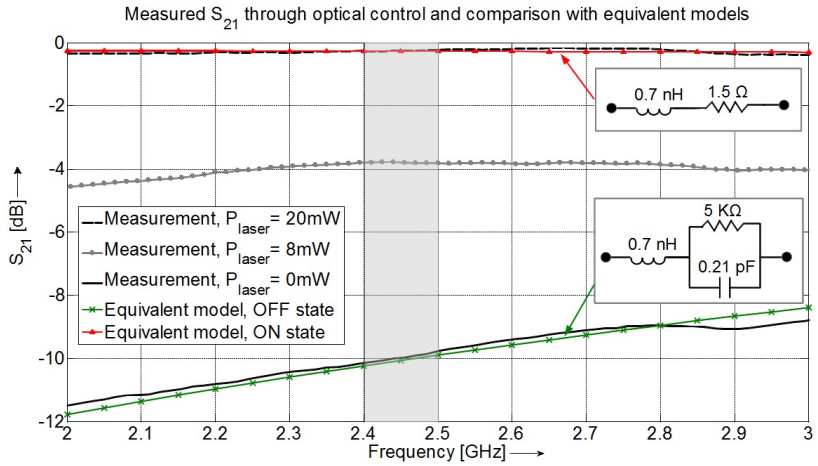

Figure 3.17 S_{21} measurements of the PIN diode under different levels of λ = 850 nm laser illumination on the phototransistor. Lumped equivalent models of ON and OFF states are also shown.

S-parameter measurements were carried out to analyze the PIN diode performance under different laser levels incident to the phototransistor. As a light source, we used a free space 850 nm laser (Vixar VCSEL), which corresponds to a responsivity of 0.9 A/W of the phototransistor. Similarly to the previous measurements, calibration of the vector network analyzer was made by de-embedding $\lambda/4$ microstrip lines used to solder the PIN diode. The measured S_{21} performance of this RF PIN diode is depicted in Fig. 3.17 under three different VCSEL optical powers. Under dark conditions, the isolation at 2.45 GHz is about 10 dB, whereas when the light incident to the phototransitor exceeds 8 mW, the generated photocurrent switches the PIN diode to conduction mode. However, the best value of insertion loss, S_{21} = -0.3 dB at 2.45 GHz, is achieved when the VCSEL is biased for free-space optical power of 20 mW. Note the level of light coupling to photo-transistor through its optical window is significantly less, as an optical focusing mechanism is now being used in this topology. Through the use of a 2D micropositioner for *x*-*y* tilting and an adjustable

base for z axis, the laser source was aligned to the phototransistor's flat-top photosensitive area, achieving a light coupling sufficient to create a biasing current flowing of 10 mA.

The presence of lumped switching elements in reconfigurable antennas often requires additional control boards to boost the current from the General Purpose Input/Output (GPIO) pins of the wireless radio platform. For comparison, a traditional MOSFET based topology would exploit the same circuit topology as in Fig. 3.16. However, the use of a 1 mm2 2-terminal phototransistor instead of a conventional SOT-23 3.7 mm^2 3-terminal MOSFET allows us to unobtrusively integrate the switching circuit in close proximity to the non-radiating area of the proposed antenna, eliminating the DC wires for gates control. We specifically selected small package SMD components, which occupy a total area of about 4 mm^2, maintaining full substrate robustness. Despite the fact that this technique involves the use of multiple components, the occupied area is relatively small, resulting in a good, cost-effective solution.

Beyond the aforementioned promising performance, in terms of isolation and insertion loss, this technique is also less affected by the noise in the laser source as the RF impedance of the switching element is not directly related to the generated photocurrent. In other words, since we take advantage of the ON/OFF behavior of a phototransistor, small variations of light intensity around its high responsivity region do not lead to significant change in the relative RF insertion loss. In fact, at the responsivity region of 0.9 A/W, small variations in the order of 15-20 $\%$ of the optical power lead to very limited changes in the forward current that flows through the PIN diode. As a result, the PIN diode series resistance does not change significantly and the insertion loss has been observed to sweep between $0.4 \leq S_{21} \leq 0.2$ dB.

The good performance demonstrated by this technique allowed us to apply the optical switching circuitry to the RALA. The next section describes the implemented antenna design along with the integrated optical control layout. The whole radiating system is then validated with comprehensive input impedance and radiation pattern measurements.

3.3.3 Antenna Design With Integrated Optical Circuitry

The design is built on the 2.4 GHz RALA design previously described and the control circuitry has been re-designed to include the optical control. As shown in Fig. 3.18 pads and gaps on the top and bottom layer are designed to include the RF PIN diodes along with the optical control circuitry described in the previous section and depicted in Fig. 3.16. Also in this case, we have used a standard FR-4 substrate and the antenna's detailed dimensions are listed in Table 3.6.

Table 3.6 Optical Reconfigurable Alford Loop Antenna Dimensions

D = 90 mm	Antenna diameter
R_b = 18.2 mm	Bottom circle diameter
W_b = 4.9 mm	Branch width
L_b = 29.5 mm	Branch length
W_w = 3.3 mm	Wing width
L_w = 26.5 mm	Wing length
W_p = 2.2 mm	Parasitic width
L_p = 24.2 mm	Parasitic length
L_s = 14.9 mm	Slot length
W_s = 1.1 mm	Slot width

To maintain purely optical control, the necessary bias voltage for the driving circuitry is provided by means of a bias-tee connected to the RF input port. As depicted in Fig. 3.19(a), the positive bias is extracted on the top layer from the RF inner conductor using a L = 220 nH RF-choke inductor and decoupled from the ground through a C = 15 pF

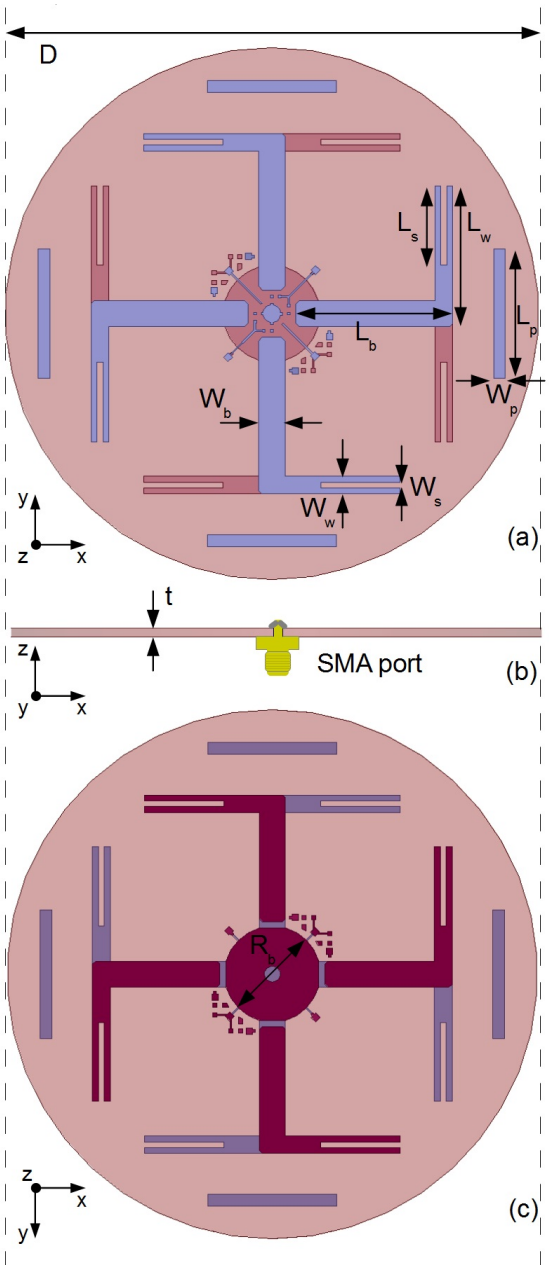

Figure 3.18 3D model of the proposed reconfigurable planar antenna. (a) Top layer view. (b) Horizontal profile with RF input port detail. (c) Bottom layer view. The small pads and lines visible on both layers constitute the arrangement for the SMD components population.

DC-block capacitor. On the bottom layer, shown in Fig. 3.19(b), the phototransistor, along with the resistive network R_1 = 10 KΩ and R_2 = 200 Ω, create the necessary bias condition VPIN to switch ON and OFF the PIN diodes on the top and bottom layers.

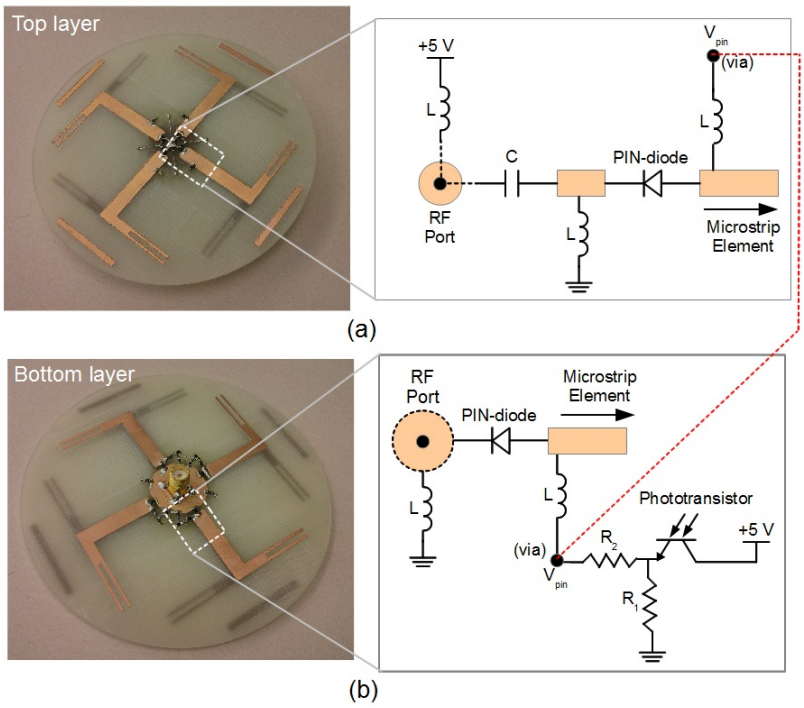

Figure 3.19 Manufactured prototype and details of the optical switching circuitry for a pair of symmetric elements. (a) Top layer biasing circuitry. (b) Bottom layer optical and biasing circuitry. The voltage and current activated by the phototransistor, are shared between the two layers through a via hole (red dashed line).

The antenna layout was designed and tuned using the full-wave electromagnetic simulator Ansoft HFSS [63]. In order to perform more realistic simulations, lumped equivalent models of the PIN diode [62] have been extracted for the best fit with the measurements depicted in Fig. 3.17. The models were then loaded into the HFSS antenna design in the form of RLC lumped ports.

Once the antenna was properly tuned for the desired impedance matching and radiation patterns, a first prototype was manufactured through a milling machine process. The board was then populated with the SMD components, constituting the optical switching circuitry as shown in Fig. 3.19.

Input Impedance Experimental Results

The return loss is defined as the ratio between the power reflected back from the antenna port and the power delivered. It is determined by the scattering parameter S_{11}, which describes the impedance matching between a 50 Ω line and the antenna port. In our case, the antenna design was tuned to exhibit good impedance matching within the WiFi band from 2.41 to 2.48 GHz in all the configurations. Good impedance matching is assumed when $S_{11} \leq$ -10 dB, as it means that more than 90 % of the input RF energy is actually fed to the antenna.

The measurements were conducted by first calibrating an Agilent N5230A vector network analyzer. Next, the optical power was equally split to illuminate all the four phototransistors, provided by the same VCSEL 850 nm laser used for the measurements described in the previous section. The power was split by means of a 1x4 fiber optic coupler with 3 dB insertion loss and plastic housing of precise alignment at the fiber optics terminations. The VCSEL laser source was tuned for equal 20 mW in each output and the correct PIN diode insertion loss verified through the S-parameter fixture of Fig. 3.16.

For performance comparison, we manufactured an electrically controlled version of the same antenna. Four copper wires were soldered on the RF-chokes for driving the PIN diodes through external DC power supply. By looking at the return loss of both omnidirectional and directional states, depicted in Fig. 3.20(a) and (b) respectively, it can be seen that the S_{11} resonance peaks are in good agreement between measurements and simulations. In Table 3.7, we summarize the simulated 10 dB bandwidth for each state, along with comparison between electrical and optical controls. It can be noted that the measured bandwidths

under optical control are slightly less than the simulations and DC control, although still maintaining good impedance matching from 2.45 to 2.48 GHz.

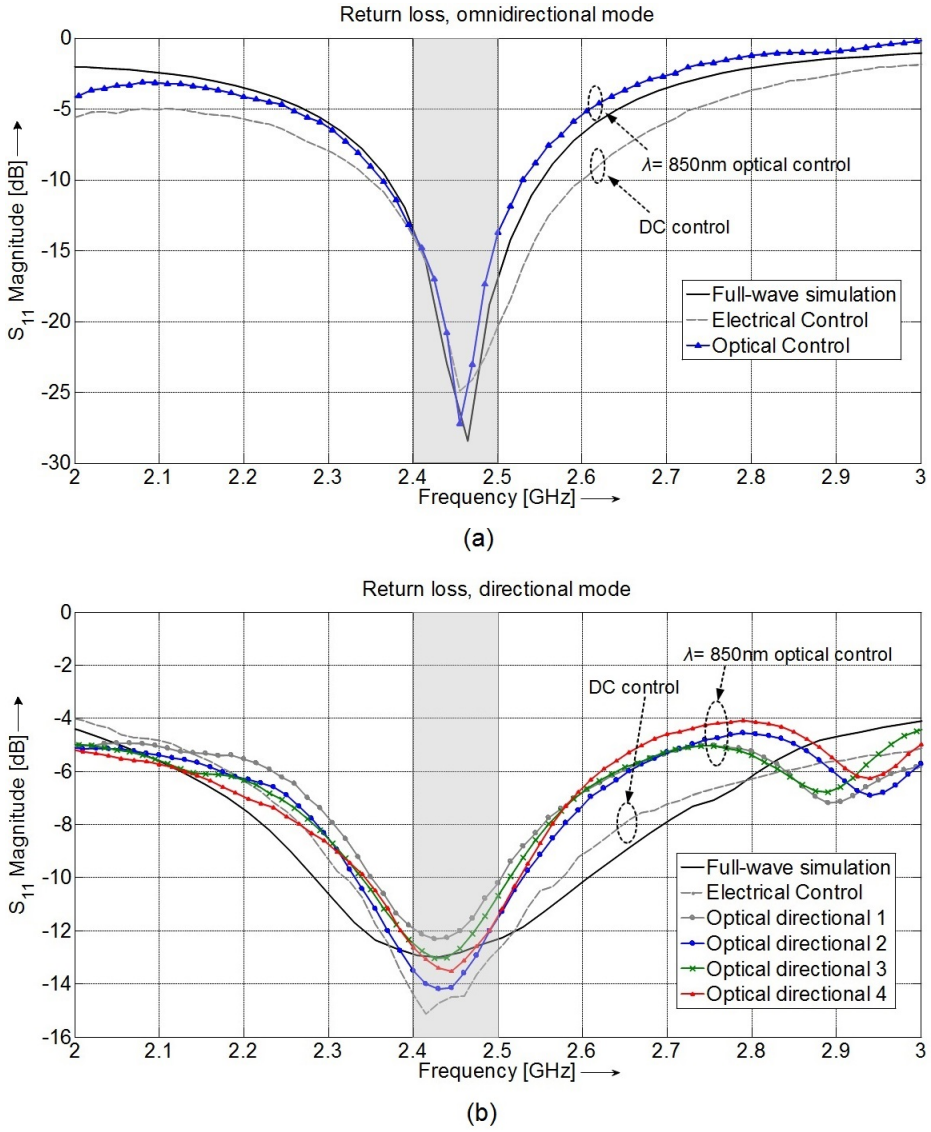

Figure 3.20 Simulated return loss for each antenna state and comparison of measurements between electrical and optical control. (a) Omnidirectional mode (b) Directional mode. While the simulated S_{11} is always identical for each directional state, some slight differences occur in real scenario when the four directional modes are measured under light illumination.

While moderate shifts in frequency and absolute peak amplitudes are commonly due to manufacturing tolerances and manual population of the board, the smaller bandwidth

Table 3.7 Bandwidth Comparison Between Optical Control, Electrical Control and Simulation

Control Omnidirectional	BW	Δ BW	Directional BW	Δ BW
Optical	160 MHz	-	200 MHz [a]	-
Electrical	250 MHz	90 MHz	250 MHz	50 MHz
Simulation	150 MHz	10 MHz	330 MHz	130 MHz

[a] Average of the four curves

exhibited by the optical control is potentially due to the reactive lumped elements as part of the control circuitry. Nonetheless, even with this bandwidth reduction, the manufactured antenna covers the entire 2.4 GHz band with good impedance matching in all the configurations under optical control.

Radiation Pattern Experimental Results

The radiation patterns characterize the variation of the far-field radiation magnitude as a function of angular steps at a specific frequency. In order to evaluate the radiation characteristics of the proposed antenna, we have measured the radiation patterns in the case of the single omnidirectional mode and for all of the four directional beams. For this purpose, instead of using a conventional anechoic chamber, we have used the tool EMSCAN RFxpert [77] which is highly convenient when measuring optically-controlled antennas. This tool is a bench-top measurement system that enables us to get 3D and 2D antenna pattern measurements in real time, avoiding the need of cumbersome arrangements of cables and fiber optics around the turntable of an anechoic chamber. Fig 3.21(a) and (b) show measurements of the omnidirectional and directional mode. Each figure shows azimuth (*x*-*y*) and elevation (*x*-*z*) cuts of the pattern according to the antenna coordinate system given in the

insets. When all of the four phototransistors are illuminated, the four microstrip element pairs are connected to the central feed port and the excited uniform current distribution generates an omnidirectional mode illustrated in Fig. 3.21(a). The results show a peak gain of about 2 dBi and uniform omnidirectional shape around the azimuth plane.

On the other hand, when just a single phototransistor is illuminated, the single pair of elements that is connected to the feed port generates a directional beam directed broadside to the active elements. As shown in Fig. 3.21(b), the resulting beam exhibits peak gain of 3.6 dBi and a front-to-back ratio of about 8 dB. The HPBW is approximately 65°. In Fig. 3.21(c) we show the azimuth view of all four directional beams, where it is important to recall that only one beam at time can be activated.

To further assess the radiation performance of the optical control, an electrically controlled version of the same antenna was also measured and compared. Fig. 3.22 shows the measured radiation patterns of both omnidirectional and directional states. The two plots show the azimuth cut, as it represents the actual beam steering plane, which also showed a more significant variation between the two control strategies. For the case of the omnidirectional state depicted in Fig. 3.22(a), we can note that the curve relative to the electrical control is less uniform than the optical control. Specifically, around the regions where the four metallic wires were connected, the radiation pattern exhibits a gain reduction between 2 dB $\leq \Delta$ G $\leq$ 3 dB. Despite the envelope resemblance to an omnidirectional beam, the presence of wires interfere with the radiated field causing local magnitude reductions in the order of 40-50 $\%$. For the second case relative to directional state in Fig. 3.22(b), the peaks of broadside magnitude between the two curves are quite similar. The presence of wires enlarges the back lobes, reducing the front-to-back ratio. Even by looking at other

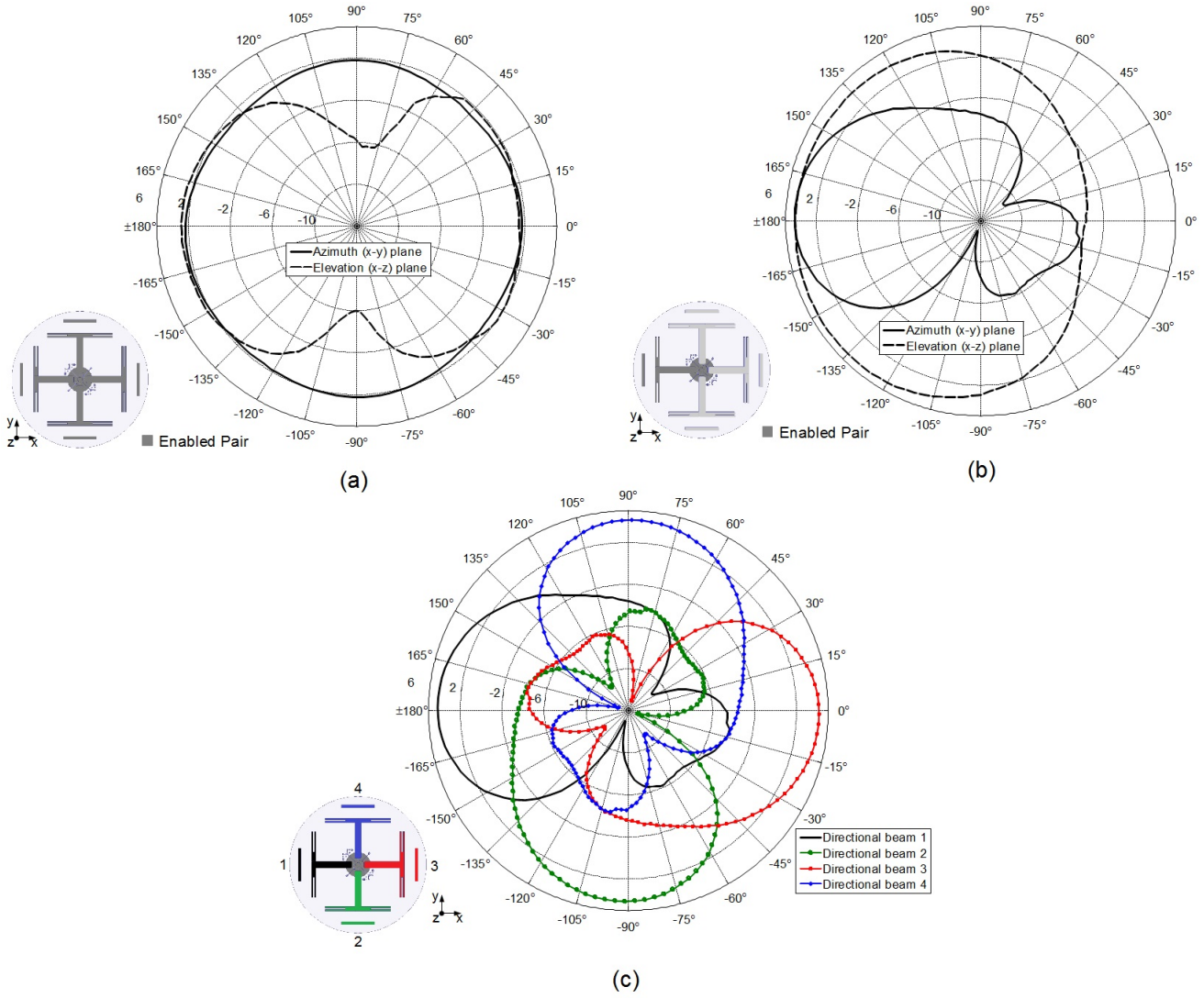

Figure 3.21 Measured radiation patterns, at 2.45 GHz. (a) Omnidirectional beam, azimuth and elevation view. All the microstrip elements are connected to the central port. (b) Single directional beam, azimuth and elevation view. In this example, only the pair of elements along negative x axis is activated. (c) Azimuth view summary of the four possible directional beams. Note that each beam is activated singularly.

existing solutions, we can see that the presence of metallic wires is a factor that reduces the homogeneity of omnidirectional radiation patterns [78, 79]. This challenge is amplified especially when the DC wires are soldered in locations corresponding to higher radiation intensity. Moreover, it is important to highlight how the proposed antenna topology enables

a fully optical control of the PIN diodes. In fact, the layout allows for extraction of the DC current from the coaxial RF port, eliminating not only the switching control wires, but also the DC feed lines. This key feature allows for a fully optical control, which could not be realized with concurrent planar antennas that achieve similar patterns reconfigurability [5].

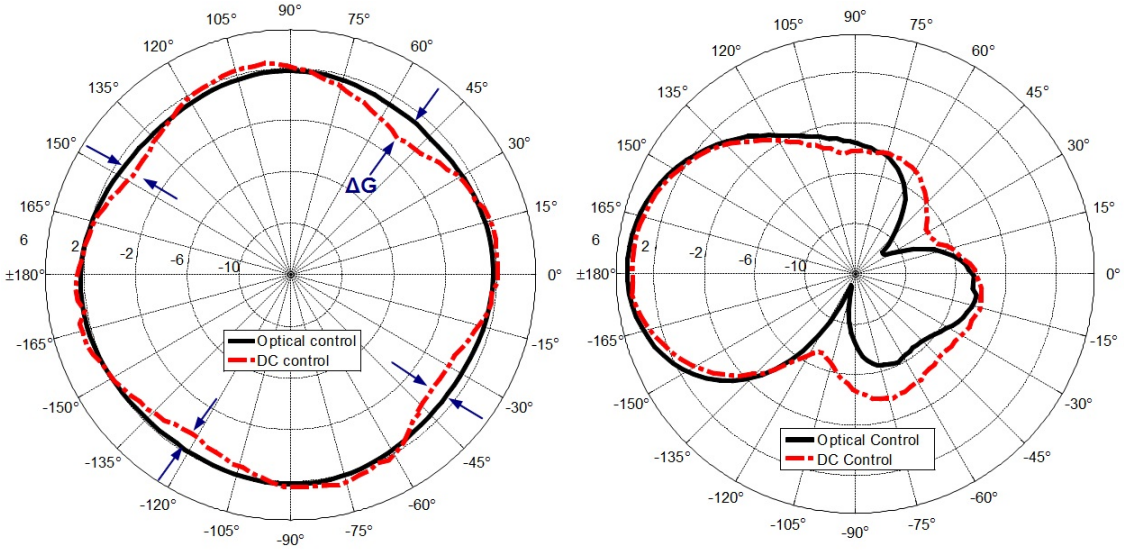

Figure 3.22 Comparison of radiation patterns between optical and electrical control of the proposed reconfigurable antenna. (a) Omnidirectional state. (b) Directional state. Measurements conducted at 2.45 GHz.

3.4 Multi-band Reconfigurable Alford Loop Antenna

The increasing number of wireless users and the Internet of Things (IoT) has boosted the adoption of WiFi connectivity to access the Internet. However, the widespread usage of the 2.4 GHz band for WiFi communication has congested these channels due to numerous interfering devices. The much less congested 5 GHz band has been increasingly utilized for more advanced applications (e.g., video streaming and gaming), where packet loss and delays are critical issues. Simultaneous and selectable dual-band routers are commercially available. These devices have different characteristics, but simultaneous 2.4 - 5 GHz routers

seem to be the preferred solution for enhanced performance [80]. However, the presence of two distinct bands has often required the installation of two separate antennas, which increases the costs because of the additional coaxial cables and RF connectors. In addition, the number of antennas is further increased if the device includes MIMO (Multiple-Input Multiple-Output) technology. In the following sections, we discuss two approaches for designing a RALA architecture that covers 2.4 and 5 GHz channels [81]. The first approach uses lumped inductors and capacitors for designing dual-band elements, while in the second approach two independent sets of elements are combined together using lumped diplexers. Other multiband RALA architectures may be designed using RF switches [82], but we focus our effort on the use of lumped filters thanks to their lower losses and absence of active DC biasing.

3.4.1 Multi-band Elements Approach

For the first approach, we started from the RALA design for the 2.4 GHz band previously described and we scaled the design to resonate at 5 GHz. Using HFSS, two different simulations were performed for tuning the smaller 5 GHz elements and the larger 2.4 GHz elements. Next, the two designs were merged together through a parametric simulation that included ideal L and C for separating the two bands, shown in Fig. 3.23. While the inductor acts as low-pass filter for the 2.4 GHz spectrum, the capacitor C acts as a high-pass filter for the 5 GHz spectrum. Due to the unknown impedance at the intersection of the two paths, we conducted a series of simulations and experiments to find the best L-C configuration to accomplish proper impedance matching within the two bands. As a result, the best configuration was found to be L = 0.4 nH and C = 1.2 pF. The physical dimensions

in Fig. 3.23(b) are: l_1 = 37 mm, l_2 = 21 mm, l_3 = 5.5 mm, and l_4 = 6.1 mm. The two slots' lengths are g_1 = 14 mm and g_2 = 3.5 mm.

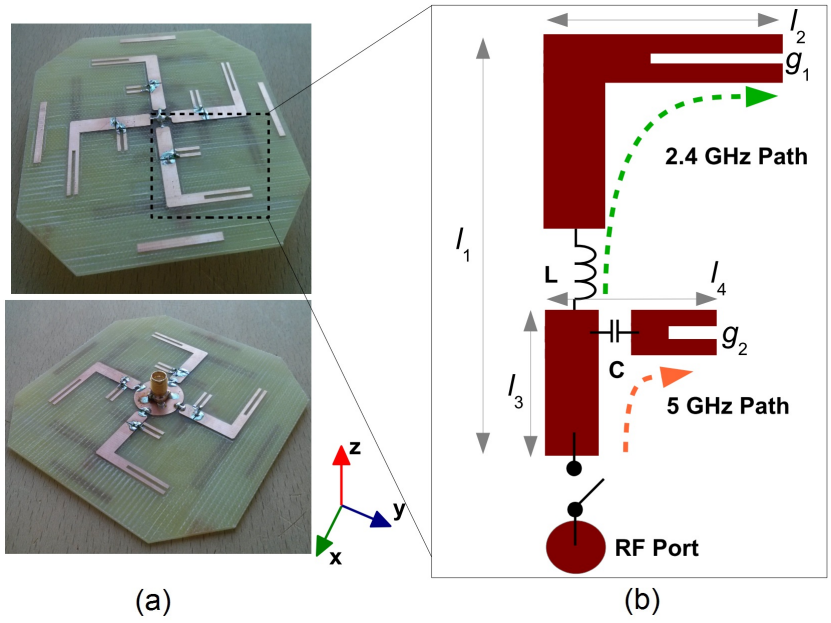

Figure 3.23 (a) Top and bottom layer pictures of the fabricated multi-band RALA. The total dimensions are 9 x 9 cm. (b) Illustration of a single element, with lumped inductor L and capacitor C for separating the two current flows at 2.4 and 5 GHz.

3.4.2 Input Impedance Experimental Results

The manufactured prototype was measured through an Agilent N5230A Vector Network Analyzer for validating the simulation results. Fig. 3.24 shows the return loss for the two cases of omnidirectional mode (all elements connected) and directional mode (two adjacent elements connected). By looking at the -10 dB return loss threshold, we notice that both configurations cover the entire lower ISM band, from 2.41 to 2.48 GHz. On the other hand, the two configurations share a shorter bandwidth at 5 GHz, from 5.2 to 5.3 GHz (channels 40 to 60). The parasitic effects of the real inductors and capacitors have slightly reduced the bandwidth expected from the simulations.

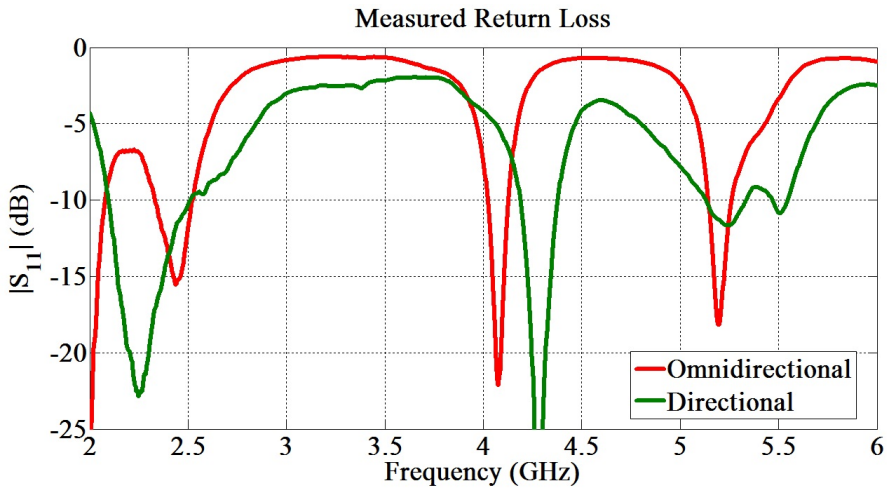

Figure 3.24 Measured return loss when all the elements are connected (Omnidirectional) and when just two adjacent elements are connected (Directional). Good impedance matching is accomplished within the whole 2.4 GHz band and from channel 40 to 60 in the 5 GHz band.

3.4.3 Radiation Patterns

The radiation patterns of the proposed antenna design are shown in Fig. 3.25. When all the elements are connected to the central RF port, an omnidirectional beam is generated. When just two adjacent elements are connected, a directional beam is directed toward the excited pairs. In Fig. 3.25, the active elements for the directional mode are directed toward x and y directions. While the beams at 2.45 GHz appear smooth and clearly defined, the ones at 5.3 GHz exhibit some local magnitude reductions due to the coupling with the longer metallization. At the lower band, the omnidirectional beam is quite uniform around the azimuth plane (x-y) with a gain of 0.7 dBi. The directional beam has a gain of 3.6 dBi and a HPBW of about 45°. At 5.3 GHz, despite the coupling, the 3 dB extension of the omnidirectional peaks covers the entire azimuth plane with a peak gain of 2.4 dBi. The directive beam has a gain of 3.4 dBi and an HPBW of about 30°. The layout allows for

generating four directional beams covering each of the azimuth (x-y) quadrants.

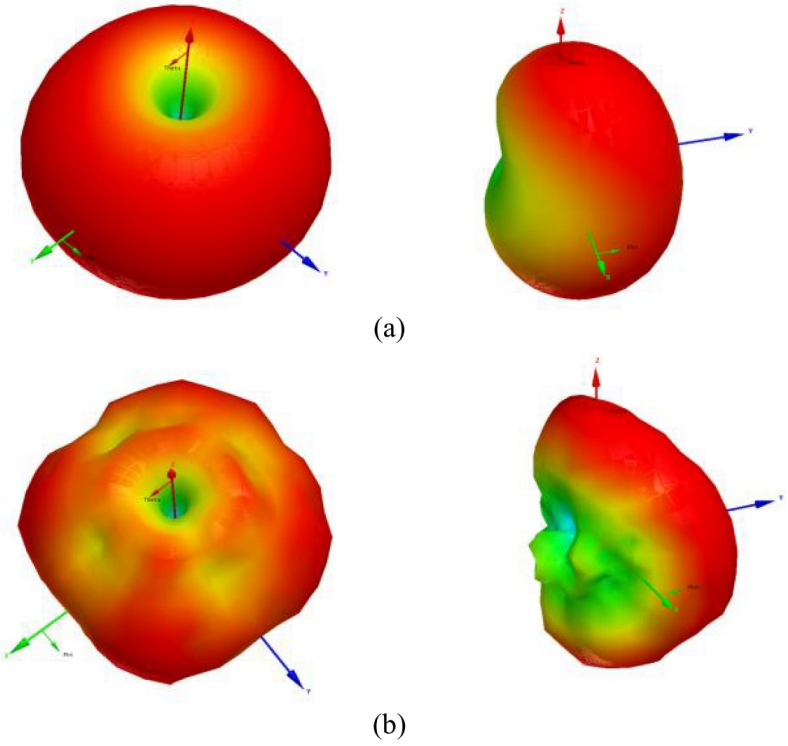

(a)

(b)

Figure 3.25 Simulated radiation patterns. (a) Omnidirectional and directional beams at 2.45 GHz. Gain are 0.7 and 3.6 dBi, respectively. (b) Omnidirectional and directional beams at 5.3 GHz. Gain are 2.4 and 3.4 dBi, respectively. As expected, the beams generated by the internal 5 GHz elements couples with the larger elements, and yielding local magnitude reductions.

3.4.4 Single-band Elements Approach

The multi-band elements approach has the limit that only a single beam at a time can be generated in the two bands. In this second approach, we use two separate sets of 2.4 and 5 GHz elements that can be activated independently to generate 2.4 and 5 GHz beams simultaneously. Once the first set of conductive elements was designed for the 2.4 GHz band, the second smaller 5 GHz set was added within the empty sectors of each quadrant. In other words, the two sets are arranged with a 45° separation as shown in Fig. 3.26(a). The ratio between the radii at the top and bottom layer circles act as a matching network to accom-

plish good impedance matching within both bands. Also in this case, the small parasitics in front of each element are included for enhancing the beams' directivity. Each pair of adjacent 2.4 and 5 GHz elements are connected to the central RF port by lumped diplexers. When integrating PIN diodes, this approach allows for activating 2.4 and 5 GHz elements at the same time, while maintaining good impedance matching. We selected the diplexer model TDK DPX205950DT-9008A1 which is a six-terminal 0805 SMD component with a common RF port and two high and low frequency ports. The component was selected due to its small dimension as well as low insertion loss within the two bands of interest: 0.4 dB at 2.4 GHz and 0.7 dB at 5 GHz [83]. The ground signal needed for the diplexers network is taken from the bottom layer circle through L = 220 nH RF chokes. The dimensions in Fig. 3.26(b) are l_1 = 22.8 mm, l_2 = 18 mm, l_3 = 10.2 mm and l_3 = 8 mm. The two slots lengths are g_1 = 16 mm and g_2 = 4 mm.

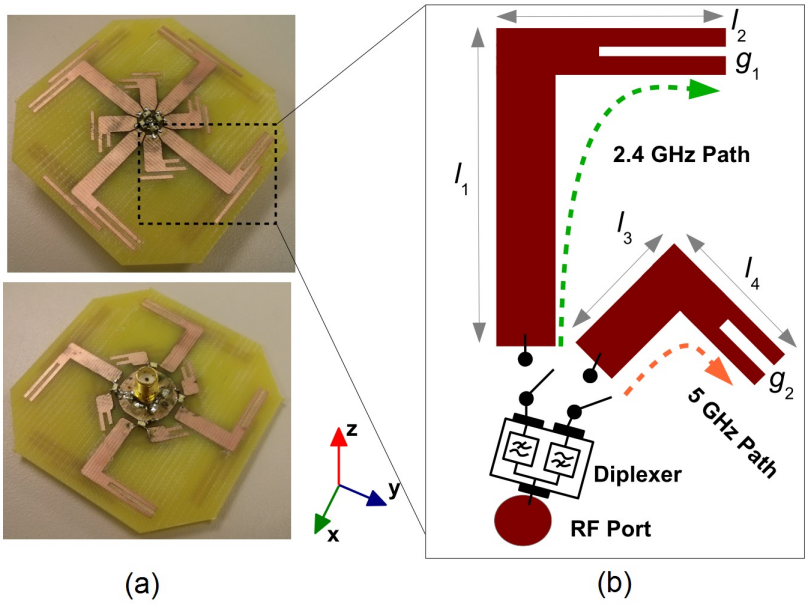

Figure 3.26 (a) Top and bottom layer pictures of the proposed antenna. The total dimensions are 6.5 x 6.5 cm. (b) Detail of a single pair of elements; a lumped diplexer is used to separate the two current flows.

3.4.5 Input Impedance Experimental Results

The manufactured prototype has been populated with the SMD components and measured through an Agilent N5230A Vector Network Analyzer. The return loss characteristics for all of the beam's configurations are depicted in Fig. 3.27. Since each band can generate two types of beams (omnidirectional and directional), there are a total of four states. Similarly to the antenna architecture with multi-band elements, the antenna covers the entire 2.4 GHz band with good impedance matching. At 5 GHz it covers channels 40 to 60. Even though the 10 dB bandwidth has not been improved, the use of diplexers allows for the filtering of undesired resonances outside the two bands. Avoiding undesired resonances allows for blocking signals that may generate 3^{rd} order intermodulation distortions within the bands of interest.

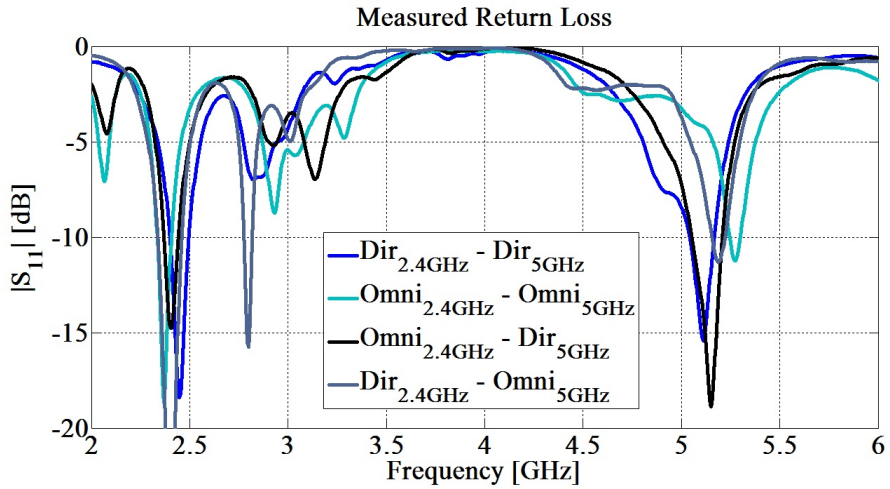

Figure 3.27 Measured return loss for omnidirectional and directional patterns at 2.4 and 5 GHz. Similar to the first approach, good impedance matching is accomplished within the whole 2.4 GHz band and from channel 40 to 60 at 5 GHz. However, the higher selectivity of the diplexer allows for the blocking of larger resonances outside the two bands.

3.4.6 Radiation Patterns

The simulated radiation patterns are shown in Fig. 3.28, according to the coordinate system given in Fig. 3.26. For each set of elements, an omnidirectional beam is generated when all the elements of a set are connected to the central RF port, while a directional beam is generated when only two adjacent elements of a set are connected. Also in this case, four directional beams can be excited, covering all the azimuth (x-y) quadrants. At 2.45 GHz, the beams resemble the ones generated by an ideal single-band 2.4 GHz antenna. In other words, the smaller 5 GHz elements do not interfere with the expected radiation patterns. The gain of the omnidirectional beam is 1.7 dBi, while the directional beam gain is 3.8 dBi. On the other hand, the beams at 5 GHz reveal some local magnitude reductions and side lobes. This effect was expected and it is due to the presence of the larger 2.4 GHz elements, which couples with the radiation coming from the smaller elements. However, the 3 dB extension of each peak in omnidirectional mode allows for the uniform coverage of the entire azimuth plane with a peak gain of 3 dBi, while the directional beam exhibits a clear directivity with a gain of 3.2 dBi and a HPBW of about 40°.

3.5 Summary

In this section we discussed the design of a new compact and planar reconfigurable antenna, the Reconfigurable Alford Loop. The design is beneficial for those applications where the possibility of generating omnidirectional and directional beams can ensure high Quality of Service. The layout is made of four pairs of 90° microstrip elements arranged symmetrically between the top and bottom layers of a standard FR-4 substrate. The antenna is fed by a coaxial SMA port connected to the bottom layer with ground, while the inner conductor

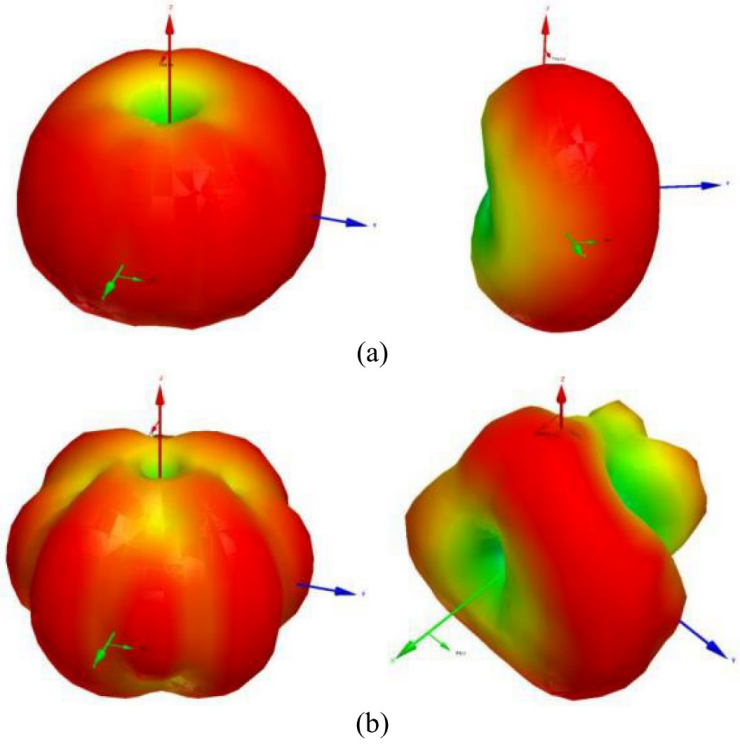

Figure 3.28 Simulated radiation patterns. (a) Omnidirectional and directional beams at 2.45 GHz. Gain are 1.7 and 3.8 dBi, respectively. (b) Omnidirectional and directional beams at 5.3 GHz. Gain are 3 and 3.2 dBi, respectively. As expected, the beams generated by the smaller 5 GHz elements undergo some coupling with the larger elements, resulting in slight local magnitude reductions and side lobes.

is soldered on top through a via hole. A set of RF switches allows to connect or disconnect the elements to the central port, allowing the design to be electrically reconfigurable.

In order to exploit the RALA concept for the newest 802.11 ac dual-band WiFi standard, we have described two approaches for designing dual-band RALAs. The goal was to enable operations within the 2.4 and the 5 GHz WiFi bands. In the first method, we utilized lumped inductors and capacitors for designing single multi-band elements. In the second approach, we combined two distinct sets of single-band elements by means of lumped diplexers. Both approaches demonstrated good return loss within the whole 2.4 GHz band and within part

of the 5 GHz band. By adding PIN diodes, the first design can be used as a simple method for non-simultaneus 2.4 and 5 GHz reconfigurable beams. The second design allows for the simultaneous generation of radiation patterns in the 2.4 and 5 GHz bands at the expense of a higher number of PIN diodes. In both cases, a single antenna can be used from the radio chains of a dual-band WiFi transceiver, leveraging the benefits of omnidirectional and directional beams diversity.

Additionally, we have shown two switching circuits that provide the proper voltage and current to the PIN diodes. The first circuit utilizes MOSFETs and a proper resistive network, while in the second approach we take advantage of phototransistors to design a fully optical switching circuit. By comparing two RALAs equipped with the two different switching circuitry, we have seen that a fully optical control allows generating a more homogeneus beam, since the coupling between DC wires and radiation pattern is avoided. Furthermore, due to the wide bandwidth of operation, a harmonic balance simulation has been performed to investigate the intermodulation distortions that may appear in-band due to PIN diodes. The equivalent circuit model of the RALA was developed by the best fit of the measured return loss. After performing an electromagnetic simulation of the coupling range between two antennas, we considered the application in a 2x2 MIMO system. In the harmonic balance simulation, we have seen that even for higher mutual coupling regimes, the distortions generated are below thermal noise for bandwidth of operation. Additionally, for improved values of mutual coupling, the intermodulation products approaches the typical OFDM noise floor (-110 dBm), which confirms that in both omnidirectional and directional operation, the quality of the signal is not significantly affected by the nonlinearity of PIN diodes. When the RALA is employed in MIMO arrays the experimental

results show very low correlation coefficients, denoting high pattern diversity. Therefore, the aforementioned characteristics enables the RALA to be a valuable solution for future wideband MIMO systems.

Chapter 4: Miniaturization of reconfigurable CRLH Leaky-Wave antennas

4.1 Overview

Composite Right/Left Handed (CRLH) Leaky-Wave Antennas (LWAs) are a class of radiating elements characterized by an electronically steerable radiation pattern. The design is comprised of a cascade of CRLH unit cells populated with varactor diodes. By varying the voltage across the varactor diodes, the antenna can steer its directional beam from broadside to backward θ_1 and forward θ_2 end-fire directions, Fig. 4.1.

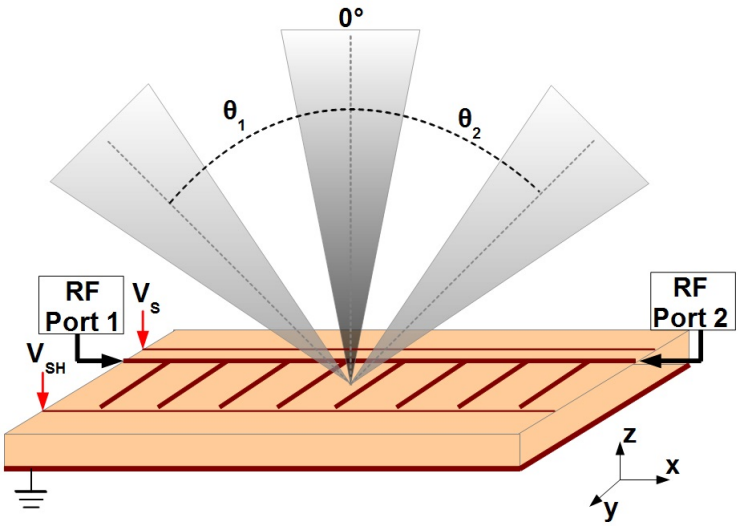

Figure 4.1 Sketch of a two-port CRLH Reconfigurable Leaky-Wave antenna with details of the beamsteering capability.

In this section, we discuss the design and experimental analysis of a miniaturized CRLH Leaky-Wave Antenna for the 2.4 GHz WiFi band [84]. The miniaturization is achieved by etching Complementary Split-Ring Resonator (CSRR) underneath each CRLH unit cell.

As opposed to the conventional LWA designs, we take advantage of a LWA layout that does not require thin interdigital capacitors, thus we significantly reduce the PCB manufacturing constraints required to achieve size reduction. The experimental results were compared with a non-miniaturized prototype in order to evaluate the differences in impedance and radiation characteristics. The miniaturization of LWAs is a significant achievement because it will enable CRLH LWAs to be a viable technology, not only for wireless access points, but also potentially for mobile devices.

4.2 Related Work

One of the most interesting reconfigurable antennas is the design of Composite Right/Left-Handed (CRLH) Reconfigurable Leaky-Wave Antennas (LWAs), a two-port metamaterial-based design that is able to steer its directive beam from broadside to backward and forward angles [9].

The reconfigurable CRLH LWA can be realized as a two-port radiating element with tunable radiation properties. The layout is made by a series of *N* metamaterial unit cells [8], cascaded in order to create a periodic structure from port 1 to port 2, as shown in Fig. 4.2(a). Unlike conventional resonating-wave antennas, the LWA is based on the concept of a traveling-wave. When a radio-frequency signal is applied to one of the input ports, the traveling wave "leaks" out energy as it progressively travels toward the second port. This energy leakage determines the directivity of the radiated beam and is a function of the propagation constant along the structure.

In LWAs, the radiation properties are determined by the complex propagation constant $\gamma = \alpha - j\beta$, where α is the attenuation constant and β is the phase constant. While the

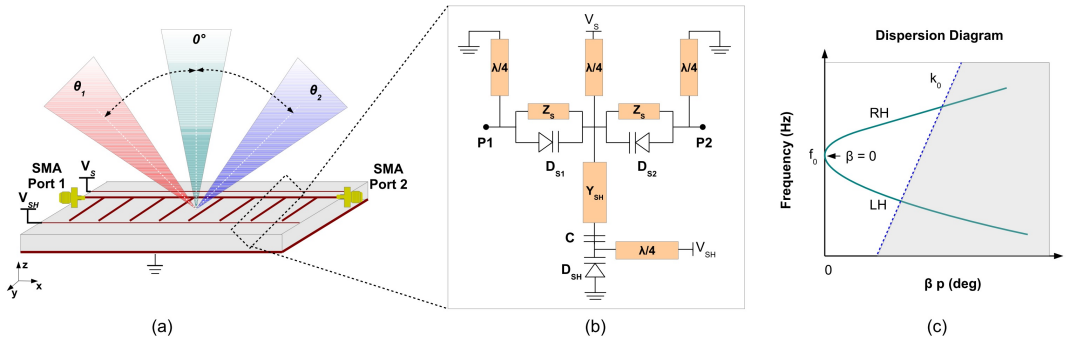

Figure 4.2 (a) Sketch of a CRLH leaky-wave antenna with beam steering from broadside $\theta = 0°$ to backward θ_1 and forward θ_2 angles. (b) Schematic of a conventional CRLH unit cell (c) Dispersion diagram used to evaluate the propagation constant β and estimate the main beam angle θ.

former corresponds to a loss due to the leakage of energy, the latter determines the radiation angle of the main beam. Additionally, the relationship between β and the wavenumber k_0 defines the regions of operation.

The dispersion diagram in Fig. 4.2(c) depicts the absolute value of β and the two regions of operation. The darker area where $|\beta| > k_0$ represents the guided wave, where the energy is propagated from port 1 to port 2. Whereas, the area where $|\beta| < k_0$ represents the radiated region. The angle of the main beam can be determined by the following equation:

$$\theta = \sin^{-1}\left(\frac{\beta}{k_0}\right) \tag{4.1}$$

If we assume that port 2 is fed an input signal and port 1 is terminated with a 50 Ω load, at frequency f_0 where $\beta = 0$, the antenna radiates a main lobe directed normal with respect to the board, in broadside direction $\theta = 0°$. For frequencies where $\beta > 0$ (positive slope of $|\beta|$) the antenna operates in RH region, steering the beam around the left semi-plane θ_1. On

the other hand, when $\beta < 0$ (negative slope of $|\beta|$) it operates in LH region, and radiation occurs within the symmetric half-plane θ_2. This frequency-dependent behavior allows for the scanning of the main beam from back-fire to end-fire directions. The introduction of tunable capacitances in the unit cell can turn the antenna from a frequency-controlled to a voltage-controlled beam steering radiator.

Several voltage-controlled LWAs have been developed in the literature [9, 59] and the circuit model of the conventional metamaterial unit cell can be described as in Fig. 4.2(b). The structure is comprised of both series and shunt components. The series portion is designed with two interdigital capacitors and two varactor diodes D_{S1} and D_{S2} connected in parallel. The shunt portion is composed of a stub and a varactor diode D_{SH} in series. The capacitor *C* acts as DC-block for the two bias lines V_S and V_{SH}. Three $\lambda/4$ microstrip transformers provide the DC bias lines to the diodes. The introduction of varactor diodes allows for a change in capacitance through the reverse bias voltage, and the propagation constant β becomes a function of the diode's voltage. As a result, the curve depicted in Fig. 4.2(c) can be varied along the vertical axis, and the radiator can steer the main beam from backward to forward directions at a given frequency. The aforementioned characteristics make the reconfigurable LWA a very attractive solution for beamforming within commercial WiFi routers and access points. Although the planar and compact form factor of the LWAs make them suitable for wireless base stations, they cannot be exploited on mobile devices due to size constrains. In this dissertation, we will address this limitation by presenting an approach that will make LWAs more suitable for mobile devices.

Current attempts to miniaturize antenna dimensions involve the use of non-conventional substrates with high or enhanced dielectric constant [85, 86]. Other techniques were devel-

oped where the substrate is made by stacking reactive layers [87, 88]. Unfortunately, these techniques introduce more manufacturing complexity and bulk. On the other hand, recent developments in defected ground structures have shown the possibility of simply properly etching the ground plane of transmission lines or antennas in order to change their cut-off and resonant frequencies [89, 90]. As a result, devices with small dimensions can be loaded with complementary resonators on the ground plane to resonate at lower frequencies, achieving miniaturization [91, 92]. We are unaware of any previous work that has achieved reconfigurable antenna miniaturization through defected ground structures (e.g., designing complementary resonators).

In this dissertation, we apply a defected ground technique to achieve miniaturization of reconfigurable antennas. In particular, we build upon an improved LWA design in which, as opposed to the conventional LWAs, we greatly reduce PCB manufacturing constraints by avoiding the use of thin interdigital capacitors. The miniaturized LWA is designed by applying a CSRR underneath each unit cell to achieve miniaturization of the top layer radiating layout. The unit cell is designed and characterized to resonate at 2.4 GHz and provide the largest possible beam-steering. Relative to a conventional 2.4 GHz LWA, the overall dimension can be halved while maintaining good impedance matching, relatively high front-to-back ratio, and good beam steering performance. The miniaturized LWA is designed to exhibit good impedance matching within the 2.41 - 2.48 GHz band, for WiFi operations on mobile devices such as laptops or tablets.

4.3 Improved LWA Design

In this section, we show the design of a composite right/left handed two port leaky-wave antenna (CRLH LWA), having reduced size and enhanced beam steering capabilities. The antenna is made of a cascade of metamaterial CRLH unit cells, populated with varactor diodes. By properly designing the CRLH unit cell, the propagation constant has been optimized within the radiated zone, achieving maximum beam steering and keeping a nearly constant gain for all of the beam configurations. The improved CRLH LWA has been designed using the full wave electromagnetic simulator HFSS and tuned to operate within the 2.4 GHz WiFi band. The layout is etched on a standard FR-4 substrate, having dielectric constant ϵ_r = 4.4 and thickness t = 1.6 mm.

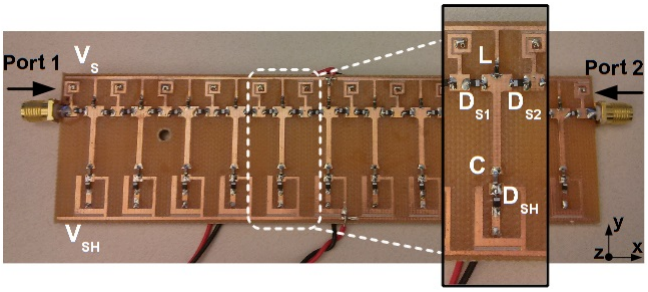

Figure 4.3 CRLH LWA prototype and unit cell details.

As illustrated in Fig. 4.3, the antenna consists of 11 metamaterial unit cells and has the overall dimensions of: length L = 140 mm and height H = 40 mm. The CRLH behavior is determined by designing the unit cell to have proper series capacitance and shunt inductive component by means of a shunt microstrip stub. The series capacitance can be varied through two varactor diodes D_{S1} and D_{S2}, while the shunt component is varied through the varactor D_{SH}. A 0.5 pF capacitor (C) was added to the shunt stub in order to decouple the two bias voltages V_S and V_{SH}. Thus, these two bias voltages will modulate the propagation

constant β along the waveguide and provide the beam steering determined by:

$$\theta = \sin^{-1}\left(\frac{\beta_{S,SH}}{k_0}\right) \tag{4.2}$$

In order to exploit the maximum beam steering capability, the unit cell was optimized to sweep within the entire LH radiating region of the dispersive curve. In this way, by switching between the two input ports, the beam can be steered from broadside to positive and negative angles. Beyond θ = 60°, the propagation constant β approaches the guided region and the directivity of the radiated beam is degraded. Unlike previous LWA designs [37, 93], the proposed antenna avoids the use of interdigital capacitors as part of the CRLH equivalent model. Thus, we avoid the manufacturing challenges that may be introduced by etching the very thin fingers that constitute the interdigital capacitors. Consequently, enhanced symmetry between the two input ports is achieved as shown in the following sections. The form factor of the antenna has also been reduced by designing the DC lines with spiral and folded rf-chokes as well as using lumped elements (L).

4.3.1 Experimental Results

The return loss of the antenna and the isolation between the two input ports have been measured using an Agilent N5230A network analyzer. The S_{11} and S_{22} scattering parameters describe the impedance integrity between the input ports and the 50 Ω feed line, whereas the S_{21} renders the isolation achievable between them. Figure 3 shows measurements of scattering parameters for different V_S and V_{SH} configurations, corresponding to beam angles θ = 0°, θ = $\pm$30°, and θ = $\pm$60° at the frequency of 2.46 GHz. For all the beam steering

configurations, the CRLH LWA exhibits good impedance matching below the 10 dB target in both input ports. The discrepancy between S_{11} and S_{22} is very limited and potentially due to manual population of the board. The isolation between the two input ports is well below 10 dB, allowing us to use the CRLH LWA as a two-element array antenna in a wireless multiple input multiple output (MIMO) system.

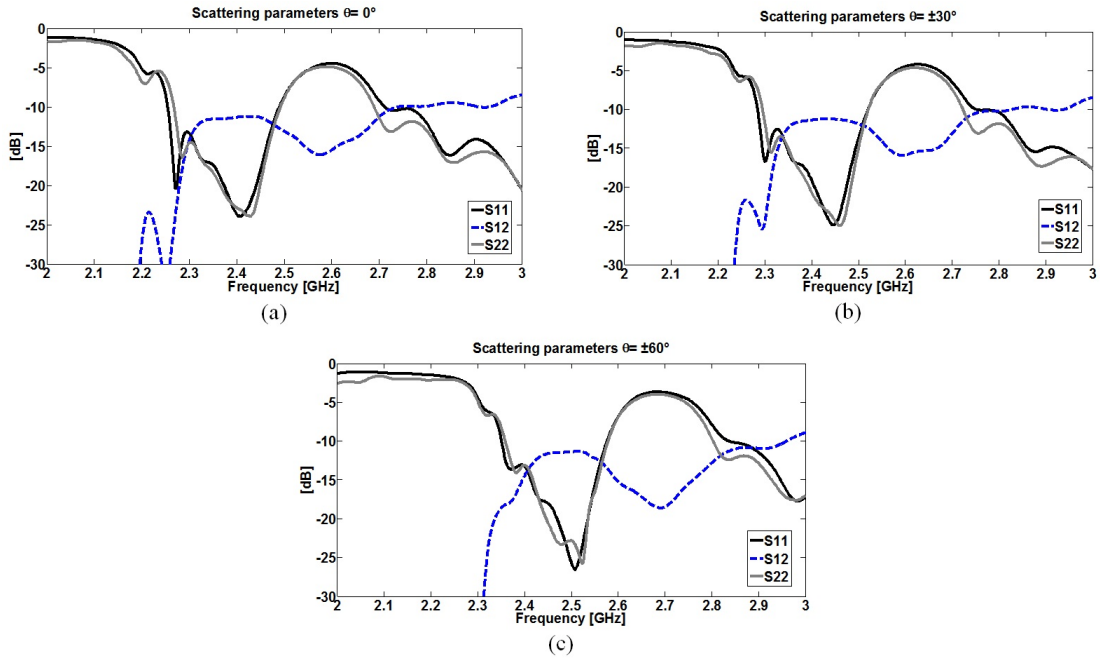

Figure 4.4 Measured scattering parameters of the CRLH LWA: (a) V_S = 12 V - V_{SH} = 11 V, (b) V_S = 14 V - V_{SH} = 16.5 V, (c) V_S = 20 V - V_{SH} = 18 V.

Table 4.1 Summary of Four Different Configurations at the Frequency of 2.46 GHz

Configuration $\{ V_S, V_{SH} \}$	Gain	Beam Angle θ
{12 V, 11 V}	4.1 dB	0°
{12.5 V, 12.5 V}	3.9 dB	±10°
{14 V, 14 V}	4.0 dB	±20°
{14 V, 16.5 V}	3.8 dB	±30°
{16.5 V, 16.5 V}	3.6 dB	±40°
{18 V, 18 V}	3.2 dB	±50°
{20 V, 18 V}	2.8 dB	±60°

Radiation pattern measurements of the CRLH LWA were conducted at a frequency of

2.46 GHz within the anechoic chamber facility at Drexel University. To characterize the full beam steering capability of the antenna, the patterns were measured in steps of $\theta = 10^{\circ}$ and are summarized in Table 4.1. The positive angles were measured by connecting port 1 and terminating port 2 in a 50 Ω load, while negative angles are relative to port 2 and port 1 terminated in a 50 Ω load. As shown in Figure 4, the gain for each pattern is between 3 and 4 dBi, and is relatively constant for all beam configurations. A slight reduction of the gain occurs for angles greater than $\theta = \pm 50^{\circ}$ since the propagation constant β starts to leave the radiated regime.

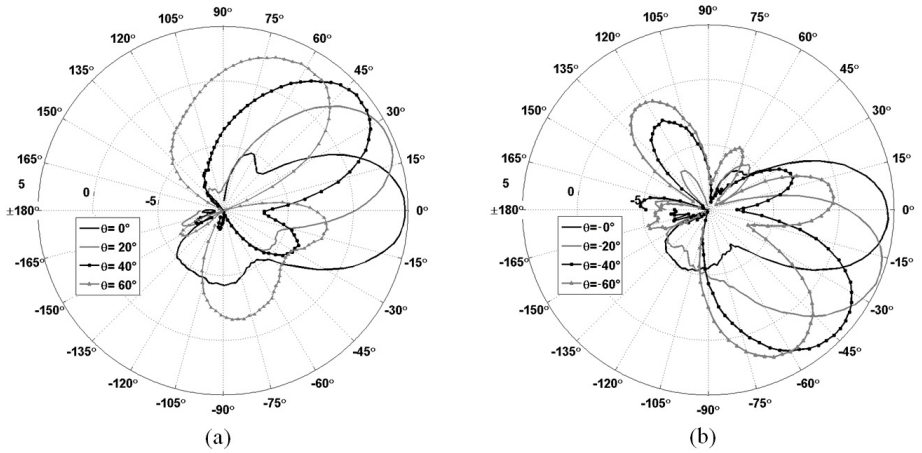

Figure 4.5 Measured radiation patterns (*z*-*y* plane) of the CRLH LWA: (a) Positive angles, port 1 connected, (b) Negative angles, port 2 connected.

4.4 Application for Direction Of Arrival Estimation

Direction of arrival estimation using compact antenna arrays are of great importance to future cognitive radio systems. This technique defines the ability to estimate the direction from which a received signal is coming, which is a useful information for applications such as localization and reconfigurable antenna state selection [93, 94, 95]. The spectrum reuse and sensing performance can be greatly improved by using spatial dimension with the help

of reconfigurable antennas, DoA estimation and beamforming techniques [96], [97], [98], [99]. By using these techniques in concern in cognitive radio environments, it is possible to reduce multiple access interference and enhance the performance of cognitive users.

Due to its beam steering capabilities, the CRLH LWA is one of the best antenna candidates for DoA estimation. In a previous work [93], the MUSIC algorithm was modified for a two-port LWA. The paper shows how the correlation matrix can be formed by using the two ports of the LWA and how the spatial diversity of the conventional antenna array can be recreated with a LWA. In [100] we performed a DoA analsys through a MUSIC algorithm, properly modified to adapt the steering vector to the improved LWA design discussed in Section 4.3.

The modified MUSIC algorithm along with the CRLH LWA was tested in an anechoic chamber facility, as illustrated in Fig. 4.6.

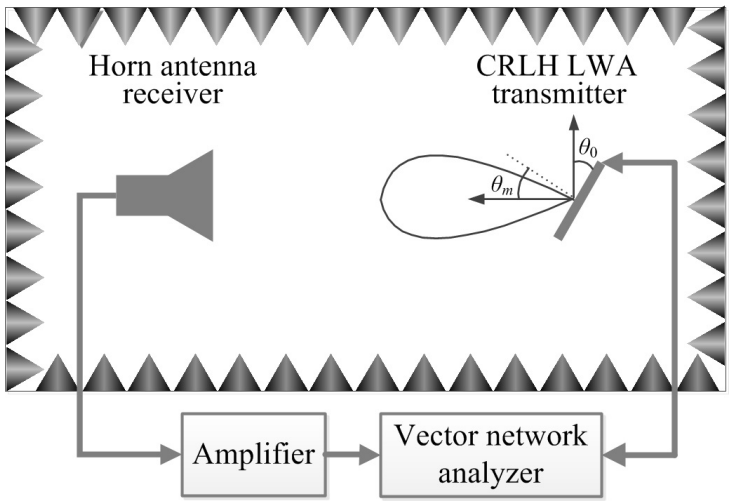

Figure 4.6 Anechoic chamber DoA measurement setup.

The LWA was set as a transmitter of 64 subcarriers signals within the frequency range from 2.452 GHz to 2.472 GHz. A horn antenna was at the receiver side. The signal was

transmitted from 12 different directions (θ = -60° to θ = +50° in steps of 10°) by setting the bias voltages V_S and V_{SH}. The wireless channel has been assumed reciprocal because of the anechoic chamber environment. During the measurements, we considered four different DoA angles: -15°, -25°, -35° and -45°. The length of the LWA cell is set d = 16.5 mm and the leakage factor α = 1. The modified MUSIC spectrum is calculated by averaging over the number of subcarriers.

The plot in Fig. 4.7 shows the power spectrum as a function of the DoA angles for the proposed CRLH LWA. The estimated DoA are in very good agreement with the expected angles, with results summarized in Table 4.2. According to the measured results, the improved LWA design, which has been miniaturized, can successfully estimate the direction of a receiving signal with high accuracy. Such a system could be a valuable solution for future cognitive radio platforms.

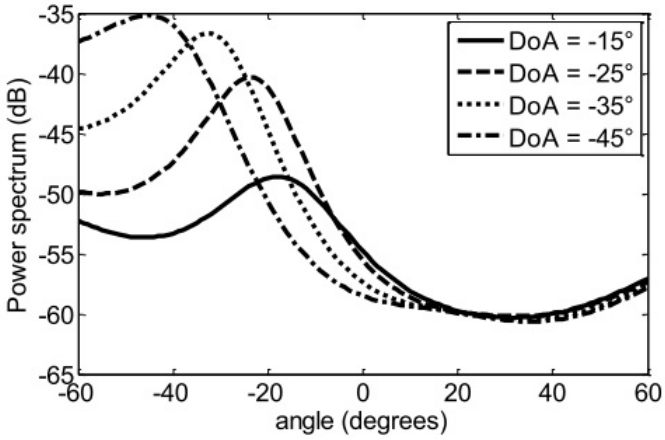

Figure 4.7 Measured DoA performance using the proposed CRLH LWA and modified MUSIC algorithm.

Table 4.2 Comparison Between Expected and Measured DoAs.

Expected DoA	Measured DoA	Error
-15	-18	2.5 %
-25	-24	0.8 %
-35	-33	1.7 %
-45	-45	0.0 %
Average		1.25 %

4.5 Design of the Miniaturized CRLH LWA Unit Cell

The improved LWA described in the previous sections is suitable for further miniaturization and integration within mobile devices. The first step for the miniaturization through Complementary Split-Ring Resonators (CSRR) is the re-design of the metamaterial unit cell. The LWA unit cell, shown in Fig. 4.8(a), was designed on a conventional FR-4 substrate having dielectric constant ϵ_r = 4.4 and thickness t = 1.6 mm. The top layout, as well as the CSRR, were tuned to operate within the entire 2.4 GHz 802.11 WiFi band.

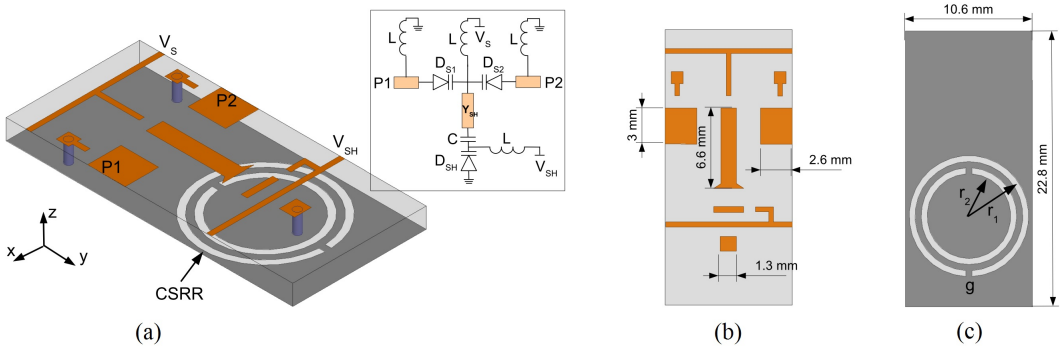

Figure 4.8 (a) 3D HFSS model of the LWA unit cell, with CSRR etched on the ground plane. (b) 2D top layer layout and dimensions. (c) Bottom layer with ground plane and CSRR design. r_1 = 5 mm and r_2 = 4 mm. The gap g and the distance between the two rings is 0.5 mm.

The unit cell was designed and tuned using the full-wave electromagnetic simulator

Ansoft HFSS [63]. In order to perform more realistic simulations, each lumped component was measured through a two-port fixture and a Vector Network Analyzer (VNA). The S-parameters (S2P) were then loaded into the circuit simulator Ansoft Designer [101]. The co-simulation between HFSS and Designer allows for evaluation of the 3D model using the actual S2P parameters. As a varactor diode, we selected an Infineon BB833 [102], designed to operate up to 2.5 GHz. In order to get a qualitative evaluation of the capacitance range and loss under reverse bias voltage, we extracted the junction capacitance C_J and the series resistance R_S from the measured S2P. The plot in Fig. 4.9 shows that the series resistance falls within the range 1.7 $\Omega \leq R_S \leq$ 1.85 Ω within the entire reverse voltage sweep. However, when $V_R \leq$ 10 V, the junction capacitance exhibits larger dynamic range: 18 pF $\leq C_J \leq$ 3 pF. The final unit cell layout has been optimized to take advantage of this large C_J variation under low bias voltages.

The CRLH behavior is determined by designing the unit cell to have proper series capacitance and a shunt inductive component. The series capacitance is achieved by placing two varactor diodes in series with a common cathode (D_{S1} and D_{S2}). The inductive part is designed by means of a shunt stub with a varactor diode (D_{SH}) placed in series. The dynamic tuning is accomplished by changing the reverse voltage V_R of the two bias line V_S and V_{SH}. A C = 0.5 pF capacitor was added to the shunt stub in order to decouple the two bias voltages. To further reduce manufacturing complexity and form-factor, we have used L = 220 nH inductors that act as RF-chokes to provide the two bias voltages. The inset in Fig. 4.8(a) depicts the resulting schematic of the LWA unit cell. The dimensions are shown in Fig. 4.8(b), and the gaps are properly designed to include the lumped components.

Simulations have shown that by using a standard ground plane, the proposed unit cell

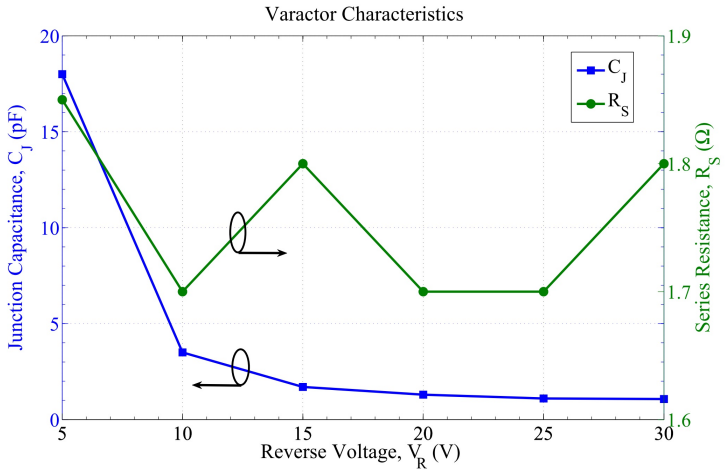

Figure 4.9 Junction capacitance C_J and series resistance R_S as function of the reverse voltage V_R. The values were extracted from the measured S-parameters. While R_S maintains a relatively constant value within the entire voltage sweep, the capacitance C_J exhibits a larger dynamic range when $V_R \leq 10$ V.

operates in the frequency region of 5 GHz. In order to reduce the operating band, a single CSRR was etched underneath the unit cell. The dimensions of the CSRR were varied to reduce the operational frequency to 2.45 GHz and the optimal layout is shown in Fig. 4.8(c). The outer radius is r_1 = 5 mm, while the inner radius is r_2 = 4 mm. The gap g on both rings, as well as the distance between them, is 0.5 mm. The CSRR was slightly moved from the center to the shunt part of the unit cell in order to reduce the radiation from the ground plane and enhance the front-to-back ratio.

The CRLH unit cell can exhibit balanced or unbalanced resonances, based on the series and shunt resonant frequencies ω_{se}, ω_{sh}. While unbalanced-type ($\omega_{se} \neq \omega_{sh}$) supports two different frequencies, the lower for the LH and the higher for the RH region, we used balanced-type unit cell ($\omega_{se} = \omega_{sh}$) in order to avoid the gap between the RH and LH regions and match the structure over a broad bandwidth. In terms of radiating regions, a

CRLH unit cell can typically operate in either RH or LH regimes. However, in order to achieve the maximum beam coverage by switching between the two input ports, we have optimized the design within the RH region ($|\beta| > 0$). Similarly to [103], port 1 is used and the beam can be steered from 0° to $\max\{\theta_2\}$, whereas by switching to port 2 the beam covers the symmetrical quadrant from 0° to $\max\{\theta_1\}$. This design choice enables full-space beam steering while taking advantage of the high C_J variation under low voltage regimes. Due to the two-port switching, a similar beamsteering mechanism can be achieved using unbalanced-type CRLH unit cells.

The next subsection describes the experimental analysis conducted on a miniaturized unit cell prototype. We evaluated the impedance characteristics and the expected radiation angles from the dispersion diagram.

4.5.1 Experimental Results

S-parameter measurements were carried out to assess the performance of a miniaturized unit cell prototype and validate the simulation results. The unit cell was etched between two $\lambda/8$ transmission lines for soldering the SMA connectors. An Agilent N5230A Vector Network Analyzer was calibrated with the port extension function for de-embedding the two extra lengths. Top and bottom layers of the manufactured unit cell are shown in Fig. 4.10.

Fig. 4.11 shows measured and simulated S-parameters for four arbitrary configurations. Due to port symmetry, in this plot we assume S_{11} = S_{22} and S_{12} = S_{21} for greater visual clarity. By observing the S_{11} curves, we can note that the proposed miniaturized unit cell maintains good impedance matching within the bandwidth of interest from 2.41 to 2.48

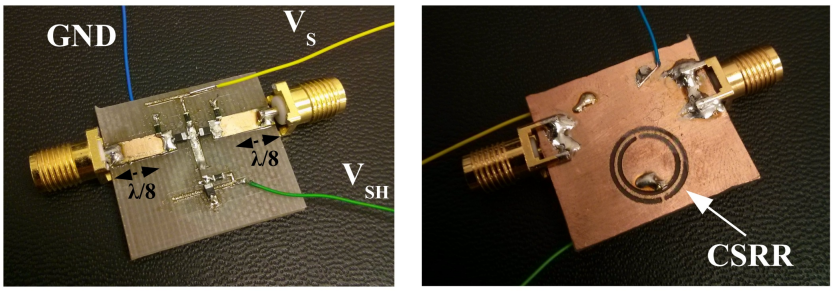

Figure 4.10 Top and bottom layer pictures of the miniaturized LWA unit cell. The design is etched between two $\lambda/8$ microstrip lines for S-parameter measurents.

GHz. The 10 dB bandwidths are between 220 MHz $\leq BW \leq$ 650 MHz. While the series voltage V_S has major control in changing configurations, the voltage V_{SH} allows for fine-tuning the S-parameters, maintaining the Block impedance relatively constant and close to 50 Ω. The insertion loss, which includes both actual losses and radiation leakage, is between 0.8 dB $\leq S_{21} \leq$ 1.5 dB among the different configurations. The higher deviation between simulation and measurement at the two sides of the bandwidth is potentially due to the S-parameters fixture used to extract the S2P of each lumped component.

In order to evaluate the beam steering capabilities, the dispersion diagram was created using the following equation [104] and the measured S-parameters:

$$\beta p = \cos^{-1}\left(\frac{1 - S_{22}S_{22} + S_{21}S_{12}}{2S_{21}}\right) \tag{4.3}$$

The dispersion diagram in Fig. 4.12 shows the result of four different configurations. We can note that within the bandwidth of interest, the curves are upward sloping, denoting operation in RH regime. The expected radiation angles θ can be estimated through the equation shown in the inset of Fig. 4.12 and computed at the desired frequency. By assum-

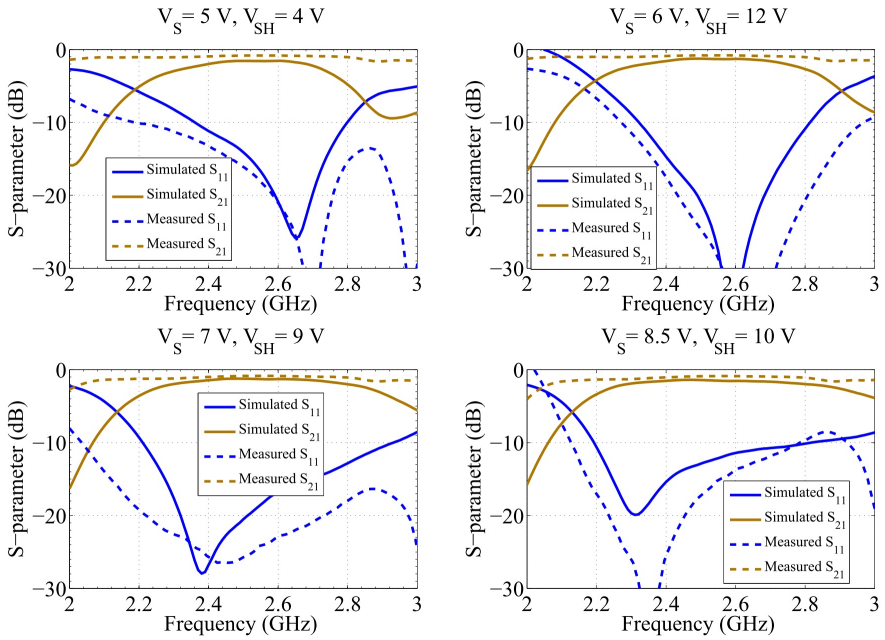

Figure 4.11 Simulated and measured S-parameters for four different configurations. While V_S acts as major controller for the center frequency, V_{SH} allows for fine-tuning and improvement of the impedance.

ing WiFi operation at 2.46 GHz (channel 11), the miniaturized unit cells allow for steering the radiated beam approximately from $\theta = 21°$ to $\theta = 55°$ with respect to broadside direction. Although the continuous biasing of varactor diodes allows for a theoretically infinite number of configurations, in Table 4.3 we summarize four significant configurations to achieve uniform beam steering. The relative Block impedance Z_b and expected beam angle θ are also reported.

Table 4.3 Summary of Four Different Configurations at the Frequency of 2.46 GHz

Configuration $\{ V_S, V_{SH} \}$	Block Impedance Z_b	Beam Angle θ
{8.5 V, 10 V}	$42 + j8\ \Omega$	21°
{7 V, 9 V}	$37 + j7\ \Omega$	28°
{6 V, 12 V}	$47 + j10\ \Omega$	38°
{5 V, 4 V}	$56 + j9\ \Omega$	55°

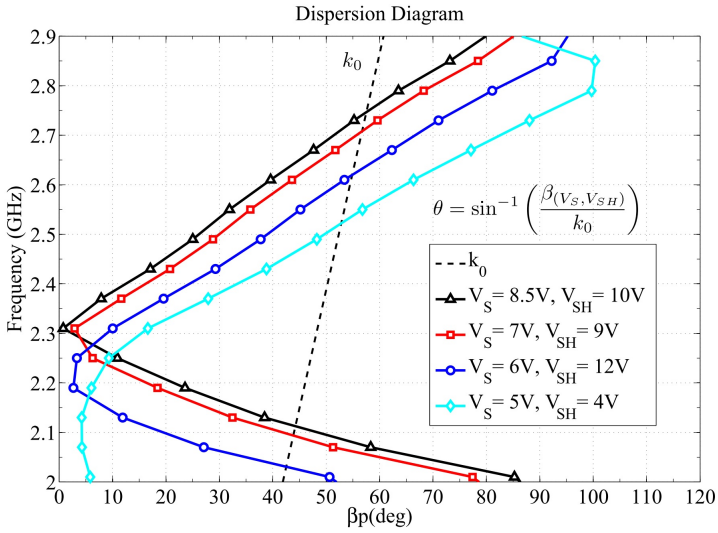

Figure 4.12 Dispersion diagram of the proposed miniaturized CRLH unit cell. The four different states were taken for incremental values of bias voltages V_S V_{SH}. The desired frequency bandwidth, 2.41 - 2.48 GHz, falls within the RH radiated region.

The aforementioned results enable the cascading of the miniaturized unit cell to create a complete leaky-wave antenna for the 2.4 GHz WiFi band. In the next section, we discuss the design of a reconfigurable CRLH LWA made by cascading 11 miniaturized unit cells, with experimental analysis of impedance and radiation characteristics.

4.6 Miniaturized CRLH LWA Antenna

The periodic structure of the miniaturized CRLH LWA was designed by cascading a series of unit cells described in the previous Section. As illustrated in Fig. 4.13, the antenna consists of N = 11 unit cells and has overall dimension l = 11.5 cm and h = 2.3 cm. The number of unit cells was selected to achieve positive gain and obtain a fair comparison with the earlier LWA presented in [100]. By switching between the two input ports, the antenna allows for the generation of two independent beams that can be steered from back-fire to

end-fire, with expected beam angles θ estimated during the unit cell analysis.

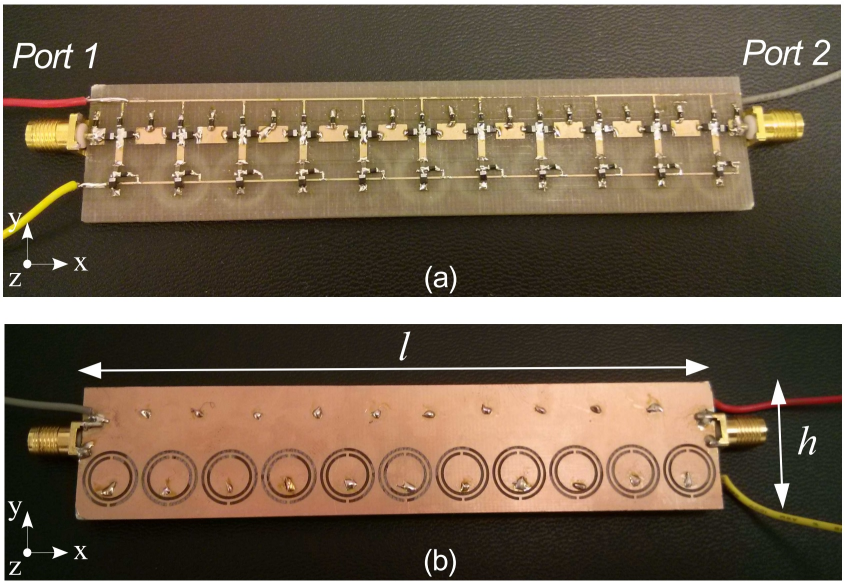

Figure 4.13 Picture of the miniaturized CRLH LWA. (a) Top layer with cascade or $N = 11$ unit cells. (b) Bottom layer with CSRRs. The overall dimensions are: $l = 11.5$ cm, $h = 2.3$ cm.

4.6.1 Input Impedance Experimental Results

The return loss and the isolation of the two input ports have been measured through a VNA. The S_{11} and S_{22} scattering parameters describe the impedance integrity between the antenna's ports and a 50 Ω feed line, whereas the S_{12} and S_{21} render the isolation achievable between them. Fig. 4.14 shows the measured scattering parameters for the four configurations listed in Table 4.3.

Both input ports exhibit good impedance matching within the 2.41 - 2.48 GHz band, the small discrepancies between the S_{11} and S_{22} curves are potentially due to the manufacturing process and, in particular, the manual population of the board. We also note that the 10 dB bandwidth is relatively large, between 1 GHz $\leq BW \leq$ 1.3 GHz. In terms of decoupling between the two port, at 2.46 GHz the antenna's isolation is within the range of 8 dB $\leq S_{21}$

$\leq$ 10 dB.

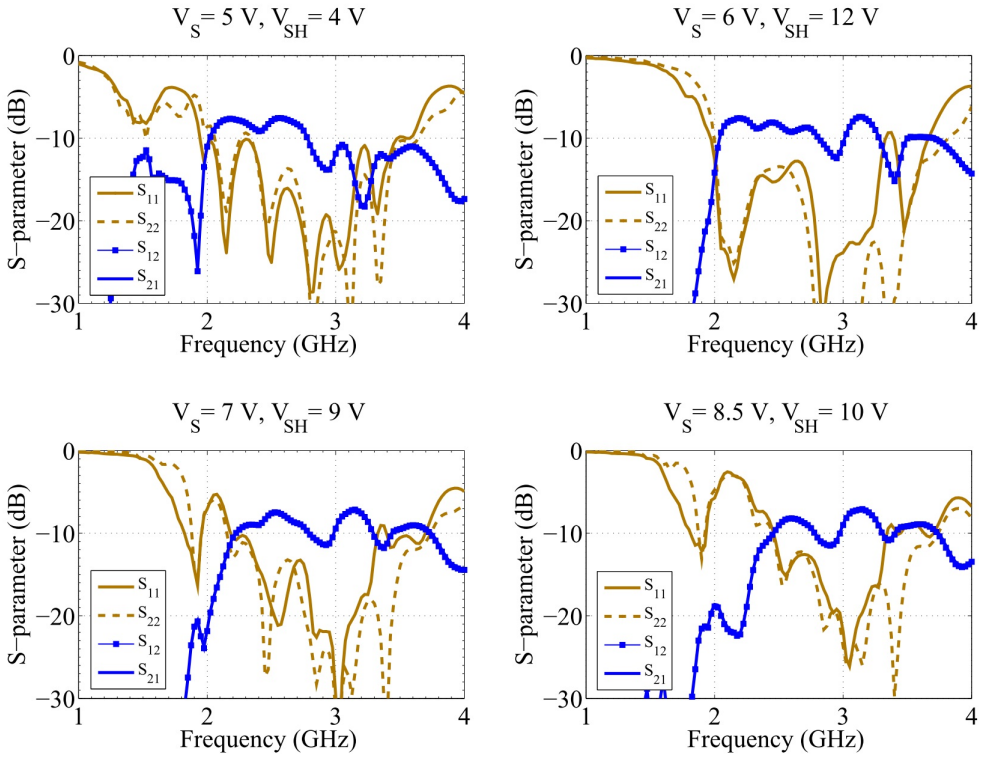

Figure 4.14 Measured S-parameters of the miniaturized CRLH LWA.

4.6.2 Radiation Patterns Experimental Results

In order to evaluate the radiation characteristics of the proposed antenna and the agreement with the expected angles, we have measured the radiation patterns for the four configuration listed in Table I. For this purpose, we used the tool EMSCAN RFxpert [77], which is a bench-top measurement system than enables us to get 3D and 2D antenna pattern measurements in real time. Fig. 4.15 shows the 3D antenna directivity graphs measured at 2.46 GHz by exciting port 2 and terminating port 1 to a 50 Ω load. The steering angles are in good agreement with the expected values. The minimum gain is 0 dBi while the peak is about 2 dBi, with a front-to-back ratio between 5 and 8 dB, depending on the adopted con-

figuration. Further measurements were conducted in an anechoic chamber and Fig. 4.16 illustrates the azimuth cut (*x*-*z*) with the complete set of radiation patterns accomplished by switching between the two input ports. The total steering angle is about 120° and the half-power beamwidth (HPWB) of each beam, between 40° and 60°, allows for nearly uniform coverage.

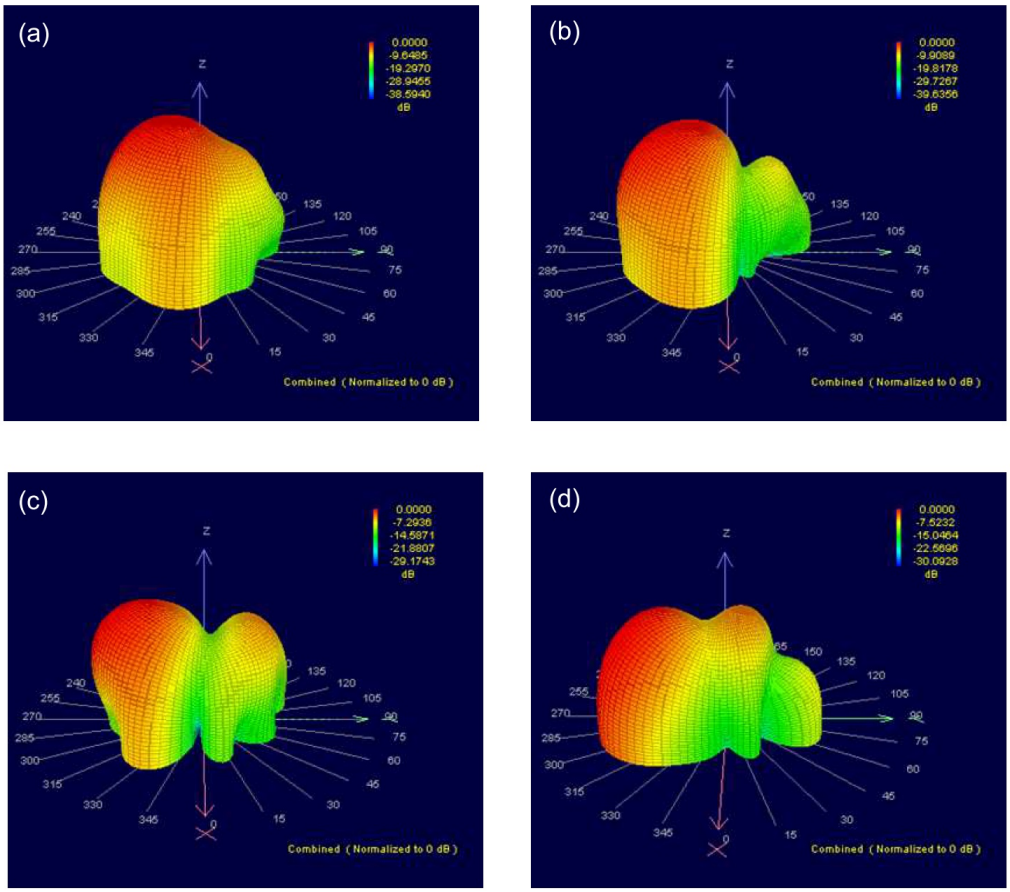

Figure 4.15 Measured 3D radiation patterns at 2.46 GHz for four configurations. Port 2, oriented in +*y* direction was connected to a signal generator, while port 1 was terminated to a 50 Ω matched load. (a) V_S = 8.5 V, V_{SH} = 10 V (b) V_S = 7 V, V_{SH} = 9 V (c) V_S = 6 V, V_{SH} = 12 V (d) V_S = 5 V, V_{SH} = 4 V.

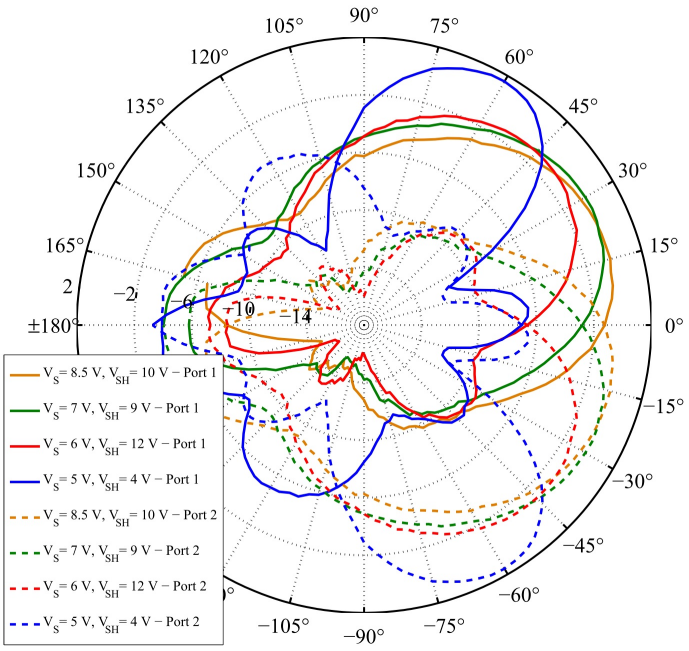

Figure 4.16 Azimuth (x-z) view of the total beam steering capabilities. The solid lines depict beams generated by exciting port 1 (and port 2 terminated to a 50 Ω load), whereas the dashed beams with port 2 (and port 1 terminated to a 50 Ω load).

4.6.3 Comparison with Conventional LWA Model

In Fig. 4.4, we compare the size of the proposed miniaturized LWA with an earlier conventional design of a LWA [100]. Both antennas were designed by cascading 11 unit cells, however, the miniaturized LWA is about 47 % smaller than the conventional LWA. We then conducted a qualitative comparison of the electrical and radiation characteristics to evaluate the performance of the proposed miniaturized LWA. A summary is shown in Table II.

The 10 dB bandwidth of the miniaturized LWA is significantly larger than the conventional model. However, it is important to recall that due to the frequency-dependency, different frequency regions will exhibit different handedness regions (i.e., RH or LH) and thus different steering angles. Moreover, when the dispersion curve approaches the propa-

gation regime, the beam's directivity and gain degrade.

Due to the smaller dimension, the isolation between the two input ports is lower with respect to the standard model. Although more than 85 % of the energy is being radiated and attenuated through the structure, the employment of a single-pole-double-throw (SPDT) switch would allow for further decoupling of the two ports and switch between them to generate the desired back-fire and end-fire beams. Furthermore, the cascade of additional unit cells can also lead to higher isolation between the ports and increases the radiated gain.

In terms of radiation characteristics, the miniaturized LWA allows for beam steering of about 120° around the azimuth plane, similar to the earlier version. The peak gain is 2 dB lower, but sufficient to utilize the antenna for mobile applications [105]. The front-to-back ratios are comparable, with both antennas performing between 4 and 8 dB, depending on the adopted configuration.

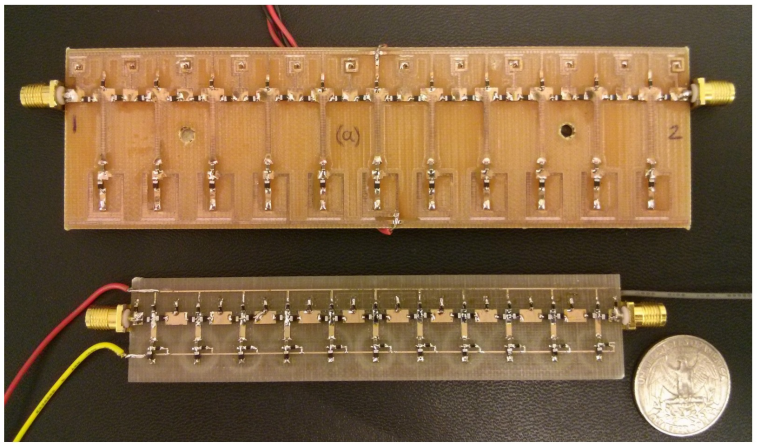

Figure 4.17 Comparison between the conventional and the proposed miniaturized reconfigurable LWA. Both antennas were designed by cascading $N = 11$ unit cells. The former occupies an area of 56 cm^2 while the latter 26.5 cm^2.

Table 4.4 Comparison Between Conventional and Miniaturized LWAs

	Conventional LWA	Miniaturized LWA
Dimension	56 cm^2	26.5 cm^2
10 dB Bandwidth (Max)	30 MHz	1.3 GHz
Isolation (min)	10 dB	8 dB
Peak Gain	4 dBi	2 dBi
Front-to-Back Ratio (avg)	8 dB	7 dB
Beamsteering Coverage	120°	120°

4.7 Summary

In this section we have shown the design of a miniaturized reconfigurable leaky-wave antenna (LWA), where the size reduction was accomplished by etching a complementary split-ring resonator (CSRR) underneath each unit cell. The CSRR was designed to decrease the size of an improved design of CRLH unit cell, covering the whole WiFi band from 2.41 GHz to 2.48 GHz. The absence of interdigital capacitors greatly reduces manufacturing constraints for size reduction while also allowing the application of the CSRR miniaturization technique. As an example of system level application, the improved LWA design has been applied for Direction Of Arrival Estimation. According to the measurements obtained within an anechoic chamber and a dedicated MUSIC algorithm, the LWA showed high accuracy in estimating the direction of incoming signals.

Numerical and experimental analysis of the miniaturized unit cell have shown good impedance performance and relatively large variations of the dispersion curves, which leads to large beam steering. After fine tuning the unit cell for the desired radiating region and steering angles, the miniaturized leaky-wave antenna has been designed by cascading 11 unit cells. With respect to an equivalent conventional LWA model, the miniaturized antenna

is 47% smaller and exhibits a larger 10 dB bandwidth. The radiation patterns were in good agreement with the expected angles and the total azimuth coverage is about 120° with gains between 0 and 2 dBi.

In conclusion, the technique of etching CSRR on reconfigurable leaky-wave antennas has been shown to be successful for size reduction and maintenance of good radiating performance. The proposed solution enables the development of miniaturized reconfigurable antennas that do not require expensive and customized substrates.

Chapter 5: Wearable Strain Sensor Through Frequency-Reconfigurable Antennas and RFID Technology

Recent advancements in conductive yarns and fabrication technologies offer exciting opportunities to design and knit seamless garments equipped with sensors for biomedical applications. In this dissertation, we discuss the design and application of a textile frequency reconfigurable antenna which can be used for biomedical monitoring, such as contraction, respiration, or limb movements. This wearable sensor system takes advantage of the intensity variations of the backscattered power (RSSI) from an inductively coupled RFID tag under physical stretching. First, we describe the antenna design along with a preliminary analysis of the RSSI sensitivity. Next, we perform a numerical simulation of a textile version of the same antenna, modeling the structuring through a sheet impedance, which characterizes the conductive textile. After knitting the prototype we measured the input impedance through a differential scattering parameter technique, which is a method for measuring the balanced input port of this radiator. Furthermore, we also validated the radiation characteristic of the antenna through radiation measurements within the anechoic chamber. The experimental results with the custom fabricated prototypes show good agreement with the numerical estimation. Finally, we will discuss the human body loading effects and the performance results when the sensor is employed for biomedical strain sensing.

5.1 Related Work

Recently, the integration of wireless smart devices into clothing has revolutionized the monitoring of physical activities and wellness. These garments incorporate physiological sensors and low-power computing units allowing for continuous biomedical monitoring and activity tracking [106, 107]. By adding low-power transceivers such as Bluetooth Low Energy devices (BLE), the information can be conveniently transmitted to mobile devices. However, these devices typically use additional dedicated transceiver modules and require batteries or other sources of energy.

Radio-Frequency Identification (RFID) technology is being increasingly utilized in an expanding set of applications. For traditional metal-based tags, it has been shown that the backscattered power (RSSI) transmitted from a passive RFID tag can be used as a wireless metric for detecting material deformations [108, 109]. In other words, when a strain force is applied on an RFID tag, the physical deformation of the embedded antenna causes a shift of its resonant frequency. Consequently, the RSSI variation received from the interrogator can be correlated to the mechanical deformation of the object where the tag is installed.

In this dissertation, we propose to take advantage of this new application of RFID technology, along with advances in knitting-based fabrication techniques, to realize comfortable and battery-less wearable strain sensors. These sensors can be used for monitoring contraction, respiration, or limb movements. In other words, these sensors can be used for all applications where a mechanical movement causes stretching and changes in RSSI responses. As a result, the desired wearable wireless strain sensor should meet the following requirements:

- comfortable to wear
- highly stretchable
- good impedance matching between antenna and microchip
- sufficient radiating characteristics to maintain communication under different levels of physical deformation.

The feasibility of building electrical devices using conductive fabrics has been analyzed through electrical characterization of transmission lines [110]. Several papers have demonstrated mounted wearable transmission lines and antennas where conductive fabrics are applied onto woven fabrics [111]. Previous work shows conductive copper foil or fabrics bonded to a flexible substrate [112, 113]. These techniques show limitations in terms of electrical losses and bulkiness. Specifically, limitations have been shown in terms of electrical characteristics by using adhesive or glue. We address these drawbacks by knitting conductive and non-conductive yarns in a single process, resulting in smart textiles that are unobtrusively integrated into the host garment, eliminating the need for chemical adhesives that degrade performance and decrease elasticity. Specifically, in this dissertation we investigate the feasibility and the radio frequency performances of designing a high frequency dipole using conductive yarns through a conventional knitting technique.

Implementing wireless devices using this knitting technique has several advantages over the current method of cutting and sticking conductive fabrics. First, the implementation is directly made by the clothing fabrication process, there's no need for cutting and sewing different fabrics. Additionally, the knitted conductive fabric has an intrinsic flexibility, capable of following the movements of the human body without the need, as currently done,

of copper foils glued over flexible materials to create electrical devices in wearable applications. Knitting the electrical components layout also has the advantage to avoid the use of glue or other attachment procedures which would affect the electrical characteristic of the device. The homogeneus, and fully integrated knitted component, has the important characteristic of being easy to fabricate by standard clothing machines, avoiding the layering process currently in use for the electro-textiles components.

The wearable strain sensor that we describe in the next section is composed of a folded dipole antenna, equipped with an inductively coupled RFID tag [109, 114]. The folded dipole topology has been motivated by the need of having an input impedance such that the RFID tag impedance $Z_c = 25 - j\,200\ \Omega$ can be complex conjugated. As opposed to conventional microchips, the two small pads of the package do not require physical soldering to the antenna arms, as the energy is inductively transferred through an internal matching circuit. The advantage of this inductively coupled RFID technology is in maintaining the full flexibility of the fabric, even around the microchip area. Furthermore, under sufficiently large mechanical deformations, the RSSI variation will be enhanced by the decoupling between the microchip and the antennas arms.

5.2 Inductively Coupled RFID Tag

One of the major challenges of smart textiles is the integration of lumped components, which require physical connection with the conductive textile element. In the literature we can find several approaches that attempt to address this challenge [115]. However, the use of conductive epoxy and other solid compounds tend to stiffen the structure and degrade the electrical performance.

We have addressed this limitation by utilizing a novel approach. As an RFID tag for the wearable strain sensor, we selected the Murata MAGICSTRAP, a 2-port IC tag employing inductive-coupling technology [116]. Specifically, the two small pads of the SMD components allow coupling of the RF energy to the two antenna's arms, avoiding the need for physical soldering. The component can be easily integrated into textiles by knitting a small pocket between the two antenna's arms, thus maintaining the full flexibility and comfort of the resulting garment. Furthermore, this choice allows for enhancing the strain sensitivity to physical deformation, as joint variations of input impedance and RF decoupling are significantly higher than radiation pattern changes alone [108]. In other words, by using the proposed RFID tag, the physical deformation of the antenna, causes impedance variations and coupling reduction between the IC and the antenna, yielding significant variations of the backscattered power (RSSI).

For the above reasons, we selected the MAGICSTRAP model LMXS31ACNA-011, a small 3.2 x 1.6 mm SMD IC with input impedance equal to $Z_c = 25\ j\,200\ \Omega$ within the 870 915 MHz bandwidth. In Table 5.1, we summarize the main features of the RFID tag. The SMD package includes a standard EPC global Class1Gen2 integrated circuit, along with a matching unit that allows the inductive-coupling of energy between the components pads and the knitted antenna. When considering the practical washability of the final garment, the component can sustain up to 150 °C for two hours, which makes it suitable for standard laundry processes. The high ESD (ElectroStatic Discharge) protection function makes it safe and compatible for wearable applications.

Table 5.1 Murata MAGICSTRAP IC Characteristics

Input Impedance	$Z_c = 25\ j\ 200\ \Omega$
Frequency	870 915 MHz
Dimension	3.2 x 1.6 x 0.55 mm
EPC Memory	240 bits
User Memory	512 bits
TID Memory	64 bits

5.3 Flexible RFID Strain Sensor Using Inductively Coupled RFID Tag

The proposed folded dipole antenna was specifically designed for use as a wireless strain sensor within the 860-960 MHz UHF region. In order to guarantee a flexible and robust support for the measurements, we employed polyethylene foam substrate having 30 mm of thickness, while the antenna metallization was printed on a thin copper tape and applied on top of the substrate.

5.3.1 Experimental Dielectric Characterization

For the sake of accurate design and simulation of the overall radiating element, the substrate dielectric characteristics have been measured with an Agilent 85070 E Dielectric Probe Kit along with N5230A Network Analyzer. This measurement is based on the estimation of the dielectric constant, or complex permittivity $k^* = \epsilon_r^* = \epsilon_r - j\epsilon'_r$, as well as the parameter $\text{Tan}(\delta) = \epsilon_r / \epsilon'_r$. While the former describes the interaction of the material with an electric field, the latter expresses relative loss of the material.

A calibrated probe was placed in contact with the polyethylene foam, measuring the complex permittivity k^* and the $\text{Tan}(\delta)$ parameters through a software running on the Network Analyzer. Fig. 5.1 shows the dielectric results of the polyethylene substrate compared

to the air characteristics. Similar to air, the polyethylene imaginary part ϵ'_r is practically negligible, resulting in a Tan(δ) approximately equal to zero. Thus, the dielectric constant of the substrate is equivalent to the solely real part of the complex permittivity $k^* = \epsilon_r^* = \epsilon_r$ and the measured value is about $\epsilon_r = 1.45$, within the whole frequency bandwidth.

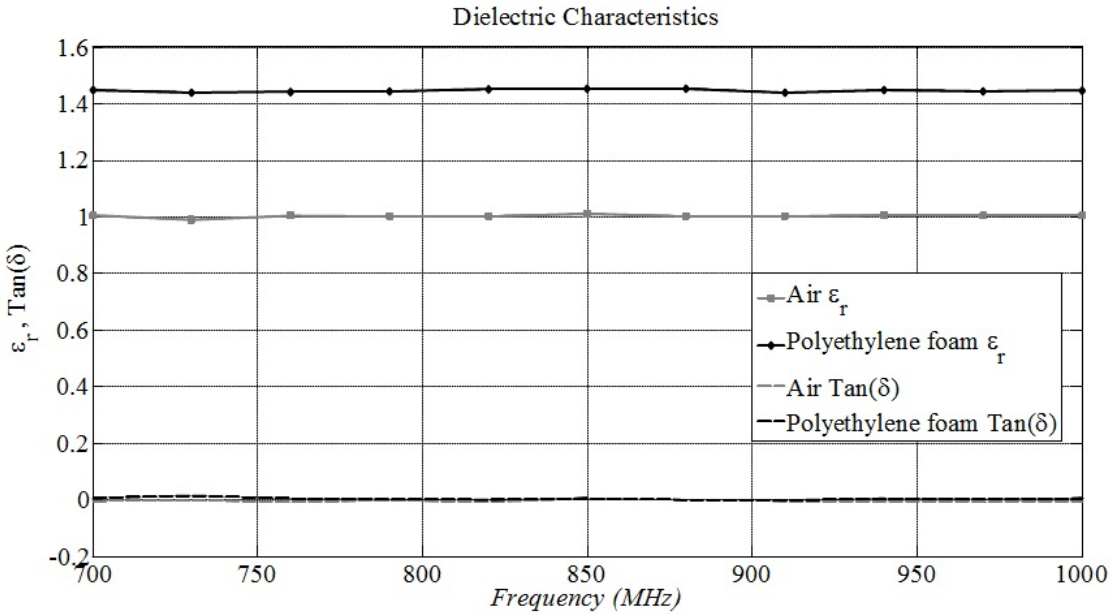

Figure 5.1 Dielectric characterization of the polyethylene substrate, compared with the standard air characteristics.

5.3.2 Folded Dipole Antenna Design

The flexible tag antenna has been designed for use with a the novel inductively coupled RFID microchip, MAGICSTRAP, which doesn't require any soldering process since the pads are inductively coupled to the antenna metallization. This choice was motivated by the need of enhancing the tag's sensitivity to physical deformations, as variations of the input impedance are significantly higher than radiation pattern changes alone [108]. Thus, by using the proposed RFID microchips, the physical deformation of the tag causes impedance variations and coupling reduction between the microchip and the antenna, yielding signifi-

cant variations of the backscattered power (RSSI).

Typically, the input impedance of RFID tags $Z_c = R_c + j\ X_c$ does not match with the 50 Ω standard which characterize the majority of front-end antennas. Due to the non-zero reactance X_c, antennas for RFID tags are properly designed for complex conjugate matching with these unconventional impedances. For the case of the MAGICSTRAP RFID tag, the input impedance is characterized by a resistance R_c = 25 Ω and a reactance of X_c = - 200 Ω. Because of this negative value of X_c, the folded dipole antenna topology was selected to exhibit inductive reactance for complex conjugate matching and thus maximum energy delivery between the microchip and the antenna. For the following realization of the wearable strain sensor, the folded dipole antenna has two major characteristics that align with system requirements:

- First, the loop structure in the knitting process allows us to achieve positive reactance for proper complex conjugate matching with the RFID tag
- Second, the simple planar layout makes the folded dipole architecture suitable for conventional knitting machines while allowing alignment of the conductive thread along the direction of maximum current flow.

Fig. 5.2 shows the 3D model of the proposed antenna, where the actual metallization layer is sitting on top of the polyethylene substrate. The layout has been designed and simulated using the High Frequency Structure Simulator (HFSS). The design is made by a folded dipole, with a thin long slot, which plays the role of tuning the center frequency of the impedance matching. The outer dimension of the proposed antenna is W = 9.5 mm and L = 124 mm, while the internal slot length is 77 mm and the width is equal to 3 mm. The

gap between the two dipole arms has been designed to have a length of 1 mm, accounting for the distance between the RFID microchip pads.

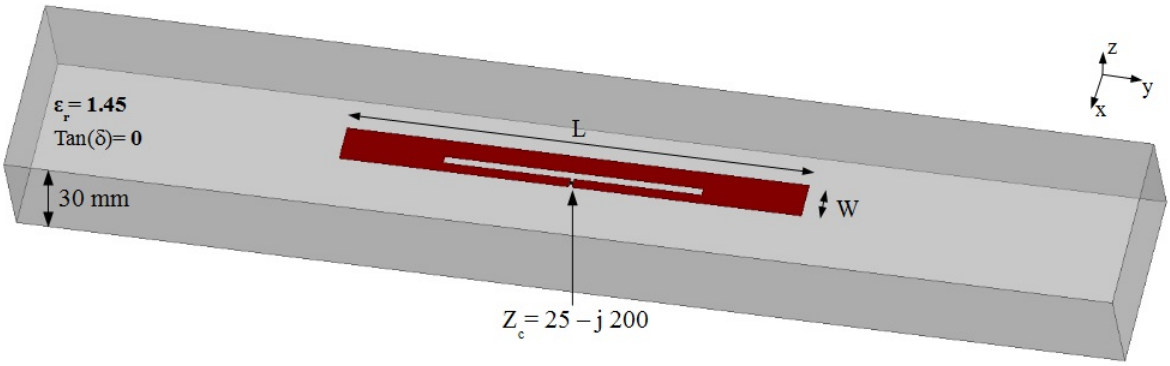

Figure 5.2 3D HFSS model of the folded dipole antenna. The substrate characteristic was defined based on the dielectric measurements, while the metallization was assumed copper. The lumped port used as excitation was set accordingly to the microchip impedance Z_c = 25 - *j* 200 Ω.

Once the antenna was properly tuned to approach the ideal complex conjugate matching at 870 MHz, the reflection coefficient S_{11}, between the antenna and the microchip, was estimated from the simulated input impedance Z_a, according to the following numerical expression [117]:

$$S_{11} = 20 \log_{10} \left(1 - \frac{4 R_a R_c}{|Z_a + Z_c|^2} \right) \tag{5.1}$$

where $Z_a = R_a + j\, X_a$ and $Z_c = R_c + j\, X_c$ is the simulated antenna input impedance and the microchip characteristic impedance, respectively.

In Fig. 5.3, we show the real and imaginary part of the complex antenna input impedance. At the desired center frequency of 870 MHz the impedance is equal to Z_a = 25.4 + *j* 201.8 Ω. Fig. 5.4 depicts the resulting return loss (S_{11}) computed using 5.1. The 10 dB return loss bandwidth is 50 MHz, covering with good impedance matching from 850 to 900 MHz.

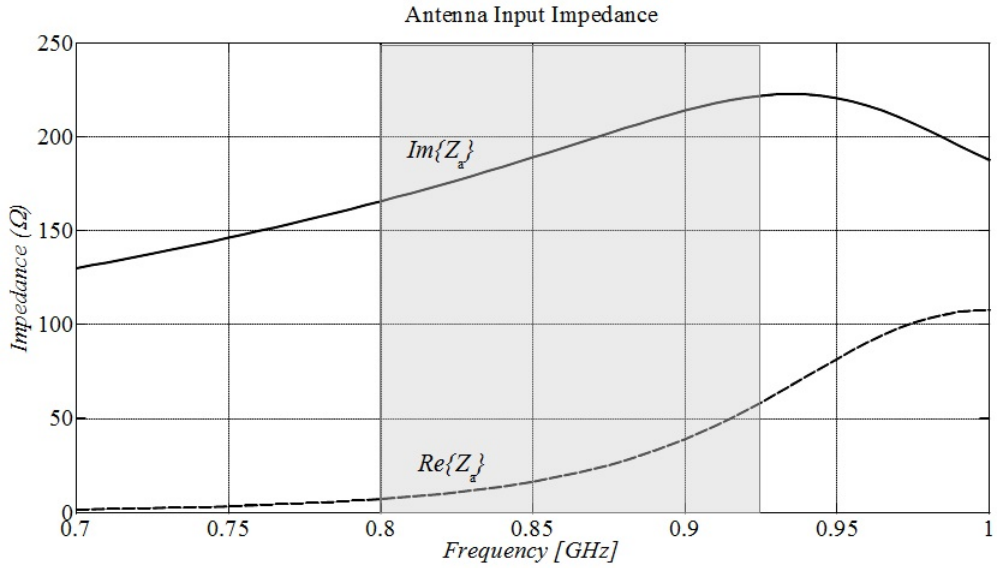

Figure 5.3 Simulated folded dipole antenna input impedance Z_a.

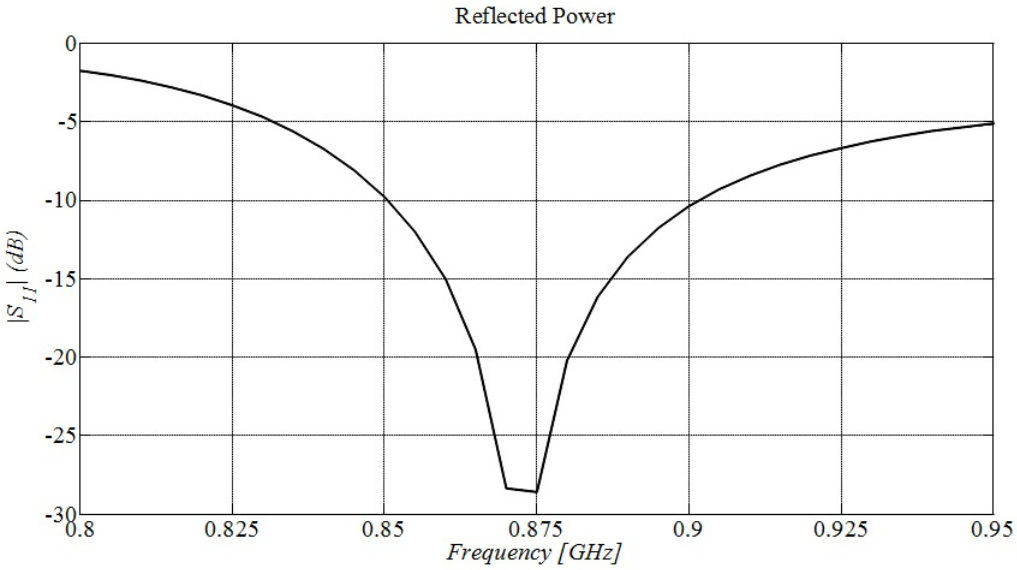

Figure 5.4 Numerical estimation of the reflection coefficient S_{11} within the highlighted bandwidth above, from 800 to 960 MHz.

In terms of radiation characteristics, the proposed antenna radiates a uniform omnidirectional beam in the plane normal to the excitation port (*x*-*z*, elevation cut) with 2.4 dBi of peak gain. Fig. 5.5 shows azimuth (*x*-*y*) and elevation (*x*-*z*) cuts of the omnidirectional

beam, according to the coordinate system shown in the inset of Fig. 5.2.

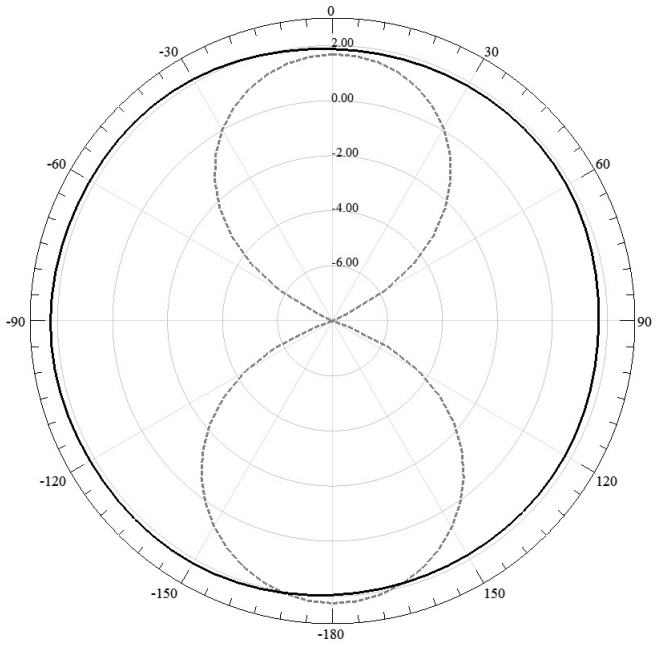

Figure 5.5 Radiation characteristic of the folded dipole antenna. The pattern resemble the typical dipole omnidirectional pattern, with uniform radiation around the plane normal to the feed port (*x*-*z*).

5.3.3 Impedance Measurements Setup and Experimental Results

The proposed folded dipole antenna has been printed on a copper tape and integrated on top of the polyethylene substrate for experimental validation. The folded dipole topology is characterized by having balanced input impedance, which doesn't allow for conventional S-parameter characterization using the unbalanced ports of a network analyzer. However, the impedance can still be determined by using a proper test fixture that considers the antenna as a two-port network. The measured two-port complex S-parameters are post-processed to compute the antenna impedance Z_a using the following expression [118]:

$$Z_a = R_a + jX_a = 2Z_0 \frac{(1 - S_{11}^2 + S_{21}^2 - 2S_{12})}{(1 - S_{11})^2 - S_{21}^2} \tag{5.2}$$

where Z_0 is the network analyzer characteristic impedance 50 Ω. Since the antenna can reasonably be assumed to be symmetrically balanced, in 5.2 we assume $S_{11} = S_{22}$ and $S_{12} = S_{21}$. Once the complex impedance Z_a has been extracted, the return loss, S_{11}, can finally be determined using 5.1. For this experiment, the test fixture was made by two 90 mm semi-rigid coaxial cables terminated by SMA connectors at one end. The two cables were aligned together by soldering the outer shields and the central conductors of the second ends were soldered on the antenna feed port. Prior port extension of the network analyzer was performed for de-embedding the test fixture length.

Fig. 5.6 shows the result of the complex input impedance measurement. At the desired center frequency of 870 MHz the impedance is equal to $Z_a = 27 + j\ 196\ \Omega$, which results in a good conjugate matching with Zc. The relative return loss in Fig. 5.7 exhibits a 10 dB bandwidth of about 200 MHz.

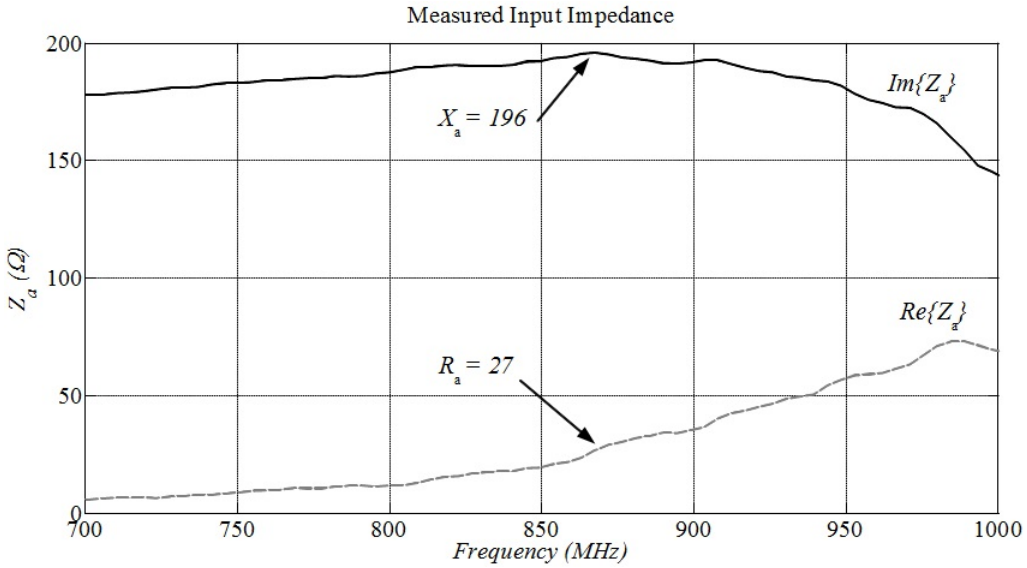

Figure 5.6 Measured input impedance through the test fixture.

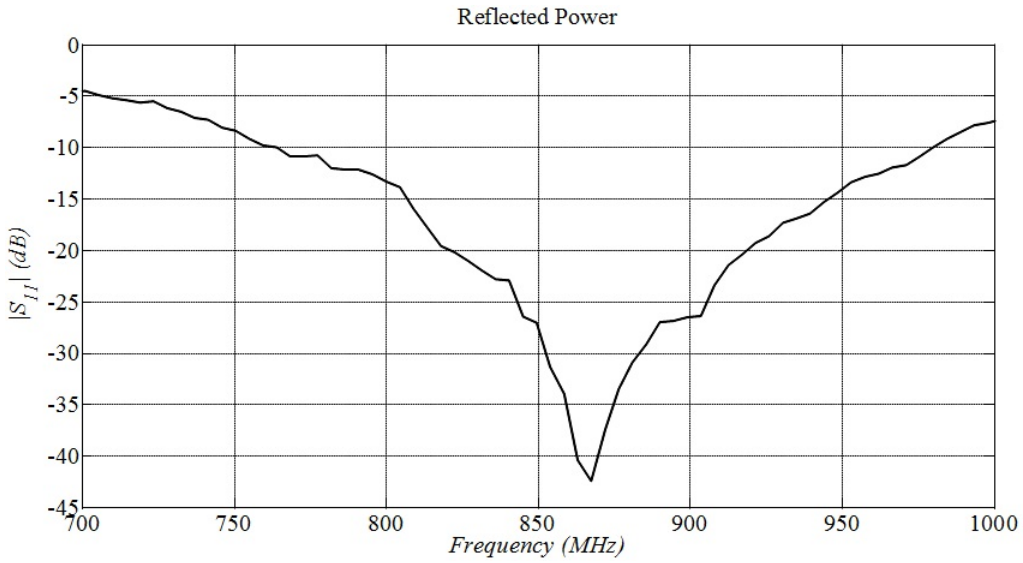

Figure 5.7 Numerical estimation of the return loss, S_{11}.

5.3.4 Strain Sensitivity Experimental Analysis

The flexible tag antenna was employed for radial strain measurements within an anechoic chamber facility. As shown in Fig. 5.8, the experimental setup comprises the manufactured tag antenna placed 1.6 m apart from a commercial Impinj Speedway RFID reader [12]. The antenna was progressively bent from the rest position $\alpha = 0°$ to the maximum angle of $\alpha = 30°$. For each angle, the reader interrogated the tag antenna collecting a total of 300 samples of backscattered RSSI values, recorded for following statistical analysis.

In Table 5.2, the results are summarized along with the relative RSSI percentage variation between the different angular deformations. With respect to the rest position, the difference in backscattered power was appreciable for angles above $\alpha = 10°$. On the other hand, when the deformation was greater than $\alpha = 30°$ the RSSI values fell below the reader sensitivity as a result of the larger impedance changing and increased decoupling between

the antenna and the microchip.

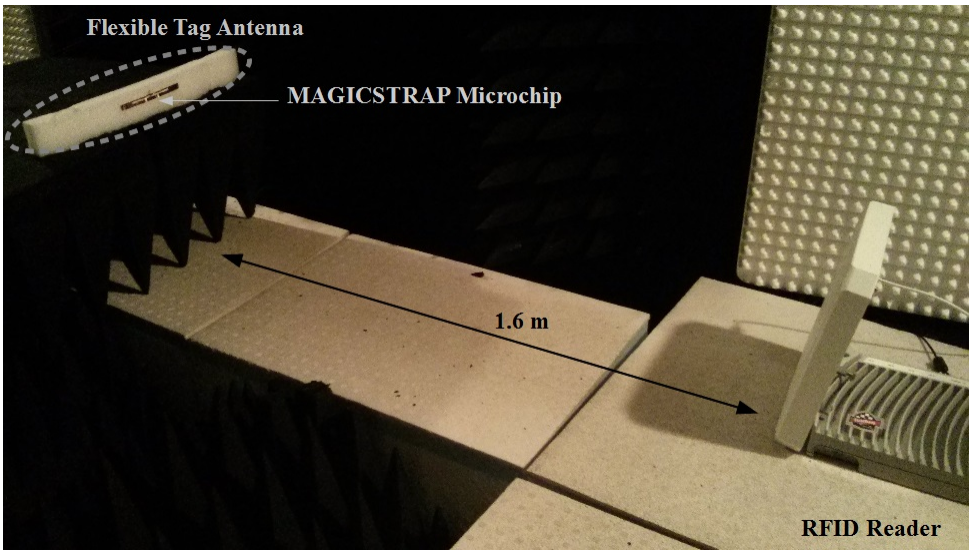

Figure 5.8 RSSI measurement setup within the anechoic chamber.

Table 5.2 RSSI Measurement Results

Angle (°)	Average RSSI (dBm) [a]	Variation (%)
$\alpha = 0°$	-61	-
$\alpha = 12°$	-63	3.3
$\alpha = 23°$	-69	13.1
$\alpha = 26°$	-73	19.7

[a] Three independent tests for each angle, 100 samples each. Maximum variance in single test $\sigma = 0.9$. Maximum Mean Square error between groups MS = 0.54.

5.4 Knitted RFID Strain Sensor

5.4.1 Experimental Material Characterization

The strain sensing application of the proposed knitted RFID tag requires a high degree of flexibility under mechanical deformation. For the non-conductive part of the garment, we employed a mix of wool and lycra, which maintains the planar antenna architecture while ensuring high elasticity. The conductive layout was knitted with high conductive silver-coated yarns. As a substrate support for non-human body based laboratory measurements,

we used a 55 mm thick polyethylene foam having dielectric constant close to the air's value as shown in Section 5.1.

For accurate simulations of the antenna design, we characterized the non-conductive fabric as well as the foam support through an Agilent 85070E Dielectric Probe Kit connected to a N5230A Vector Network Analyzer. Table 5.3 summarizes the measured characteristics. The dielectric constant of the foam approximates the unitary value of the air, whereas the non-conductive textile is slightly higher. For both materials, the loss tangent is relatively low.

Table 5.3 Supporting Material Characterization

Material	ϵ_r	Tan(δ)
Polyethylene Foam	1.2	0.01
Mix of Woll and Lycra	1.5	0.03

For knitting the conductive layout, we selected a 99 % pure silver plated nylon yarn having linear resistance equal to 50 Ω/m and 27 % of maximum elongation. When a conductive yarn is used, the finite conductivity of the planar structure is determined by the yarn's linear resistance and knitting method. As the contact area between the conductive loops increases, the equivalent resistance of the fabric decreases. Furthermore, the conductivity is highly dependent on the direction of the current flow in the textile, knitting geometry and loop density [115]. To ensure good conductivity of the overall design, the loops forming the antenna are tightly knitted, even when the fabric is in a relaxed state. Furthermore, the conductive threads have been aligned along the direction of maximum current flow in order to minimize the conduction losses. The following antenna layout selection and optimization takes into account the aforementioned factors as well as the

practical manufacturability using conventional knitting machines for industrial production.

5.4.2 Knitted Antenna Design

When designing knitted or embroidered conductive structures, the layout cannot be modeled or assumed as a pure conductive sheet. In our case, we can define knitting as the process of creating fabric with yarns by forming a series of interconnected loops. As suggested in [119], these structures exhibit higher electrical length compared to corresponding ideal copper sheets. For these reasons, the conductive layout should be modeled by a sheet impedance Z_s comprising resistive and imaginary parts, expresses by Ω/sq. While the resistance accounts for the ohmic losses, the imaginary part contributes to the antenna input impedance due to the electrotextile knitted loops.

The antenna was built on the folded dipole layout discussed in Section 5.3.2 and simulated with the High Frequency Structure Simulator HFSS. The design is a folded dipole with a thin slot whose width and length act as the main tuning parameters for impedance matching at 870 MHz. The complex sheet impedance was determined through a series of parametric simulations and comparison with a measured prototype. The optimal sheet resistance and reactance values are Z_s = 0.2 - j 2.6 Ω/sq. Fig. 5.9 shows the 3D antenna model for numerical simulations where the antenna layout is placed on top of the supporting polyethylene substrate. The outer dimension of the proposed antenna is W_{total} = 7.5 mm and L_{total} = 88 mm, while the internal slot length is W_{slot}= 1.5 mm and L_{slot} = 68 mm.

Once the antenna impedance was properly tuned for the best complex conjugate matching at 870 MHz, the return loss S_{11} was calculated from the simulated input impedance Z_a according to 5.1, where $Z_a = R_a + j\,X_a$ and $Z_c = R_c + j\,X_c$ is the simulated knitted antenna

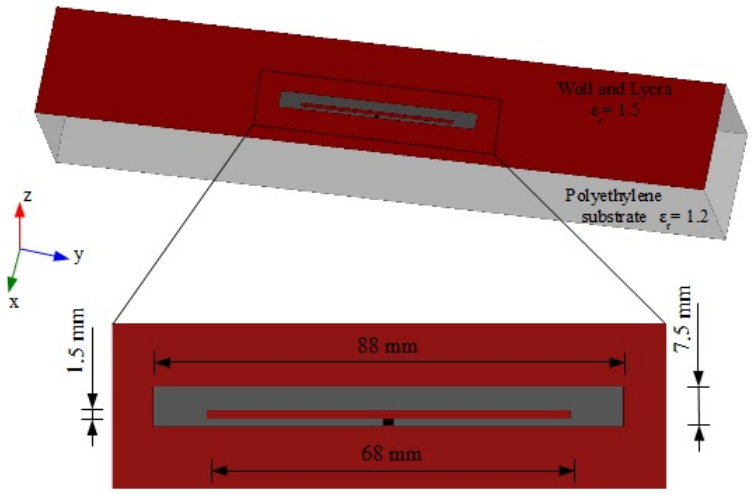

Figure 5.9 3D Simulation model of the proposed wearable RFID sensor. The substrate characteristics were defined based on the dielectric measurements reported in Table 5.3. As an RF excitation, a lumped port was set according to the RFID tag impedance Z_c = 25 - j 200 Ω.

input impedance and the MAGICSTRAP RFID tag characteristic impedance given in Table 5.1, respectively. The equation editor in HFSS allows for a convenient real time plotting of this custom S_{11} quantity.

In Fig. 5.10 we show the simulation of the antenna's input impedance Z_a. At the desired center frequency of 870 MHz, the complex impedance is equal to Z_a = 57.1 + j 180.2 Ω. The return loss S_{11}, computed with 5.1, is depicted in Fig. 5.11 for the same frequency sweep. The 10 dB return loss bandwidth is about 70 MHz, covering, with good impedance matching, the frequency band from 850 to 920 MHz.

The radiation characteristic resembles the same omnidirectional beam as a conventional dipole radiator. As shown in Fig. 5.12(a), the maximum current intensity occurs along the two major edges, while it reaches lower intensity along the short edges. The resulting beam will, therefore, be characterized by a uniform radiation around the plane normal to the feed

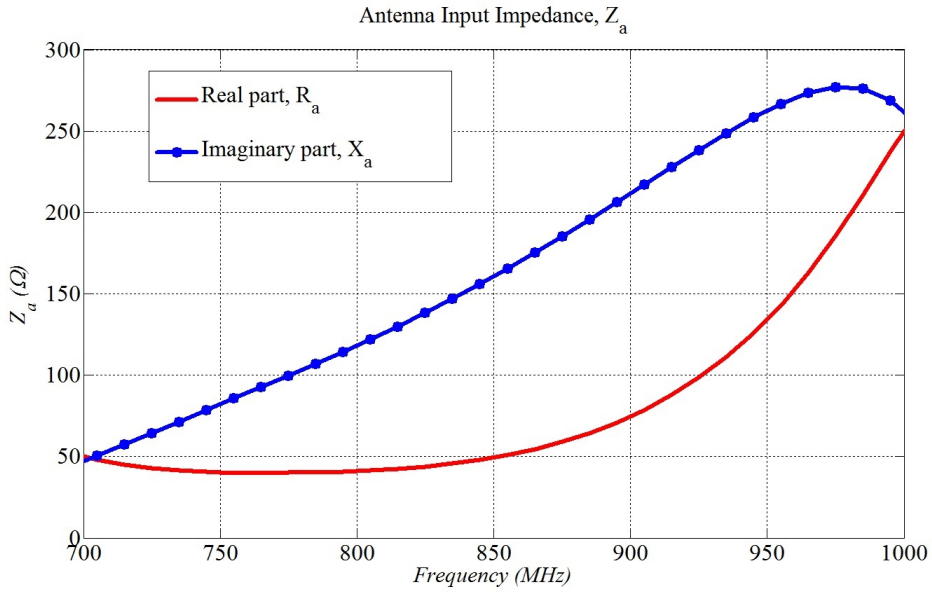

Figure 5.10 Simulated complex input impedance of the textile folded dipole antenna.

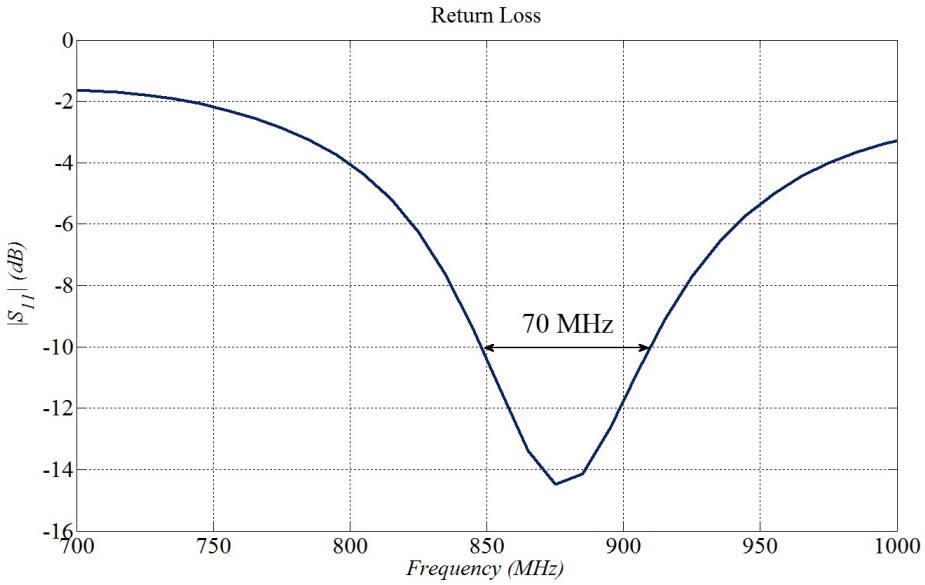

Figure 5.11 Numerical estimation of the return loss S_{11} using 5.1. The antenna layout has been optimized to yield good impedance matching within the whole frequency range of the RFID tag: 870 - 915 MHz.

port (x-z plane), and two nulls along the major axis (y-z plane). In Fig. 5.12(a) and (b) and we show the 3D beam with respect to the antenna layout along with the detailed 2D

azimuth and elevation patterns. The maximum gain is about 0.8 dBi, which is lower with respect to a copper-based design, due to the textile complex sheet impedance.

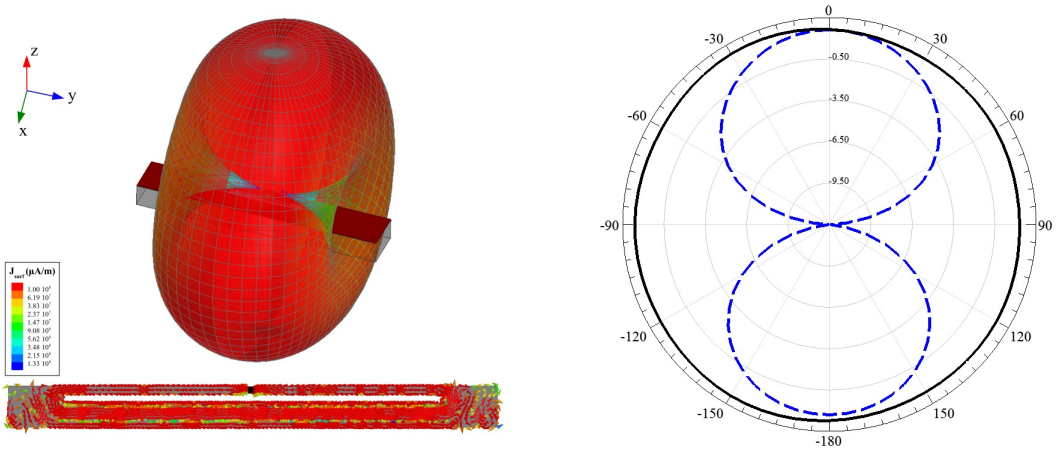

(a) (b)

Figure 5.12 Simulated current distribution and radiation characteristics. (a) The highest density of current distribution flows along the major axis, generating an omnidirectional beam normal to the y axis. (b) 2D radiation pattern for both azimuth (x-y plane, dashed line) and elevation plane (x-z plane, solid line).

When designing knitted antennas, the transition between the theoretical model to the actual prototype requires some empirical iterations. While the theoretical dimensions are given in the metric system, the CAD software used for knitting machines defines the layout in terms of the number of yarns and loops. Once the desired knitted folded dipole antenna was manufactured, its input impedance and radiation pattern have been characterized and compared to the expected numerical results.

5.4.3 Input Impedance Experimental Results

As previously mentioned, the topology of folded dipole antennas is characterized by balanced input impedance, while the conventional coaxial lines are balanced (quasi-TEM). This characteristic does not allow for conventional scattering parameters (S-parameters)

characterization using the coaxial ports of a network analyzer. However, the antenna's input impedance can still be determined through a differential approach, with a proper coaxial fixture that considers the antenna to be a two-port network. Fig. 5.13 shows the experiment setup with a network analyzer and two-port fixture along with the prototype of the knitted folded dipole antenna.

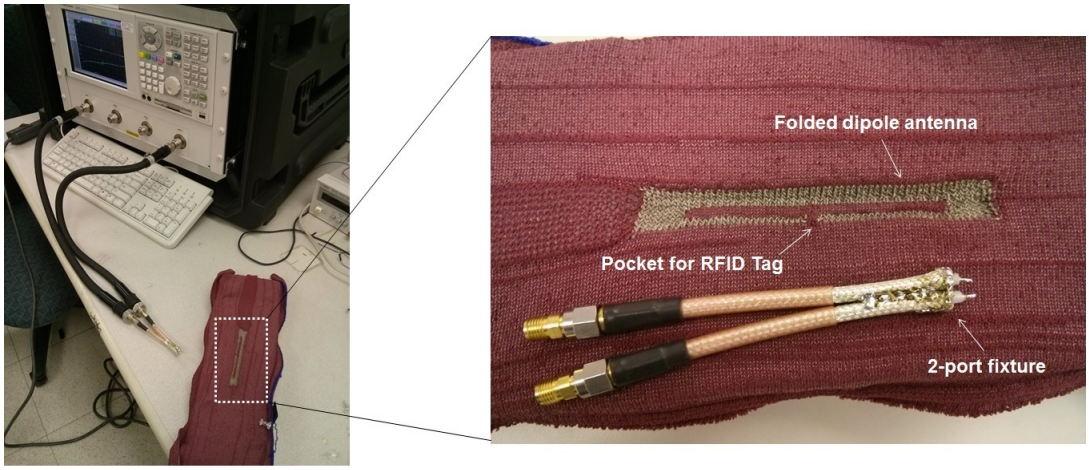

a

Figure 5.13 Experiment setup of S-parameter measurements. (a) Network analyzer connected to the two-port fixture. (b) Knitted dipole antenna prototype with location of the pocket for RFID tag housing and detail of the two-port fixture for balanced impedance measurements.

[a]Textile antennas manufactured at the Drexel Shima Seiki Haute Technology Laboratory.

In these measurements, the fixture was made by two $\lambda/4$ semi-rigid coaxial cables terminated with SMA connectors at one end. The two cables were aligned together by soldering the outer shields and the central conductors were connected to the knitted antenna by using conductive epoxy. The network analyzer was properly calibrated and the fixture's length was de-embedded through the port-extension function. The measured two-port complex S-parameters were loaded into MATLAB for computing the antenna impedance Z_a

through 5.2, where Z_0 is the 50 Ω characteristic impedance of the network analyzer. The knitted antenna can reasonably be assumed to be symmetrically balanced, therefore in 5.2 we still assume $S_{11} = S_{22}$ and $S_{12} = S_{21}$. After determining the antenna's impedance Z_a, the return loss S_{11} can be calculated using 5.1.

In Fig. 5.14 the measurements show that at the desired center frequency of 870 MHz, the impedance is equal to $Z_a = 49.5 + j\ 205.0\ \Omega$, which yields a good conjugate matching with the RFID tag impedance Z_c. The respective return loss in Fig. 5.15 exhibits a 10 dB bandwidth of 100 MHz, covering the desired frequency range. Through comparison with the simulated return loss, we notice that the measurement returns a larger 10 dB bandwidth. This is potentially due to the lower quality factor of the manufactured knitted radiator, which tends to be more lossy, and in turn it yields a larger bandwidth.

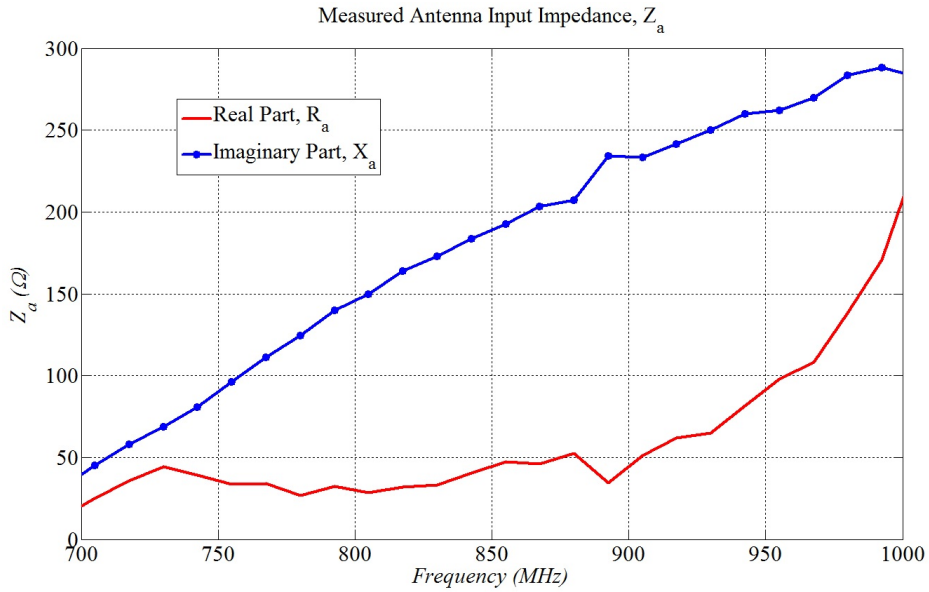

Figure 5.14 Measured complex input impedance of the knitted folded dipole ntenna, using the differential measurement approach.

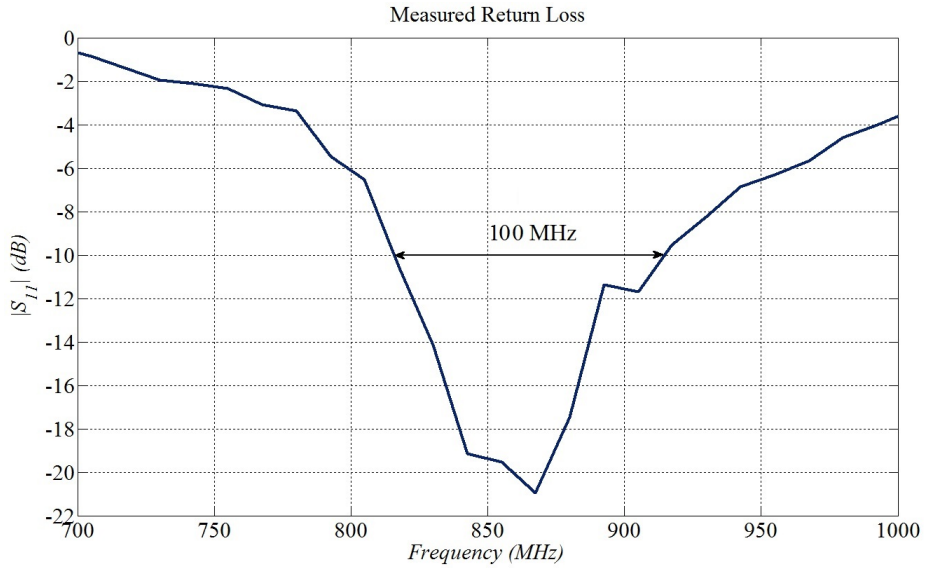

Figure 5.15 Measured return loss S_{11}, extracted using 5.1. The 10 dB return loss bandwidth is 100 MHz.

5.4.4 Radiation Pattern Experimental Results

Evaluating the directivity of the knitted antenna allows us to infer the current distribution occurring along the conductive threads. To this end, the knitted folded dipole prototype, equipped with the MAGICSTRAP RFID tag, and an Impinj Speedway reader [12], were set 70 cm apart within an anechoic chamber. The antenna was attached to a 3D manipulator for azimuth and elevation plane rotations. The rotations occurred in steps of 5°, and 200 RFID packets were averaged for each angular step.

Fig. 5.16 shows the anechoic chamber setup along with the resulting azimuth and elevation cuts. The knitted folded dipole antenna offers the desired omnidirectional radiation in the azimuth plane, and the two nulls in the azimuth plane correspond to the location of the antenna's short edges. This is in good agreement with the predicted radiation characteristics of Fig. 5.12. The high conductive thread density along the longer edges allows us

to support the expected current flow and generation of the desired radiation pattern.

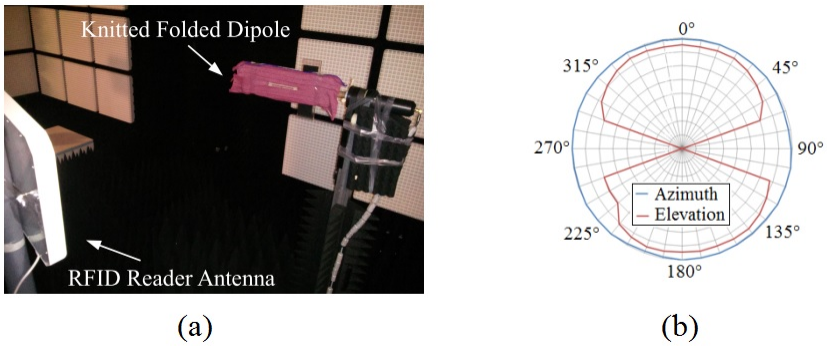

(a) (b)

Figure 5.16 Anechoic chamber setup for radiation pattern measurements. (a) Directional antenna connected to Impinj Speedway reader [12]. (b) Knitted folded dipole antenna with MAGICSTRAP tag inserted within the knitted pocket.

5.4.5 Effects of the Human Body Proximity

The wearable RFID strain sensor discussed above aims to determine human functions such as breathing and contraction patterns or determine the points of an injury. However, the human body interacts with the radiated field of the antenna due to the absorption of radiation between tissue layers. This interaction tends to load the antenna, leading to a shift of the resonant frequency, as well as degradation of the radiation pattern and efficiency. In order to evaluate this effect, and thus properly compensate the antenna design, we have performed a numerical simulation to simulate the antenna at different heights from the human body [120]. Specifically, by addressing the application of a fetal well-being monitor, we simulated the antenna for incremental separations above a human stomach to determine the best placement of the sensor.

The human stomach model was created with four different layers: skin, fat, muscle, and intestines [121]. Fig. 5.17 illustrates the structure of the human stomach. The skin layer had a thickness of 2 mm, the fat layer had a thickness of 5 mm, the muscle layer

had a thickness of 10 mm, and the intestines layer was extended to the bottom of the simulation boundary. The antenna can operate within the 800-900 MHz RFID band, as a result the layer properties were defined with dielectric constants and densities measured at 900 MHz [122]. The layer properties are displayed in Table 5.4, and were loaded into the HFSS model. The skin, muscle, and intestine layers have a high relative permittivity and conductivity. This is due to the large water content that exists in these tissue layers. As a result, these layers have a greater impact on the antenna's performance than the fat layer.

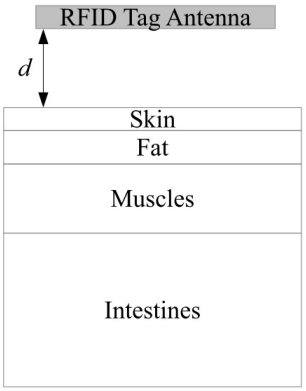

Figure 5.17 Sketch of the human body stomach model used for simulations.

Table 5.4 Human Stomach Layer Properties

Human Stomach Layer	ϵ_r	Conductivity (S/m)	Density (Kg/m^3)
Skin	41.40	0.87	1100
Fat	5.50	0.05	916
Muscle	56.90	1.00	1041
Intestines	55.00	1.05	1000

A parametric simulation was run to observe the loading effects at different heights d above the human stomach model, shown in Fig. 5.17. The antenna was first placed at skin level, then progressively separated in steps of d = 5 mm. By looking at Fig. 5.18, we can observe the effect of the human body on the antennas input impedance. By assuming

operations at 870 MHz, the S_{11} falls below the -6 dB threshold when the distance is between 5 mm $< d <$ 10 mm. However, the optimal S_{11} regime under -10 dB is achieved when $d >$ 45 mm. This analysis allows for optimizing the original antenna design by considering the aforementioned loading effects. In fact, by matching the antenna 30 - 40 MHz above the desired center frequency, we can guarantee optimal impedance matching under wearable applications.

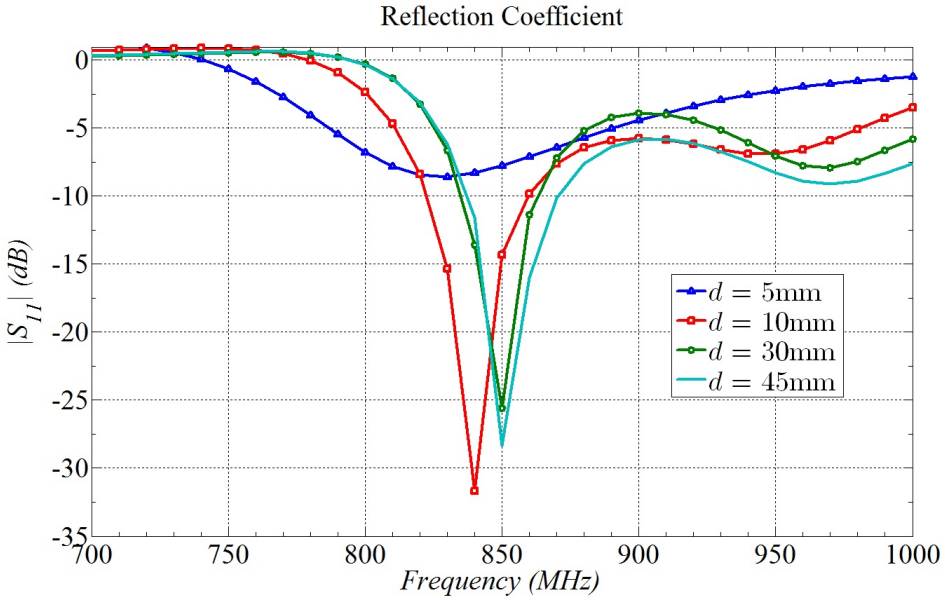

Figure 5.18 Return loss S_{11} of the RFID tag antenna for different distances d from the human stomach model.

The envelope of the radiation pattern changed significantly in proximity of the human body. Due to reflections and absorptions of the tissue layers, the radiation pattern is directed broadside, normal to the human body model. As shown in Fig. 5.19, when the antenna is kept very close to the human stomach, the loading effect is such that the antenna efficiency degrades, causing negative gains. On the other hand, when the height d is increased, the efficiency improves and the antenna radiates with positive gains. Specifically, when $d >$ 10 mm the gain returns to have positive values, up to 4.7 dBi. Even though the

radiation pattern remains directional, the Half-Power Beamwidth (HPBW) is comparable to the omnidirectional beam showed in Fig. 5.16.

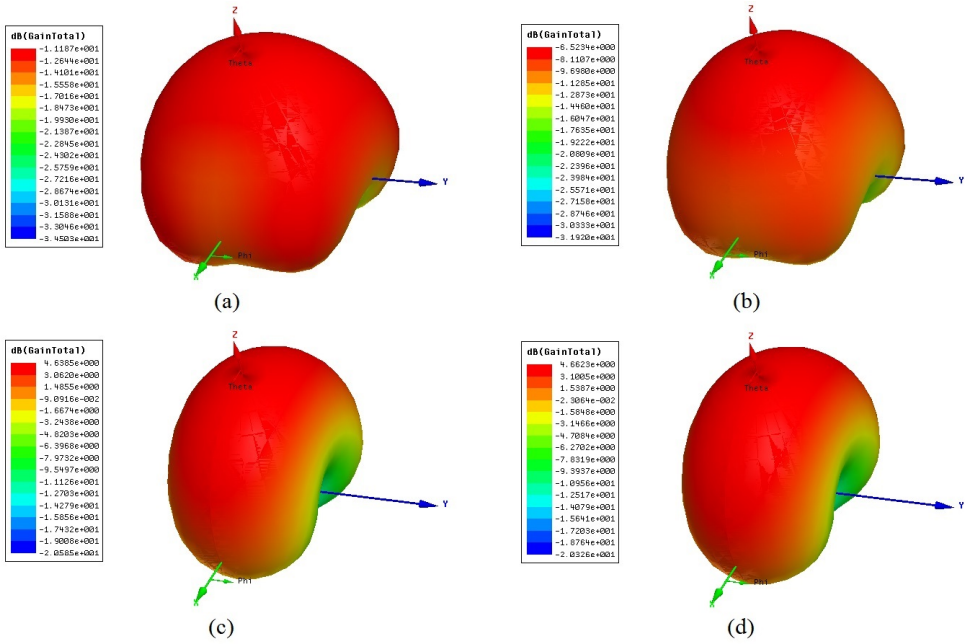

Figure 5.19 Radiation patterns as function of the heights d above the human stomach, at the frequency of 870 MHz. (a) d = 5 mm, (b) d = 10 mm, (c) d = 30 mm, (c) d = 45 mm. Under low distance the gains are negative, while when d is increased, the gains are about 60 % higher than without human stomach.

5.5 Application as a Biomedical Contractions Sensor

Since the aim of this sensor is to capture contractions or other physical deformations in the presence of a human body, we have performed a preliminary strain sensing analysis using a peristaltic pump to periodically inflate and deflate a balloon inside the stomach of a pregnancy mannequin. As a benchmark, we used a commercial Philips 50 xm tocodynamometer [123], which is a wired probe that measures pregnancy contractions. For interrogating the textile sensor, we employed an Impinj Speedway RFID reader [12] placed at about 1 m from the mannequin. The air balloon was inflated and deflated seven times over

a period of 140 seconds. As depicted in Fig. 5.20, the side-by-side simultaneous testing showed that the received RSSI variations are in good agreement with the output from the commercial tocodynamometer. This result enables the wearable RFID sensor to be used as a strain sensor for biomedical applications.

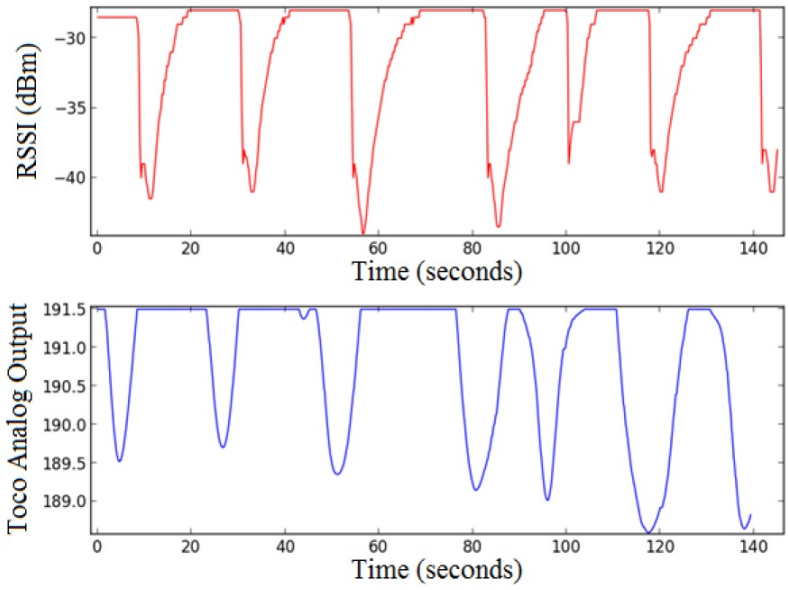

Figure 5.20 Performance comparison between the proposed wearable RFID sensor (red) and a commercial tocodynamometer (blue).

5.6 Application as a Baby Breathing Monitor

The Sudden Infant Death Syndrome (SIDS) is a sudden death of a child less than one year of age and it usually occurs during sleep. This death is unexplained, but the potential enviromental causes may be sleeping on the stomach or side, overheating, and exposure to cigarette smoke. Accidental suffocation, such as during bed sharing, may also be a cause of SIDS.

Monitoring if the child is breathing regularly can detect the aforementioned causes and prevent SIDS. Currently, the wearable baby monitors are made by a baby onesie equipped

with a WiFi or Bluetooth module that collects data from sensors integrated into the garment and sends the data to a mobile device [107]. However, these monitors employ active modules that are bulky and need to be recharged regularly. The wearable strain sensor that we have designed has the potential of improving this current technology, since it can be used to detect the breathing pattern of a child.

In order to evaluate the performance of the strain sensor for SIDS monitoring, we have used a mechanical baby mannequin which is used for medical training. This mannequin, called Laerdal SimBaby [124], can be programmed with specific breathing and non-breathing intervals and the chest of the baby resembles the usual expansion of a breathing pattern. The wearable strain sensor was fitted around the baby mannequin's chest, and the Impinj Speedway RFID reader [12] was placed at about 1 m from the mannequin. Five minutes of continuous data was collected from the programmable infant mannequin device as follows: breathing from 0 - 60 seconds, non-breathing from 60 - 100 seconds, breathing from 100 - 210 seconds, non-breathing from 210 - 240 seconds, breathing from 240 - 300 seconds. To remove noise and mitigate quantization, a Gaussian filter was applied to the RFID data collected. The algorithm considered for determining activity state is the Support Vector Machine [125]. This algorithm is a machine learning model that analyzes data and recognizes patterns used for classification analysis. This analysis separates the data points collected by the RFID interrogator into two classes: in this case, breathing and non-breathing classes. The data points are arranged into a 2D plot with standard deviation on the x-axis and RSSI mean on the y-axis. Because the mean and standard deviation were found to be highly separable, they plot in such a way that one or more separating "lines" can be drawn that separates most of the data points. The "best" such separating line is the

one that separates the groups of points and also maximizes the distance or margin between the line and the nearest data point from each class.

From the results shown in Fig. 5.21 we can see that the wearable strain sensor, along with the Support Vector Machine algorithm, allow a very clear separation of the breathing and non-breathing patterns. The few points that belong to the wrong region are errors due to the mannequin transitioning from breathing to non-breathing states, and vice versa. This result demonstrates that the wearable strain sensor can be effectively used for monitoring breathing activity and preventing the risk of SIDS.

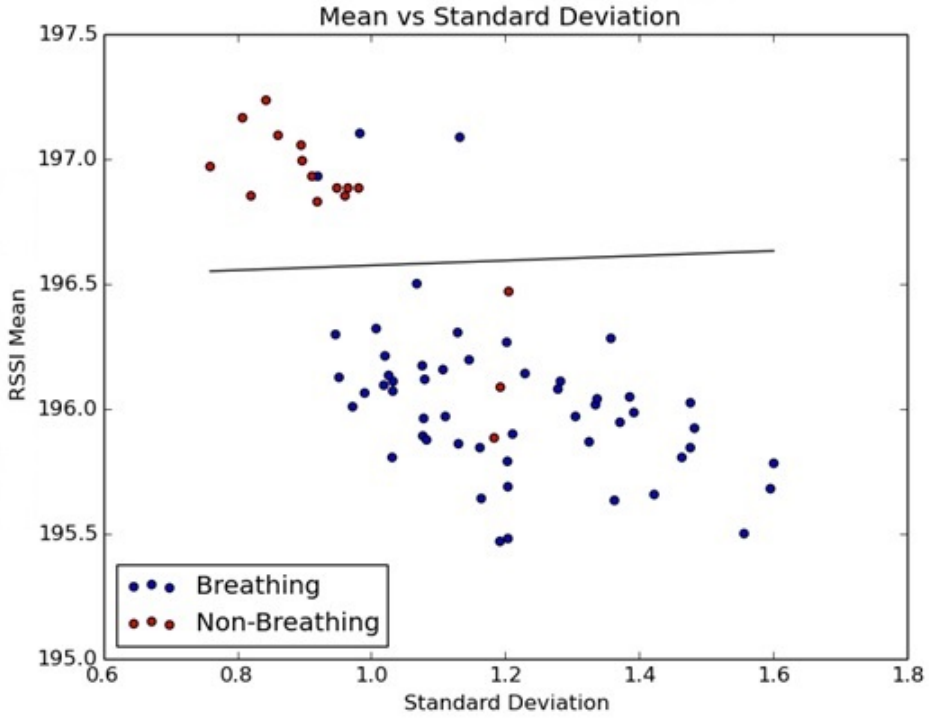

Figure 5.21 Plot of breathing and non-breathing patterns detected using the wearable strain sensor, along with the support vector machine algorithm.

5.7 Summary

In this section we have discussed the design and the experimental results of a knitted RFID strain sensor. It comprises a knitted folded dipole antenna with an inductively coupled RFID tag. This new approach is superior because it allows for an easier integration of RFID microchips into clothes, avoiding the need of physical connection between the antenna and the microchip's pads. Furthermore, if employed as a strain sensor, this approach maintains the full fabric elasticity and it enhances the backscattered power variations under physical stretch.

Preliminarily, we evaluated the strain sensing capability using a flexible copper based design. Next, after characterizing the textile materials used for manufacturing, we have designed and simulated the folded dipole antenna for the best impedance matching with the tags characteristic impedance. Due to the knitted pattern, we have modeled the conductive layout with complex sheet impedance, which reflects more closely the resistive loss and the reactive contribution of stiches and loops. The measurements with a two-port S-parameter fixture matched the numerical results. Further measurements in an anechoic chamber confirmed the desired omnidirectional radiation pattern of the knitted sensor.

Since the aim of this sensor is to capture contractions, respiration, or other physical deformations, we have performed a preliminary strain sensing analysis for pregnancy monitoring and baby breathing monitoring using programmable mannequins. An Impinj Speedway reader [12] was used to interrogate the knitted tag placed on the mannequins. By collecting and post-processing the RSSI data received from the sensor, the experiments have shown that the sensor can successfully detect contractions and respiration patterns. A side-

by-side comparison with commercial devices further confirmed the accuracy achievable with this new technology.

Chapter 6: Conclusions

The exponential growth in wireless data demand has driven new technological solutions to meet high performance requirements. In particular, the MIMO multi-antenna systems became an integral part of the modern wireless devices for enhancing the data throughput and maintaining a high quality of service. In order to further improve the robustness of the wireless link and the channel capacity, reconfigurable antennas provide additional capacity to the MIMO systems. These antennas allow for a smart control of the energy radiated from each antenna, which can be adaptively changed through ad-hoc algorithms running within the wireless device. As opposed to conventional antennas which radiate a static beam around unnecessary directions, reconfigurable antennas allow for change to their radiation pattern toward a specific wireless user or toward the best multipath direction. Moreover, in addition to enhancing the channel capacity and link robustness, reconfigurable antennas significantly reduce the interference between adjacent wireless networks.

The integration of reconfigurable antennas within commercial wireless devices is currently limited by the large dimension and higher manufacturing costs. In this dissertation we have proposed two novel designs that address these limitations: i) Reconfigurable Alford Loop Antenna, which can generate a single omnidirectional pattern and switchable directional patterns in a single planar design, ii) miniaturized metamaterial leaky-wave antenna with large beamsteering capabilities. The former design is characterized by planar layout and reduced number of components for a more cost effective integration within

commercial WiFi routers. Whereas, the latter design is significant because it represents the first beam steering antenna that can be integrated within mobile devices, such as laptop computers and tablets.

In Chapter 3, we showed the design and characteristics of the Reconfigurable Alford Loop Antenna. In addition to having compact and low cost features, the aim of this reconfigurable antenna is to radiate omnidirectional and directional beams in order to maintain high link robustness under different multiple or single client network scenarios. The design is composed of four pairs of microstrip elements, disposed symmetrically on both layers of a standard FR-4 substrate. Two sets of PIN diodes allow the control of the different antenna states. In order to exploit this new antenna architecture with the current wireless standards, we have shown three different designs: *i)* Ultra wideband design for communications at 3.6 GHz. *ii)* WiFi and WiMAX design for the 2.4 and 3 GHz bands. *iii)* Two multiband designs for the newest 802.11 ac standard, which uses 2.4 and 5 GHz bands. We demonstrated that this new antenna architecture can be used for a single wideband communication system or over multiple separate bands by using lumped filters.

To effectively integrate this antenna within commercial routers or software-defined radios, we have designed two switching circuits that provide external control to the different antenna states. The first circuit is made by MOSFETs and a passive network for standard wired control through GPIOs, whereas, in the second approach we used phototransistors for designing a fully optical switching circuit. According to the results obtained within the anechoic chamber, we have shown that the optical circuitry prevents the distortion of the directivity of each radiation pattern caused by the conventional wired controls. We also evaluated the level of intermodulation distortions that may be generated by the PIN diodes.

The numerical analysis has shown that in both omnidirectional and directional states, the quality of the signal at the antenna's input port is not affected by the non-linearity of the PIN diodes. Finally, the experimental results conducted on a 2x2 RALA array showed high level of pattern diversity, which can be leveraged for improving the wireless link on MIMO systems.

In Chapter 4, we have shown the design and characterization of a miniaturized reconfigurable leaky-wave antenna. The size reduction has been accomplished through the etch of complementary split-ring resonators underneath each unit cell. This defected ground structure acts as a loading element that reduces the resonant frequency of the top layer radiating layout. The experimental results demonstrated that this miniturization technique can be successfully applied to metamaterial antennas, maintaining good impedance matching and radiation performance. In this work, we have performed an extensive numerical and experimental analysis of the miniaturized unit cell centered at 2.45 GHz. The unit cell has shown good impedance matching and a relatively large sweep of the dispersion curve, which leads to large beam steering angles. With respect to an equivalent conventional leaky-wave antenna, the miniaturized design achieved in this work is 47 % smaller but with equal beam steering coverage of 120 °. According to the results obtained in this work, the leaky-wave antenna etched with complementary split-ring resonators enables the development of miniaturized beam steering antennas that do not require expensive and bulky substrates. This architecture enables the integration of small beamsteering antennas within portable devices for improving the wireless connectivity.

In Chapter 5, this thesis discussed the application of frequency reconfigurable antennas and RFID technology for the development of a wireless, wearable sensor. The aim of

the project is to design a knitted passive sensor for monitoring respirators and contractions wirelessly. The unique feature of this work is the development of knitted antennas embedded in the host garment and equipped with inductively coupled RFID tags for backscatter power sensing. Through the use of commercially available RFID readers, the wearable RFID sensor responds to mechanical deformations with backscattered power variations. The successive filtering and analysis of this data provide information about the respiration or contraction patterns that need to be monitored. To design the wearable RFID sensor, we took the following steps: *i)* design of a preliminary copper based folded dipole antenna equipped with an inductively coupled RFID tag, *ii)* strain sensitivity evaluation through a commercial RFID reader, *iii)* re-design of a textile version of the sensor, accounting for the complex sheet impedance which is a non-ideal effect due to knitted conductive loops and yarns, *iv)* experimental analysis of input impedance and radiating performance, *v)* strain sensitivity analysis through programmable medical mannequins and performance comparison with commercial devices. According to the results of this work, we demonstrated that fully knitted antennas equipped with inductively coupled RFID tags provide good strain sensing performance to be used as wireless sensors for monitoring biomedical parameters, such as contraction or respiration patterns.

The technical focus of this Ph.D. dissertation was enhanced with an analysis of the commercialization reconfigurable antenna technologies in Appendix A. By considering that a large number of the antenna technologies are conceived within research laboratories, we have analyzed the three major modes of external technology commercialization: *i)* licensing, *ii)* spin-off, and *iii)* joint-venture. Central to the analysis of each mode are benefits and costs from both the academic and the industrial perspectives, with examples from the

antenna technology field. This work was extended through a survey of the companies that are currently commercializing reconfigurable antennas in the U.S. and Europe. In terms of technology application, the U.S. companies exploited reconfigurable antennas for diverse applications such as, mobile, satellite communications, vehicular and WLAN, whereas, European companies seem to converge on traditional WiFi or mobile applications. However, one of these companies is also commercializing a reconfigurable antenna for enhancing the reading reliability of RFID systems. As a result of this analysis we can infer potential new applications where the reconfigurable antenna technology has not been exploited yet.

Based on the results discussed in this dissertation, there are three new potential applications and improvements that could be undertaken:

Reconfigurable Antennas for Wireless Charging Transmitters: The ability to harvest energy from surrounding wireless networks or dedicated devices, is currently being used for charging low-power devices wirelessly [126]. This new technology enables the elimination of batteries and it can extend the operating life of electronic systems. However, the application of reconfigurable antennas has not been exploited yet. Based on the results discussed in this thesis, reconfigurable antennas can be used to further maximize the energy transferred between the power transmitter and the receiving device. By pointing the beam toward the specific device to be charged, the charging time may be significantly reduced and the energy transmitted more efficiently. Furthermore, the use of reconfigurable antennas for energy transfer and data throughput maximization may coexist within the same device. In fact, the development of new algorithms for the antenna state selection for both the throughput maximization and energy transfer, may extend the capabilities of the current WiFi access points.

Port Isolation Improvement on the Miniaturized Leaky-Wave Antenna: In Chapter 4, we have seen the design of a miniaturized leaky-wave antenna with large beam steering capabilities. This antenna has the potential to be integrated within mobile devices. However, the low RF isolation between the two input ports may represent a challenge for the use with 2x2 MIMO cards, which require high isolation between the two RF ports. In order to solve this limitation, two approaches may be investigated: *i)* By cascading additional metamaterial unit cells the isolation between the ports can be improved, and the higher energy leakage would lead to higher radiation pattern's gain and narrower half-power beamwidth. *ii)* The use of RF circulators or couplers for energy recycling is another approach that can solve the poor isolation on the miniaturized leaky-wave antenna. Similarly to [127], the use of an RF circulator or a coupler enhances the radiation efficiency of a leaky-wave antenna by feeding the energy remaining at the output port back into the input port. As a result, the current loops several times along the antenna until its energy has been fully radiated. Even though this approach renders the antenna single-port, the use of two single-port leaky-wave antennas placed back-to-back allows for full azimuth coverage and 2x2 MIMO operations.

Wearable Strain Sensor Through Textile Patch Antennas: Recently, it has been shown that RFID tags can be developed using textile technologies and patch antenna architectures [119]. The wearable strain sensor proposed in this dissertation may be improved by using a patch antenna architecture, which may extend the reading range of the wearable sensor and, potentially, increase the strain sensitivity under physical deformation. Another advantage of using patch antennas for wearable applications is the broadside radiation pattern, which concentrates the main beam away from the human body and it reduces the RF exposure.

Bibliography

[1] D. Piazza and K. Dandekar, "Reconfigurable antenna solution for MIMO-OFDM systems," *Electronics Letters*, vol. 42, no. 8, pp. 446–447, 2006.

[2] D. Piazza, P. Mookiah, M. D'Amico, and K. Dandekar, "Two port reconfigurable circular patch antenna for mimo systems," in *Antennas and Propagation, 2007. EuCAP 2007. The Second European Conference on*, Nov 2007, pp. 1–7.

[3] G.-M. Zhang, J. song Hong, and B.-Z. Wang, "A novel pattern reconfigurable wideband slot antenna using pin diodes," in *Microwave and Millimeter Wave Technology (ICMMT), 2010 International Conference on*, May 2010, pp. 22–24.

[4] M. Donelli, R. Azaro, L. Fimognari, and A. Massa, "A planar electronically reconfigurable wi-fi band antenna based on a parasitic microstrip structure," *Antennas and Wireless Propagation Letters, IEEE*, vol. 6, pp. 623–626, 2007.

[5] M. Facco and D. Piazza, "Reconfigurable zero-order loop antenna," in *Antennas and Propagation Society International Symposium (APSURSI), 2012 IEEE*, July 2012, pp. 1–2.

[6] B. Alshami, H. Aboulnour, and M. Dib, "Design of a broadband espar antenna," in *Microwave Symposium (MMS), 2009 Mediterrannean*, Nov 2009, pp. 1–6.

[7] M. Yamamoto, M. Taromaru, H. Sadamichi, and A. Shimizu, "Performance of angle switch diversity using espar antenna for mobile reception of terrestrial digital tv," in *Vehicular Technology Conference, 2006. VTC-2006 Fall. 2006 IEEE 64th*, Sept 2006, pp. 1–5.

[8] T. I. C. Caloz, *Electromagnetic metamaterials transmission line theory and application*. John Wiley and Sons, Inc., 2006.

[9] S. Lim, C. Caloz, and T. Itoh, "Metamaterial-based electronically controlled transmission-line structure as a novel leaky-wave antenna with tunable radiation angle and beamwidth," *Microwave Theory and Techniques, IEEE Transactions on*, vol. 53, no. 1, pp. 161–173, Jan 2005.

[10] D. Piazza, M. D'Amico, and K. Dandekar, "Two port reconfigurable CRLH leaky wave antenna with improved impedance matching and beam tuning," in *Antennas and Propagation, 2009. EuCAP 2009. 3rd European Conference on*. IEEE, 2009, pp. 2046–2049.

[11] A. G. K. A. Alford, "Ultra high-frequency loop antenna," *Institute of Electrical and Electronics Engineers, AIEE Transactions*, 1940.

[12] Impinj rfid readers. [Online]. Available: http://www.impinj.com/products/readers/

[13] J. Kountouriotis, D. Piazza, K. Dandekar, M. D'Amico, and C. Guardiani, "Performance analysis of a reconfigurable antenna system for mimo communications," in *Antennas and Propagation (EUCAP), Proceedings of the 5th European Conference on*. IEEE, 2011, pp. 543–547.

[14] A. Grau, H. Jafarkhani, and F. De Flaviis, "A reconfigurable multiple-input multiple-output communication system," *Wireless Communications, IEEE Transactions on*, vol. 7, no. 5, pp. 1719–1733, 2008.

[15] R. Bahl, N. Gulati, K. Dandekar, and D. Jaggard, "Impact of pattern reconfigurable antennas on interference alignment over measured channels," in *Globecom Workshops (GC Wkshps), 2012 IEEE*. IEEE, 2012, pp. 557–562.

[16] R. Wang, X. Wang, T. Chow, J. Burman, S. Zogg, F. Sakarya, and D. Jensen, "Capacity and performance analysis for adaptive multi-beam directional networking," in *Military Communications Conference, 2006. MILCOM 2006. IEEE*. IEEE, 2006, pp. 1–7.

[17] K. Wanuga, N. Gulati, H. Saarnisaari, and K. Dandekar, "Online learning for spectrum sensing and reconfigurable antenna control," in *Cognitive Radio Oriented Wireless Networks and Communications (CROWNCOM), 2014 9th International Conference on*, June 2014, pp. 508–513.

[18] P. Mookiah, J. Kountouriotis, R. Dorsey, B. Shishkin, and K. Dandekar, "Securing wireless links at the physical layer through reconfigurable antennas," in *Antennas and Propagation Society International Symposium (APSURSI), 2010 IEEE*. IEEE, 2010, pp. 1–4.

[19] N. Gulati, R. Greenstadt, K. Dandekar, and J. Walsh, "Gmm based semi-supervised learning for channel-based authentication scheme," in *Vehicular Technology Conference (VTC Fall), 2013 IEEE 78th*, Sept 2013, pp. 1–6.

[20] B. Cook, A. Shamim, and M. Tentzeris, "Passive low-cost inkjet-printed smart skin sensor for structural health monitoring," *Microwaves, Antennas Propagation, IET*, vol. 6, no. 14, pp. 1536–1541, 2012.

[21] C. A. Balanis, *Antenna Theory Analysis and Design*. John Wiley and Sons, Inc., 2005.

[22] P.-Y. Qin, A. Weily, Y. Guo, T. Bird, and C.-H. Liang, "Frequency reconfigurable quasi-yagi folded dipole antenna," *Antennas and Propagation, IEEE Transactions on*, vol. 58, no. 8, pp. 2742–2747, Aug 2010.

[23] Y. Zhou, R. Adve, and S. Hum, "Design and evaluation of pattern reconfigurable antennas for mimo applications," *Antennas and Propagation, IEEE Transactions on*, vol. 62, no. 3, pp. 1084–1092, March 2014.

[24] D. Piazza, P. Mookiah, M. D'Amico, and K. Dandekar, "Pattern and polarization reconfigurable circular patch for mimo systems," in *Antennas and Propagation, 2009. EuCAP 2009. 3rd European Conference on*, March 2009, pp. 1047–1051.

[25] D. Piazza, D. Michele, and K. Dandekar, "Two port reconfigurable crlh leaky wave antenna with improved impedance matching and beam tuning," in *Antennas and Propagation, 2009. EuCAP 2009. 3rd European Conference on*, March 2009, pp. 2046–2049.

[26] M. Kubo, X. Li, C. Kim, M. Hashimoto, B. Wiley, D. Ham, and G. M. Whitesides, "Stretchable microfluidic electric circuit applied for radio frequency antenna," in *Electronic Components and Technology Conference (ECTC), 2011 IEEE 61st*, May 2011, pp. 1582–1587.

[27] Q. Liu and P. Hall, "Varactor-loaded left handed loop antenna with reconfigurable radiation patterns," in *Antennas and Propagation Society International Symposium, 2009. APSURSI '09. IEEE*, June 2009, pp. 1–4.

[28] D. V. Thiel, "Switched parasitic antennas and controlled reactance parasitic antennas: a systems comparison," in *Antennas and Propagation Society International Symposium, 2004. IEEE*, vol. 3, June 2004, pp. 3211–3214 Vol.3.

[29] ——, "Impedance variations in controlled reactance parasitic antennas," in *Antennas and Propagation Society International Symposium, 2005 IEEE*, vol. 3A, July 2005, pp. 671–674.

[30] R. Ibernon-Fernandez, J. Molina-Garcia-Pardo, and L. Juan-Llacer, "Comparison between measurements and simulations of conventional and distributed mimo system," *Antennas and Wireless Propagation Letters, IEEE*, vol. 7, pp. 546–549, 2008.

[31] A. Z. A. Sibille, C. Oestges, *MIMO From Theory to Implementation*. Academic Press, 2011.

[32] M. Sawahashi, Y. Kishiyama, A. Morimoto, D. Nishikawa, and M. Tanno, "Coordinated multipoint transmission/reception techniques for lte-advanced [coordinated and distributed mimo]," *Wireless Communications, IEEE*, vol. 17, no. 3, pp. 26–34, June 2010.

[33] E. Perahia and R. Stacey, *Next Generation Wireless LANs: 802.11 n and 802.11 ac*. Cambridge university press, 2013.

[34] A. F. Molisch, *Wireless Communications*. John Wiley and Sons, Inc., 2005.

[35] A. Goldsmith, *Wireless Communications*. Cambridge university press, 2005.

[36] N. Gulati and K. Dandekar, "Learning state selection for reconfigurable antennas: A multi-armed bandit approach," *Antennas and Propagation, IEEE Transactions on*, vol. 62, no. 3, pp. 1027–1038, 2014.

[37] D. Piazza, M. D'Amico, and K. Dandekar, "Performance improvement of a wide-band MIMO system by using two-port RLWA," *Antennas and Wireless Propagation Letters, IEEE*, vol. 8, pp. 830–834, 2009.

[38] D. Piazza, N. Kirsch, A. Forenza, R. Heath, and K. Dandekar, "Design and evaluation of a reconfigurable antenna array for MIMO systems," *Antennas and Propagation, IEEE Transactions on*, vol. 56, no. 3, pp. 869–881, 2008.

[39] D. Patron, A. Daryoush, and K. Dandekar, "Optical control of reconfigurable antennas and application to a novel pattern-reconfigurable planar design," *Lightwave Technology, Journal of*, vol. 32, no. 20, pp. 3394–3402, Oct 2014.

[40] Q. Liu and P. Hall, "Varactor-loaded left handed loop antenna with reconfigurable radiation patterns," in *Antennas and Propagation Society International Symposium, 2009. APSURSI '09. IEEE*, June 2009, pp. 1–4.

[41] D. V. Thiel, "Switched parasitic antennas and controlled reactance parasitic antennas: a systems comparison," in *Antennas and Propagation Society International Symposium, 2004. IEEE*, vol. 3, June 2004, pp. 3211–3214 Vol.3.

[42] ——, "Impedance variations in controlled reactance parasitic antennas," in *Antennas and Propagation Society International Symposium, 2005 IEEE*, vol. 3A, July 2005, pp. 671–674 vol. 3A.

[43] S. Lim, C. Caloz, and T. Itoh, "Electronically-controlled metamaterial-based transmission line as a continuous-scanning leaky-wave antenna," in *Microwave Symposium Digest, 2004 IEEE MTT-S International*, vol. 1, June 2004, pp. 313–316 Vol.1.

[44] C.-M. Nieh and J. Lin, "Adaptive beam-steering antenna for improved coverage of non-contact vital sign radar detection," in *Microwave Symposium (IMS), 2014 IEEE MTT-S International*, June 2014, pp. 1–3.

[45] C. W. Jung, M.-J. Lee, G. Li, and F. De Flaviis, "Reconfigurable scan-beam single-arm spiral antenna integrated with rf-mems switches," *Antennas and Propagation, IEEE Transactions on*, vol. 54, no. 2, pp. 455–463, Feb 2006.

[46] Z. Jiang and F. Yang, "Reconfigurable sensing antennas integrated with thermal switches for wireless temperature monitoring," *Antennas and Wireless Propagation Letters, IEEE*, vol. 12, pp. 914–917, 2013.

[47] M. Islam and M. Ali, "Body-wearable beam steering antenna array for 5.2 ghz wlan applications," in *Electrical Computer Engineering (ICECE), 2012 7th International Conference on*, Dec 2012, pp. 447–449.

[48] D. Patron, K. Dandekar, and A. Daryoush, "Optical control of pattern-reconfigurable planar antennas," in *Microwave Photonics (MWP), 2013 International Topical Meeting on*, Oct 2013, pp. 33–36.

[49] A. Daryoush, K. Bontzos, and P. Herczfeld, "Optically tuned patch antenna for phased array applications," in *Antennas and Propagation Society International Symposium, 1986*, vol. 24, June 1986, pp. 361–364.

[50] Z. Jiang and F. Yang, "Reconfigurable sensing antennas integrated with thermal switches for wireless temperature monitoring," *Antennas and Wireless Propagation Letters, IEEE*, vol. 12, pp. 914–917, 2013.

[51] J. Luther, S. Ebadi, and X. Gong, "A low-cost 2 x 2 planar array of three-element microstrip electrically steerable parasitic array radiator (espar) subcells," *Microwave Theory and Techniques, IEEE Transactions on*, vol. 62, no. 10, pp. 2325–2336, Oct 2014.

[52] Y.-Y. Bai, S. Xiao, C. Liu, X. Shuai, and B.-Z. Wang, "Design of pattern reconfigurable antennas based on a two - element dipole array model," *Antennas and Propagation, IEEE Transactions on*, vol. 61, no. 9, pp. 4867–4871, Sept 2013.

[53] J. Luther, S. Ebadi, and X. Gong, "Electrically-steerable parasitic array radiator (espar) antenna design for arrays with two and three parasitically-coupled elements," in *Radio and Wireless Symposium (RWS), 2012 IEEE*, Jan 2012, pp. 79–82.

[54] D. Smith, J. Willie, D. C. Padilla, S. Vier, and S. Nemat-Nasser, Schultz, "Composite medium with simultaneously negative permeability and permittivity," *Physical Review Letters*, vol. 84, no. 18, pp. 4184–4187, May 2000.

[55] A. Grbic and G. Eleftheriades, "A backward-wave antenna based on negative refractive index l-c networks," in *Antennas and Propagation Society International Symposium, 2002. IEEE*, vol. 4, 2002, pp. 340–343 vol.4.

[56] A. Oliner, "A planar negative-refractive-index medium without resonant elements," in *Microwave Symposium Digest, 2003 IEEE MTT-S International*, vol. 1, June 2003, pp. 191–194 vol.1.

[57] C. Caloz and T. Itoh, "Application of the transmission line theory of left-handed (lh) materials to the realization of a microstrip "lh line"," in *Antennas and Propagation Society International Symposium, 2002. IEEE*, vol. 2, 2002, pp. 412–415 vol.2.

[58] ——, "Novel microwave devices and structures based on the transmission line approach of meta-materials," in *Microwave Symposium Digest, 2003 IEEE MTT-S International*, vol. 1, June 2003, pp. 195–198 vol.1.

[59] D. Piazza, P. Mookiah, M. D'Amico, and K. Dandekar, "Two port reconfigurable circular patch antenna for MIMO systems," in *Antennas and Propagation, 2007. EuCAP 2007. The Second European Conference on*. IET, 2007, pp. 1–7.

[60] C. Jiang, X.-W. Dai, and Y.-C. Jiao, "A novel compact horizontally polarized omnidirectional antenna," in *Signals Systems and Electronics (ISSSE), 2010 International Symposium on*, vol. 1, Sept 2010, pp. 1–3.

[61] F. Jolani, Y. Yu, and Z. Chen, "A broadband e-plane omnidirectional antenna for 4g lte applications with mimo," in *Antennas and Propagation Society International Symposium (APSURSI), 2012 IEEE*, July 2012, pp. 1–2.

[62] Skyworks smp-1345 *"Technical Data Sheet."*. [Online]. Available: http://www.skyworksinc.com/uploads/documents/200046M.pdf

[63] Ansoft hfss user manual. [Online]. Available: http://www.ansoft.com/

[64] D. Patron, D. Piazza, and K. Dandekar, "Wideband planar antenna with reconfigurable omnidirectional and directional radiation patterns," *Electronics Letters*, vol. 49, no. 8, pp. 516–518, April 2013.

[65] D. Patron and K. Dandekar, "Planar reconfigurable antenna with integrated switching control circuitry," in *Antennas and Propagation (EuCAP), 2014 8th European Conference on*, April 2014, pp. 2737–2740.

[66] S. Blanch, J. Romeu, and I. Corbella, "Exact representation of antenna system diversity performance from input parameter description," *Electronics Letters*, vol. 39, no. 9, pp. 705–707, May 2003.

[67] D. Patron, K. Dandekar, and D. Piazza, "A reconfigurable antenna with omnidirectional and directional patterns for mimo systems," in *Antennas and Propagation Society International Symposium (APSURSI), 2013 IEEE*, July 2013, pp. 204–205.

[68] G. D. Sworo, D. Patron, K. R. Dandekar, and M. Kam, "Characterization of pattern reconfigurable antenna arrays for mimo systems," in *Information Sciences and Systems (CISS), 2015 49th Annual Conference on*, March 2015, pp. 1–3.

[69] D. M. Pozar, *Microwave Engineering*. John Wiley and Sons, Inc., 2005.

[70] D. Patron, A. Daryoush, K. Dandekar, and D. Piazza, "Design and harmonic balance analysis of a wideband planar antenna having reconfigurable omnidirectional and directional patterns," in *Wireless and Microwave Technology Conference (WAMICON), 2013 IEEE 14th Annual*, April 2013, pp. 1–5.

[71] Skyworks, design with pin diodes, application note. [Online]. Available: http://www.skyworksinc.com/

[72] Y. Tawk, A. Albrecht, S. Hemmady, G. Balakrishnan, and C. Christodoulou, "Optically pumped frequency reconfigurable antenna design," *Antennas and Wireless Propagation Letters, IEEE*, vol. 9, pp. 280–283, 2010.

[73] Y. Tawk, S. Hemmady, C. Christodoulou, J. Costantine, and G. Balakrishnan, "A cognitive radio antenna design based on optically pumped reconfigurable antenna system (opras)," in *Antennas and Propagation (APSURSI), 2011 IEEE International Symposium on*, July 2011, pp. 1116–1119.

[74] G. Jin, D. Zhang, and R. Li, "Optically controlled reconfigurable antenna for cognitive radio applications," *Electronics Letters*, vol. 47, no. 17, pp. 948–950, August 2011.

[75] C. Panagamuwa, A. Chauraya, and J. Vardaxoglou, "Frequency and beam reconfigurable antenna using photoconducting switches," *Antennas and Propagation, IEEE Transactions on*, vol. 54, no. 2, pp. 449–454, Feb 2006.

[76] Everlight pt19-21b *"Technical Data Sheet."*. [Online]. Available: http://www.everlight.com/datasheets/PT19-21B-L41-TR8_datasheet.pdf

[77] Emscan, rfxpert. [Online]. Available: http://www.emscan.com/

[78] Y. J. Y. W. S. Kang, J. A. Park, "Simple reconfigurable antenna with radiation pattern," *Electronics Letters*, vol. 44, no. 3, pp. 182–183, 2008.

[79] C. P. [18] T. Abouful, A. Alomainy, "Reconfiguring uwb monopole antenna for conitive radio applications using gaas fet switches," *Antennas and Wireless Propagation Letters*, vol. 11, pp. 392–394, 2012.

[80] Netgear white paper *"Why Choose Simultaneus Dual Band?"*. [Online]. Available: http://www.netgear.com/landing/dual-band.aspx

[81] D. Patron, , D. Piazza, and K. Dandekar, "On the use of lumped filters for designing dual-band planar antennas with omnidirectional and directional radiation patterns," in *Wireless and Microwave Technology Conference (WAMICON), 2015 IEEE 16th Annual*, April 2015.

[82] M. Williams, D. Patron, and K. Dandekar, "Investigation of switching techniques for reconfigurable multiband planar antennas," in *Antennas and Propagation Society International Symposium (APSURSI), 2014 IEEE*, July 2014, pp. 1095–1096.

[83] Tdk diplexer dpx205950dt-9008a1 *"Technical Data Sheet."*. [Online]. Available: http://product.tdk.com/en/catalog/datasheets/rf_dpx_dpx205950dt-9008a1_en.pdf

[84] D. Patron and K. Dandekar, "A miniaturized reconfigurable crlh leaky-wave antenna using complementary split-ring resonators," *Transactions of Antennas and Propagation*, vol. under review, 2015.

[85] J. Kula, D. Psychoudakis, W.-J. Liao, C.-C. Chen, J. Volakis, and J. Halloran, "Patch-antenna miniaturization using recently available ceramic substrates," *Antennas and Propagation Magazine, IEEE*, vol. 48, no. 6, pp. 13–20, Dec 2006.

[86] P. Ikonen, K. Rozanov, A. Osipov, P. Alitalo, and S. Tretyakov, "Magnetodielectric substrates in antenna miniaturization: Potential and limitations," *Antennas and Propagation, IEEE Transactions on*, vol. 54, no. 11, pp. 3391–3399, Nov 2006.

[87] H. Mosallaei and K. Sarabandi, "Design and modeling of patch antenna printed on magneto-dielectric embedded-circuit metasubstrate," *Antennas and Propagation, IEEE Transactions on*, vol. 55, no. 1, pp. 45–52, Jan 2007.

[88] P. Mookiah and K. Dandekar, "Metamaterial-substrate antenna array for mimo communication system," *Antennas and Propagation, IEEE Transactions on*, vol. 57, no. 10, pp. 3283–3292, Oct 2009.

[89] D. Ahn, J.-S. Park, C.-S. Kim, J. Kim, Y. Qian, and T. Itoh, "A design of the low-pass filter using the novel microstrip defected ground structure," *Microwave Theory and Techniques, IEEE Transactions on*, vol. 49, no. 1, pp. 86–93, Jan 2001.

[90] A. Anand, A. Bansal, K. Shambavi, and Z. Alex, "Design and analysis of microstrip line with novel defected ground structure," in *Advanced Nanomaterials and Emerging Engineering Technologies (ICANMEET), 2013 International Conference on*, July 2013, pp. 670–673.

[91] Y. Xie, L. Li, C. Zhu, and C.-H. Liang, "A novel dual-band patch antenna with complementary split ring resonators embedded in the ground plane," *Progress In Electromagnetics Research Letters*, vol. 25, pp. 117–126, Aug 2011.

[92] M. Sharawi, M. Khan, A. Numan, and D. Aloi, "A csrr loaded mimo antenna system for ism band operation," *Antennas and Propagation, IEEE Transactions on*, vol. 61, no. 8, pp. 4265–4274, Aug 2013.

[93] H. Paaso, A. Mammela, D. Patron, and K. Dandekar, "Modified music algorithm for doa estimation using crlh leaky-wave antennas," in *Cognitive Radio Oriented Wireless Networks (CROWNCOM), 2013 8th International Conference on*, July 2013, pp. 166–171.

[94] H. Paaso, A. Mammela, D. Patron, and K. R. Dandekar, "Doa estimation through modified unitary music algorithm for crlh leaky-wave antennas," in *Personal Indoor and Mobile Radio Communications (PIMRC), 2013 IEEE 24th International Symposium on*, Sept 2013, pp. 311–315.

[95] A. Hakkarainen, J. Werner, N. Gulati, D. Patron, D. Pfeil, H. Paaso, A. Mammela, K. Dandekar, and M. Valkama, "Reconfigurable antenna based doa estimation and localization in cognitive radios: Low complexity algorithms and practical measurements," in *Cognitive Radio Oriented Wireless Networks and Communications (CROWNCOM), 2014 9th International Conference on*, June 2014, pp. 454–459.

[96] S. Wang, Q. Liu, and Z. Zhou, "A cooperative cognitive radio network using smart antenna," in *Communications Technology and Applications, 2009. ICCTA '09. IEEE International Conference on*, Oct 2009, pp. 450–456.

[97] J. Xie, Z. Fu, and H. Xian, "Spectrum sensing based on estimation of direction of arrival," in *Computational Problem-Solving (ICCP), 2010 International Conference on*, Dec 2010, pp. 39–42.

[98] E. Lee and A. Vinod, "A spatial and spectral detection approach for primary user interference mitigation in cognitive radios," in *General Assembly and Scientific Symposium, 2011 XXXth URSI*, Aug 2011, pp. 1–4.

[99] R. J. Weber, "Development of a cognitive array system," in *Masters Thesis, Montana State University*, 2010.

[100] D. Patron, H. Paaso, A. Mammela, D. Piazza, and K. Dandekar, "Improved design of a crlh leaky-wave antenna and its application for doa estimation," in *Antennas and Propagation in Wireless Communications (APWC), 2013 IEEE-APS Topical Conference on*, Sept 2013, pp. 1343–1346.

[101] Getting started with ansoft designer. [Online]. Available: http://www.ansoft.com/

[102] Infineon bb833 *"Technical Data Sheet."*. [Online]. Available: http://www.infineon.com/

[103] H. Nguyen, S. Abielmona, and C. Caloz, "Performance-enhanced and symmetric full-space scanning end-switched crlh lwa," *Antennas and Wireless Propagation Letters, IEEE*, vol. 10, pp. 709–712, 2011.

[104] A. Mehdipour, T. Denidni, and A.-R. Sebak, "Multi-band miniaturized antenna loaded by zor and csrr metamaterial structures with monopolar radiation pattern," *Antennas and Propagation, IEEE Transactions on*, vol. 62, no. 2, pp. 555–562, Feb 2014.

[105] K.-L. Wong and P.-J. Ma, "Small-size internal antenna for lte/wwan operation in the laptop computer," in *Applications of Electromagnetism and Student Innovation Competition Awards (AEM2C), 2010 International Conference on*, Aug 2010, pp. 152–156.

[106] Om signal. [Online]. Available: http://www.omsignal.com

[107] The mimo smart baby monitor. [Online]. Available: http://www.mimobaby.com

[108] C. Occhiuzzi, C. Paggi, and G. Marrocco, "Passive rfid strain-sensor based on meander-line antennas," *Antennas and Propagation, IEEE Transactions on*, vol. 59, no. 12, pp. 4836–4840, Dec 2011.

[109] D. Patron, T. Kurzweg, A. Fontecchio, G. Dion, and K. Dandekar, "Wireless strain sensor through a flexible tag antenna employing inductively-coupled rfid microchip," in *Wireless and Microwave Technology Conference (WAMICON), 2014 IEEE 15th Annual*, June 2014, pp. 1–3.

[110] D. Cottet, J. Grzyb, T. Kirstein, and G. Troster, "Electrical characterization of textile transmission lines," *Advanced Packaging, IEEE Transactions on*, vol. 26, no. 2, pp. 182–190, May 2003.

[111] D. Paul, M. Klemm, C. Railton, and J. McGeehan, "Textile boradband e-patch antenna at ism band," in *Antennas and Propagation for Body-Centric Wireless Communications, 2007 IET Seminar on*, April 2007, pp. 38–43.

[112] F. Declercq and H. Rogier, "Characterization of electromagnetic properties of textile materials for the use in wearable antennas," in *Antennas and Propagation Society International Symposium, 2009. APSURSI '09. IEEE*, June 2009, pp. 1–4.

[113] Y. Ouyang and W. Chappell, "High frequency properties of electro-textiles for wearable antenna applications," *Antennas and Propagation, IEEE Transactions on*, vol. 56, no. 2, pp. 381–389, Feb 2008.

[114] D. Patron, T. Kurzweg, A. Fontecchio, G. Dion, and K. Dandekar, "Wearable biomedical strain sensing via knitted antennas and inductively-coupled rfid tags," in *RFID, 9th annual IEEE International Conference on*, April 2015.

[115] I. Locher, M. Klemm, T. Kirstein, and G. Troster, "Design and characterization of purely textile patch antennas," *Advanced Packaging, IEEE Transactions on*, vol. 29, no. 4, pp. 777–788, Nov 2006.

[116] Murata magicstrap uhf tag. [Online]. Available: http://www.murata.com/en-us/campaign/ads/americas/rfid

[117] T. Koskinen and Y. Rahmat-Samii, "Metal-mountable microstrip rfid tag antenna for high impedance microchip," in *Antennas and Propagation, 2009. EuCAP 2009. 3rd European Conference on*, March 2009, pp. 2791–2795.

[118] X. Qing, C. K. Goh, and Z. N. Chen, "Impedance characterization of rfid tag antennas and application in tag co-design," *Microwave Theory and Techniques, IEEE Transactions on*, vol. 57, no. 5, pp. 1268–1274, May 2009.

[119] K. Koski, A. Vena, L. Sydanheimo, L. Ukkonen, and Y. Rahmat-Samii, "Design and implementation of electro-textile ground planes for wearable uhf rfid patch tag antennas," *Antennas and Wireless Propagation Letters, IEEE*, vol. 12, pp. 964–967, 2013.

[120] D. Patron, K. Gedin, T. Kurzweg, A. Fontecchio, G. Dion, and K. Dandekar, "A wearable rfid sensor and effects of human body proximity," in *Microwave and Antenna Sub-systems (BenMAS), 2014 Benjamin Franklin Symposium on*, September 2014.

[121] L. Roelens, W. Joseph, and L. Martens, "Characterization of the path loss near flat and layered biological tissue for narrowband wireless body area networks," in *Wearable and Implantable Body Sensor Networks, 2006. BSN 2006. International Workshop on*, April 2006, pp. 4 pp.–56.

[122] A. Christ, T. Samaras, A. Klingenbck, and N. Kster, "Characterization of the electromagnetic near-field absorption in layered biological tissue in the frequency range from 30mhz to 6,000mhz," in *Physics in Medicine and Biology*, Septemeber 2006, pp. 4951–4965.

[123] Philips 50 xm tocodynamometer *"Installation and Service Guide"*. [Online]. Available: http://www.frankshospitalworkshop.com/equipment/documents/ecg/service_manuals/Philips_M1350_-_Service_Manual.pdf

[124] Symbaby infant patient simulator. [Online]. Available: http://www.laerdal.com/us/SimBaby

[125] C. Cortes and V. Vapnik, "Support-vector networks," *Machine Learning*, vol. 20, no. 3, pp. 273–297, 1995. [Online]. Available: http://dx.doi.org/10.1007/BF00994018

[126] Powercast wireless power components and embedded modules.

[127] H. Nguyen, S. Abielmona, A. Parsa, and C. Caloz, "Novel power recycling schemes for enhanced radiation efficiency in leaky-wave antennas," in *Microwave Conference, 2009. APMC 2009. Asia Pacific*, Dec 2009, pp. 2006–2009.

[128] F. T. Rothaermel, S. D. Agung, and L. Jiang, "University entrepreneurship: a taxonomy of the literature," *Industrial and corporate change*, vol. 16, pp. 691–791, 2007.

[129] G. D. Markman, D. D. Siegel, and M. Wright, "Research and technology commercialization," *Journal of Management Studies*, vol. 45, pp. 1401–1423, 2008.

[130] D. Piazza, M. D'Amico, and K. Dandekar, "Performance improvement of a wideband mimo system by using two-port rlwa," *Antennas and Wireless Propagation Letters, IEEE*, vol. 8, pp. 830–834, 2009.

[131] R. Bahl, N. Gulati, K. Dandekar, and D. Jaggard, "Impact of reconfigurable antennas on interference alignment over measured channels," in *GLOBECOM Workshops (GC Wkshps), IEEE*. IEEE, 2012.

[132] P. Mookiah and K. Dandekar, "Enhancing wireless security through reconfigurable antennas," in *Radio and Wireless Symposium (RWS), 2010 IEEE*, Jan 2010, pp. 593–596.

[133] D. J. Teece, "Profiting from technological innovation: Implications for integration, collaboration, licensing and public policy," *Research Policy*, vol. 15, pp. 285–305, 1986.

[134] Decawave fully customizable ultra wideband antennae. [Online]. Available: http://www.dit.ie/hothouse/spin-outopportunities/successstories

[135] Adant s.r.l. [Online]. Available: http://www.adant.com

[136] Antrum l.t.d. [Online]. Available: http://www.antrum.co.uk

[137] Fractus s.a. [Online]. Available: http://www.fractus.com

[138] Fractus s.a. [Online]. Available: http://www.ficosa.com

[139] N. Kroes, “Europes risk-averse culture risks condemning it forever to second place behind the u.s.” *Europes World*, vol. special issue on Digital Economy, 2014.

Appendix A: Commercialization of Reconfigurable Antennas

Academic research is a major contributor to the development of new technologies [128]. In order to profit from technological innovation, universities utilize technology managers, who are typically employed in a Technology Transfer Office (TTO). These professionals act as a bridge between external entities, such as entrepreneurs or firms, and the universities which represent the academic scientists. Therefore, the main task of the TTOs is to boost the commercialization of the technologies developed within the university.

Following [129], we can divide the technology commercialization into three approaches. The first is the internal approach, where the TTO is in charge of promoting the commercialization of the research developed at the university. The second is a quasi-internal approach, where business incubators accelerate the growth and success of start-ups through the provision of business support, resources, and services. The third approach is external, and it entails research parks, spin-offs, collaborations, joint ventures, and open science and innovation.

Reconfigurable antennas represent one of the most recent examples of new technologies developed within academic institutions which have been brought to the market recently. As opposed to standard static antennas, Reconfigurable Antennas (RAs) are able to change their radiating characteristics in order to improve the wireless communication between two devices [130]. In addition to improve the data rate, RAs are able to cope and mitigate the increasing amount of interference due to the spreading of wireless networks, as well as

enhance security [131, 132].

Thanks to these advantages, several start-ups have been founded to commercialize this novel technology. Moreover, well established companies also decided to invest and develop new RAs.

In this dissertation, we summarize the fundamental concepts of external commercialization approaches, analyzing benefits and costs of the three major modes of commercialization: technology licensing, spin-offs, and joint ventures. Following a brief description of each mode, we summarize benefits and costs from both the academic and the entrepreneurial perspectives. For each mode, we also provide an example from the reconfigurable antenna field. Moreover, we provide a survey of the major companies that are currently commercializing reconfigurable antenna technologies. The survey shows the actual market applications of these technologies, as well as the different commercialization approaches.

A.1 Modes of University Technology Commercialization

Following previous literature [129, 133], we identify three modes of research and technology commercialization: internal approaches, quasi-internal approaches, and externalization approaches. Fig. A.1 summarizes these three academic modes of technology commercialization.

In the case of internal approaches, universities advance the commercialization of their technologies through the Technology Transfer Office (TTO). The office is in charge of bridging the gaps between the academic scientists, university administration, and the firms. Quasi-internal approaches facilitate the technology commercialization through business in-

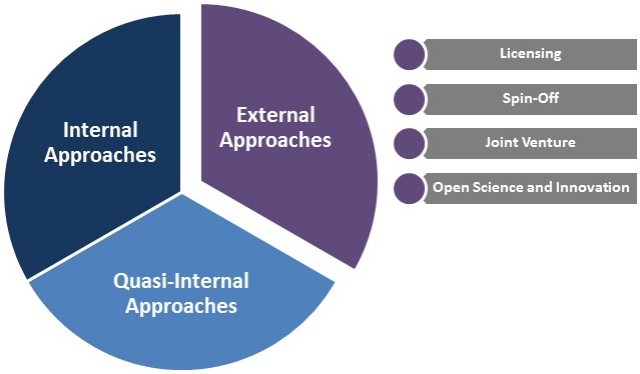

Figure A.1 Summary of the three academic modes of technology commercialization. The external approaches lead to higher separation from the academic institution, and it can be accomplished through technology licensing, spin-offs or joint ventures.

cubators. These entities foster the creation of start-ups (based on university-owned or licensed technologies) by providing business support, resources and services. In the case of externalization approaches, the technology is commercialized through university research parks, regional cluster, academic spin-offs and start-ups, licensing, contract research and consultancy, joint venture spin-offs, alliances and collaborations, and open science and innovation.

In the next subsections, we focus our analysis on the three most common modes of external commercialization: Technology Licensing, Spin-Offs, and Joint Ventures.

Technology Licensing

By licensing a new invention, the inventors (licensor) allow external firms (licensee) to use their invention at a specific royalty fee and often a lump sum upfront fee. The technology provided from the licensor might assume different forms. For example, in the case of electronics/RF technologies, the inventors provide a reference design of the hardware they invented, allowing the licensee to manufacture and market it. Other forms of technologies

might involve chemical formulas, engineering methods and techniques, software, etc.

The payment by the licensee can be structured in different ways. The two major methods are the up-front fees and the royalties. With the former method, the licensee pays a predetermined amount at the time the agreement is signed, while with the latter method the licensee pays a fixed or variable percentage on sales or on the units of product sold. The structure of payment between up-front fees and royalty fees is often contingent upon the nature of the technology, the market potential, the relative bargaining powers of the parties and other relevant factors. Moreover, the setting of an annual or periodic fee, which typically terminates when royalty payments begin, is an incentive for the licensee to aggressively develop and market the technology.

From the inventors' view point, patenting a technology puts the licensor in a better negotiating position because the risk of misappropriation by the licensee diminishes when the underlying technology is protected through a patent. However, technology licensing can be accomplished even without such a patent protection. An alternative to patenting is signing a non-disclosure agreement (NDA) between the licensee and the licensor. However, patenting represents a superior protection because NDA protects the licensor only with respect to those who have signed the agreement. In some industries where the innovation is embedded in processes, trade secrets are another viable alternative to patents. Trade secrets protection is possible only if the firm can put its product before the public and still keep the underlying technology secret.

In Fig. A.2, we summarize the benefits and costs of technology licensing for both the licensor and the licensee. From the licensor's perspective, the main advantage is to avoid manufacturing, marketing and commercialization costs. On the other hand, the licensee

can increase the speed of innovation while reducing the costs and risk of internal R&D. However, the licensee faces a tradeoff between internal R&D costs and the payment of up-front fees or royalty fees to the licensor.

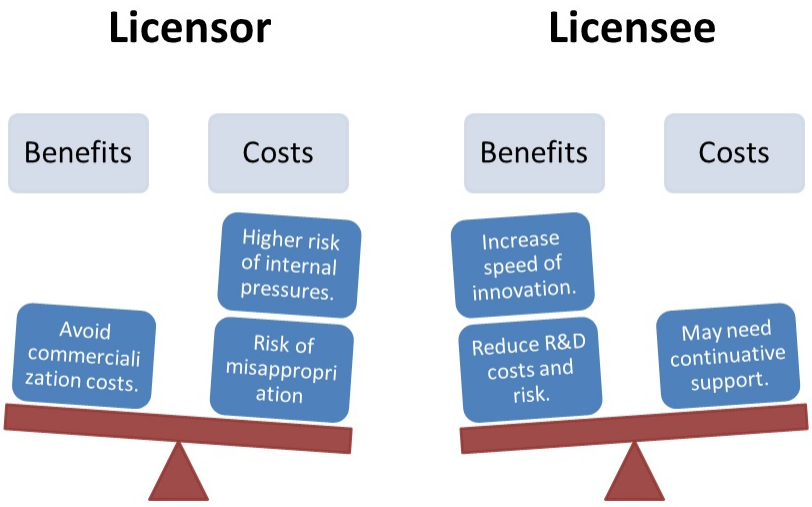

Figure A.2 Benefits and costs summary of technology licensing for both the licensor and the licensee.

In the case of public universities, the licensor may encounter more constraints in terms of political pressure. While private universities are more flexible, they are able to provide faculty royalty incentives to promote licensing and entrepreneurial activities [133]. Furthermore, when patenting new technologies in the form of Intellectual Property (IP), disclosure may lead to misappropriation by the licensee because the latter can change the IP marginally to invent around. Such actions often lead to legal battles and litigations. Even higher risks may come from those countries where the patent application has not been submitted. The potential costs for the licensee may stem from the need for continuous support in order to fully exploit the licensor's technology.

In the field of antenna technologies, an example of the licensing mode of technology commercialization comes from the Dublin Institute of Technology (DIT). DIT signed a li-

censing agreement with Decawave on specific antenna designs for the development of a small sensor chip [134]. Specifically, the miniature integrated circuit exploits ultra wide-band pulses to track assets with an accuracy of up to 7 cm, and the antenna technology provided by the university enables the efficient transmission of this series of pulses.

Numerous other antenna technologies were licensed from universities to newly founded start-ups and established firms. The examples in the next subsections discuss other forms of technology commercialization, beginning with licensing the IP from the university where the technology was invented.

Spin-Offs

A spin-off enables a university technology to be commercialized externally by founding a new company (startup). These startups rely on licensing or the assignment of a university or corporation's IP for commercialization. Typically, these companies are founded or co-founded by the leading faculty members, recently graduated Ph.D. students and researchers. In addition, faculty members may sit on the scientific advisory board of the spinoffs. In most cases, researchers and faculty members are the key shareholders of the company. However, the university or company may own equity at the early stage of these spin-offs. These start-ups often seek investments from angel investors and venture capital firms. As a result, the major ownership may be diluted over time as the external investors take equity stake in the startup.

In Fig. A.3, we summarize the benefits and costs of the spin-off. The key advantage of creating a spin-off through establishing a start-up is to be able to commercialize the technology without the constraints of the university system. The start-up becomes a sepa-

rate entity, where the decisions are made without the academic influence. The relationship with the university is often limited to the technology licensing, however, as part of the costs, a new start-up requires business knowledge and capabilities for an effective commercialization of the technology. The lack of complementary assets, such as marketing, competitive manufacturing, and after-sales support, may prevent the start-up from reaching its full potential. These complementary capabilities that are needed for a successful commercialization may not be known to the new entrepreneurs coming from academia.

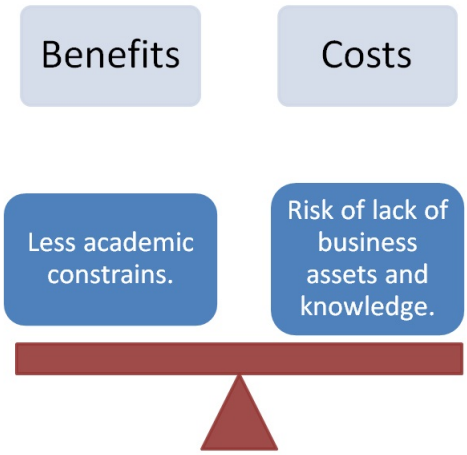

Figure A.3 Benefits and costs of the spin-off mode of commercialization.

In the field of antenna technologies, Adant S.r.l. [135] is an example of a start-up established as a university spin-off. The company was founded by a leading researcher and his advisor from Drexel University. Through the support of an incubator and financing of several venture capital firms (VCs), the company started to develop its smart antenna technologies for WiFi and RFID systems. The company utilizes the technology licensed from the university and continues to develop its own IPs through internal R&D. Another example of a university spin-off in the field of antenna technologies is Antrum Ltd [136], a

spin-off founded by a leading faculty member, with research funds from the Loughborough University, UK and other private investors.

Joint Ventures

Joint ventures are newly established companies that are jointly owned by a university and an industrial partner. While a company can be founded without a joint-venture, as in the case of spin offs, the combination of the two entities allows the university to access complementary assets that are required to commercialize technologies. These assets are not often available within universities or through a spin-off. The scientists that invented the technology typically have an equity stake in the new enterprise and they contribute to the further development of the technology.

In Fig. A.4, we summarize the benefits and costs of the joint venture mode of technology commercialization.

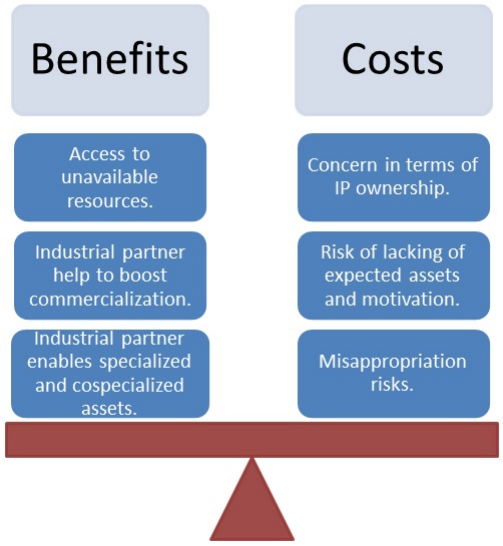

Figure A.4 Benefits and costs of the joint venture as a third mode of external approach of technology commercialization.

For the universities, the main benefit of establishing a joint venture is the access to the important, complementary commercialization assets that may not be available within the academia or spin-off. An industrial partner can enhance the technology commercialization prospect with its downstream assets, such as manufacturing and marketing competence, and relationships with other important constituents. These assets could be specialized for a particular technology that the industry partner had previously developed.

On the other hand, the mix of ownership in a joint venture may create concerns regarding newly developed IPs and how to distribute the revenues from the commercialized technology. Moreover, there is a risk that the industrial partner may not perform and contribute as expected. Misappropriation may also arise if the partner attempts to imitate the technology in order to compete with the innovator. In some countries, under a weak IP regime, governments may prevent foreign innovators by denying ownership of specialized assets. In such situations, the technology licensing might be more appropriate.

An example of a joint venture is Advanced Automotive Antennas (A3). The company is the result of a joint venture between Fractus S.A. [137] and Ficosa International S.A [138]. The former is a university spin-off, while the latter is a well-established multinational producer of automotive systems and components. Ficosa signed an agreement with Fractus that includes licensing rights for the use, application and development of the fractal technology to the automotive industry worldwide. In 2002, the two companies created the joint venture A3, which is dedicated to the application of Fractus technology, products and services to the automotive industry. The joint venture allows the academic spin-off, Fractus, to access those automotive assets and market themselves, which would be challenging to do by themselves.

A.1.1 Survey Results and Considerations

The fast growth of wireless communications has driven the necessity of exploiting technological solutions for the needs of faster connectivity. Although bandwidth allocation and Effective Radiated Power (ERP) are subjected to regulatory constraints, alternative solutions have been developed to overcome the challenges that arise in terms of wireless coverage and the number of users. Reconfigurable antennas technology is one of the hardware solutions that have been developed to enhance the connectivity between wireless devices. These new classes of radiating elements are able to adapt their physical characteristics in response to the environmental changes or user density and location. Unlike conventional "static" antennas, where the energy is wasted around the surrounding space, the reconfigurable antennas allow for a smarter management of the radiated energy as the beam can be focused toward specific directions. As a result, not only data throughput between two devices can be improved but also the interference between adjacent networks can be reduced significantly.

Because of the aforementioned technological benefits, several new companies started developing reconfigurable antennas for different applications. Although the main application remains to be WLANs, the reconfigurable antennas have been exploited among diverse wireless applications. In Table A.1, we report a list of existing companies that provide reconfigurable antenna technologies. We focused our survey on the companies that develop antennas for civilian purposes. The table summarizes each company by application, location, firm type and business model. We divide the companies into two groups - US and European based companies. Although the WiFi and WLAN applications seem to be the ma-

jor technology applications, reconfigurable antennas are also commercialized for mobile, vehicular and satcom applications. Furthermore, one firm also develops reconfigurable antennas for RFID applications.

Table A.1 Current Firms Commercializing Reconfigurable Antenna Technologies

Firm Name	Technology Application	Location	Type	Business Model
Airgain	WLAN, WiMAX	USA (CA)	Established	R&D & Manufacturing
Commscope	GSM, CDMA, W-CDMA, LTE	USA (NC)	Established	R&D & Manufacturing
Fidelity Comtech	Wi-Fi, Vehicular	USA (CO)	Established	R&D & Manufacturing
Kymeta	SatCOM	USA (WA)	Established	R&D & Manufacturing
Laird	Wi-Fi, Vehicular	USA (MO)	Established	R&D & Manufacturing
Ruckus Wireless	Wi-Fi	USA (CA)	Established	R&D & Manufacturing
Thinkom	SatCOM	USA (CA)	Established	R&D & Manufacturing
Adant	Wi-Fi, RFID	Italy	Start-up	R&D
Antenna Company	Wi-Fi	The Netherlands	Start-up	R&D
Smart Antenna Technologies	Mobile	England	Start-up	R&D
Sofant	Mobile	Scotland	Start-up	R&D

By looking at the first set of U.S. companies, we note that there are diverse applications where reconfigurable antennas are used. All of the U.S. companies are established, as opposed to the European companies that are startups. Furthermore, because the U.S. companies are established companies, their activities include internal R&D and product manufacturing. These companies invest heavily in complementary assets that are necessary for the successful commercialization of a new product (production facilities, marketing effort, etc.). However, in most of the cases, the marketed product is likely to be fabricated from external manufacturers.

The second set of companies are four European start-ups. Due to the limited capital and resources of these startups, they focus on R&D activities only, leaving the manufacturing to their customers. In essence, these companies follow the model of selling or licensing their designs to manufacturers of wireless access points and mobile terminals. The common denominator among all of these companies is the way they were founded. In fact, the

majority of these startups are spin-offs from European and US universities. As described in Section A.1, the scientists and the faculty members leading the academic research allowed the commercialization of these new technologies through the founding of a new company. As previously mentioned, these start-up companies are separate entities from the academia, which allows for more autonomy and possibly faster business growth.

The plausible reason why U.S. companies are often established firms and the European ones are startups is that the former ones are willing to undertake risky investments. Europe is characterized by a risk-averse culture that prevents established companies from supporting and investing in innovation [139]. On the other hand, in the U.S., the high interest in ICT technologies, especially in the telecommunication sector, fosters the investments and thus the infrastructures for the development of new technologies. Even though we observe that European entrepreneurs try out new ideas and have funded the aforementioned startups, the mode of pure R&D and licensing is a common approach for avoiding the costs and risks associated with the product's commercialization. In the U.S., the higher access to capital and the reduced risk-averse culture allows the companies to utilize the internal R&D mode, along with internal manufacturing. Despite the initial higher upfront costs, this approach is likely to be more profitable and it reduces the misappropriation risks. It is also important to note that the U.S. is characterized by large governmental and defense funding programs that contribute to, and boost, the RF industry. This aspect can be noted also by the more diverse set of applications where reconfigurable antennas are employed (e.g., satCOM and vehicular applications). Even though we cannot ignore that some of these established firms may have acquired licenses from third parties, to our best knowledge these companies focus on internal R&D development for their technologies.

In terms of technology application, the U.S. companies exploited reconfigurable antennas for diverse applications, while European companies seem to converge on traditional WiFi or mobile applications. The aforementioned analysis can also be seen as an opportunity to investigate the use of reconfigurable antennas for unexplored applications.

Vita

Damiano Patron received the B.S. Degree in Electronics Engineering from University of Padua, Italy in 2010 and the M.S. Degree in Electrical and Computer Engineering from Drexel University, Philadelphia, PA in 2013.

From 2002 to 2010, Patron worked with Euro-Link S.r.l. in the field of RFID systems. In 2010 he joined the start-up company Adant Inc. as an RF and antenna Engineer, designing reconfigurable antennas for WiFi and RFID applications.

His research focuses on the design of reconfigurable antennas for throughput maximization and DoA estimation in wireless networks. He also works in the development of wearable sensors and power harvesting systems. Patron is the author and coauthor of several patent applications in the field of reconfigurable antennas, antenna miniaturization and wearable technologies. He received several awards including the Drexel Frank and Agnes Seaman Fellowship Award in 2013, the Drexel Allen Rothwarf Research Award in 2014, the Young Scientist Best Paper Award at the ICEAA IEEE APWC EMS 2013 Conference and the Rectenna Competition Award at the IEEE RFID International Conference in 2015.